UNIVERSITY OF CALIFORNIA
RIVERSIDE

Optical Coherence Tomography for Structural Neuroimaging and Non-Contact Recording of Functionally Stimulated Neural Activity

A Dissertation submitted in partial satisfaction
of the requirements for the degree of

Doctor of Philosophy

in

Bioengineering

by

Md Shahidul Islam

December 2013

Dissertation Committee:
Dr. B. Hyle Park, Chairperson
Dr. Victor G. J. Rodgers
Dr. Valentine I. Vullev

The Dissertation of Md Shahidul Islam is approved:

Committee Chairperson

University of California, Riverside

Acknowledgements

First of all, I would like to acknowledge the support, guidance and encouragement I received from my advisor Professor B. Hyle Park. I was blessed to be the first graduate student in his new lab and this provided me an incredible opportunity to learn and build everything from scratch. Hyle was very approachable and supportive all through my PhD research. I want to thank Hyle for his patience during the early years and uneasy times of this project. He has been an inspiring figure for me both in academic and research activities and I learned from him how to be a better person both at and outside work. Thanks for being more than just an advisor, instead becoming a guiding friend and a encouraging coach for all of us in lab.

I would like to thank my dissertation committee members, Professor Victor G. J. Rodgers and Professor Valentine Vullev, for their time to review my work and provide me valuable feedback. I also thank my other oral qualifying exam committee members, Professor Jerome Schultz, Professor Khaleel Abdulrazak and Professor Maxim Bazhenov for reviewing my proposal during the PhD candidacy exam.

Most of this work has been possible because of great support from my lab mates and colleagues outside lab. I would like to thank all present and past members of NOIR lab, Gregory from Dr. Bazhenov's lab, Mike Hsu and Jenny Szu from Dr. Binder's lab and Ian Johnson from Dr. Huinan Liu's lab. I want to specially acknowledge the great

teamwork with my lab mate and friend, Md Rezuanul Haque at different steps of this research. His motivation, discussions and help with horseshoe crab dissection has been instrumental during the course of this research. Thanks to Rezuanul for being there during the uneasy times and providing me his honest and critical feedbacks at work. Christian M. Oh has been a great colleague and friend since the day one of building the system. Thank you Christian for all the instant discussions and support and having the mindset for high standard of work. It has been a great pleasure and opportunity to work in NOIR lab. I want to appreciate the great time I had with my lab mates in and outside lab during this last five years. I also want to acknowledge the support from the personnel at Bioengineering department office. Denise Sanders, Crissy Reising, Jennifer Morgan, Corena Valencia and Hong Xu from lab safety have been great support all through last five years. Funding supports from UCR Dean's fellowship, gradate division TA stipends, NIH R00 grant, ASLMS grant and other grants are also highly acknowledged.

Last but most importantly, I want to thank my family members for their inspiration and patience all through my academic life. I want to thank Mom, Dad for your strong support without which nothing would be possible today. Thanks to my two younger brothers, Shafiq and Jahid for everything you did. Thanks to my loving wife, Fatima Nafisa Putul for your love, patience and encouragement. I want to thank my Nanu, Nana, Sezo mama, Choto mama and Solaiman mama for your encouragement to do something big since the time I was a kid. I thank all my teachers at schools and colleges, my friends and well-wishers. Thanks to my friend, Khalid Ashraf for encouraging me to go to graduate school. Finally I pray and thank to the Almighty for everything.

Md Shahidul Islam
Riverside, California

To my dear mom
For your love, support and lifelong dedication

ABSTRACT OF THE DISSERTATION

Optical Coherence Tomography for Structural Neuroimaging and Non-Contact Recording of Functionally Stimulated Neural Activity

by

Md Shahidul Islam

Doctor of Philosophy, Graduate Program in Bioengineering
University of California, Riverside, December 2013
Dr. B. Hyle Park, Chairperson

Nerve activity in a biological neural network is mostly characterized by generation and propagation of impulses through the nerves. These impulses, known as action potentials, are generated when the nerves are excited by a stimulus either as an external input or as a means of internal communication between nerves. This project is aimed to develop an optical imaging based minimally invasive technique for neural recording. Existing technologies largely limit the analysis of neuronal processing to a single or small cluster of neurons using different varieties of electrodes or the introduction of exogenous contrast agents and most of these techniques are invasive in some ways. Nerves undergo rapid transient thickness changes during propagation of action potentials. These activity

associated structural changes are usually in the order of nanometers which is well beyond the usual limit of resolution of most common imaging technologies, including optical coherence tomography (OCT). However, recent advances in phase-resolved OCT (pr-OCT), a specific modality of OCT, have enabled the measurement of subnanometer changes in optical path length. This study demonstrates pr-OCT's capability to detect and measure rapid transient thickness changes in nerves during activity. Optically detected changes in nerve fiber thickness have timing and duration similar to the propagating electrical signal recorded in electrophysiology. Averaging of 8-10 impulses improves the SNR of detected optical signal. However, most of the results demonstrated here are single shot detections. Since OCT collects data from every depth points within a single A-line simultaneously, the changes in phase at every depth location are examined. Results demonstrate that these transient changes are present at different depths and this allows representing activity as a map of thickness changes. A custom-built cold block system has been used for switchable control of activation and deactivation of action potential propagation through the Limulus nerve. Optical recording has been compared with simultaneous electrical recording at every stages of cold block operation: activated nerve before deactivation, nerve after deactivation and nerve after reactivation. Hopefully, this study will serve as the basic ground work for future experiments and will have an overall significant impact on functional neuroimaging.

Table of Contents

List of Figures

Introduction

The nervous system consists of a large assembly of neurons that maintain different levels of hierarchy according to their specific location and function. Studies dedicated to investigate these neural circuits and their pathways largely depend on the information of how neurons communicate with each other. Therefore, real time monitoring of neuronal activity is an important part of neurobiological research. Currently available techniques usually measure activity using electrodes and in some cases, take the advantages of using fluorescent dyes for enhanced contrast. However, there are often cases where bringing an electrode into contact with a nerve is difficult or even impossible, such as in the retina. Depending on the dose and cellular environment, fluorescent dyes may induce different levels of toxicity. The focus of this research is to develop a non-contact minimally invasive optical method which can record single electrical activity in neurons. It has been known for more than six decades now that the active area of a nerve undergoes very small transient structural changes and very recently, non-contact imaging technique called phase-sensitive optical coherence tomography (OCT) has proven to be capable of measuring displacements of similar orders of magnitude. So, this research is aimed at developing a phase-resolved OCT electrode for real time monitoring of nerve activity.

This dissertation is organized in six chapters. Chapter 1 provides a brief literature review of the currently available optical and non-optical neural recording technologies. It

describes the techniques ranging from conventional electrical methods to magnetic and optical approaches. It summarizes the benefits and limitations of these methods. Chapter 2 introduces optical coherence tomography (OCT) in details. This chapter explains the principle and mathematical representation of OCT and its one specific modality, phase-resolved spectral domain OCT (pr-SD-OCT). Next section of this chapter summarizes the application areas of conventional OCT and its different modalities. Later, this chapter discusses the previous studies and capability of OCT for neural recording.

Chapter 3 discusses the calibration, characterization and imaging experiments. Every major step in calibration and characterization of basic OCT and pr-OCT system has been explained in this chapter. The last section of this chapter has provided a quick glance to the imaging capabilities of the implemented system.

Chapter 4 and 5 are focused towards the optical detection of neural activity in horseshoe crab optic nerve. Chapter 4 discusses the animal model and sample preparation, details experimental setup, structural imaging and activity recording and finally the post analysis schemes. This chapter highlights the results obtained from single shot detection, which, to the best of our knowledge, has been demonstrated for the first time for functionally stimulated neural activity. This chapter also discusses averaging of multiple responses and pictorially shows how increasing the number of impulses for averaging improves the overall signal-to-noise ratio. The last section of this chapter describes a new scheme of

data analysis where multiple groups of depth points are analyzed simultaneously and the neural activity associated optical changes are resolved at different depths. This depth-resolved activity detection allows a larger region of bundle to be analyzed at the same time. Hopefully this study will pave the way to build next generation micro OCT-electrode array (MOA). Chapter 5 discusses the two control experiments which were performed for validation of the OCT data that claims detection of neural activity. Both the experiments - excess KCl and cold block experiment - are explained and the results are discussed.

Chapter 6 originates from some recent study aimed at investigating the changes in optical properties of brain tissue during neural activity. Experiments on mouse brain slice and fruit fly brain stem have yielded some exciting results which are very briefly discussed in this chapter. This chapter is included in this dissertation to hint a pathway to future research direction where similar technology can be used not only for *Limulus* optic nerves, but also to study the activity in both vertebrate and non-vertebrate animal's brain models.

In fine, the dissertation is concluded with a brief summary of the overall findings of this study and highlighting the significant achievements that can lead to future research studies.

Chapter 1

Recording of Neural Activity

1. Action Potential: Mechanism of Initiation and Propagation

The nervous system is the major control system in an animal's body whose task is to coordinate other organ systems that make up the organism [1]. It is a network of specialized cells, mostly neurons and glials that coordinates the communication between different parts of the body. The nervous system has a complicated structure and is anatomically and functionally divided into two major parts – central nervous system and peripheral nervous system. The central nervous system (CNS) is formed by brain and spinal cord while the peripheral nervous system (PNS) contains the sensory and motor neurons spread all over the body. In this way, PNS connects all the organs and limbs of the body to the CNS and thus they play a fundamental role in the control of animal behavior and cognition [1-3].

Neural Activity

Activity in the nervous system is largely caused by internal signaling (e.g. regulation of heart rate from the CNS) or from communication with the external world (hearing a sound, smelling something fragrant, etc). The basis of all these activities is neuronal communication, i.e. communication between neurons. The nervous system possesses an

immense number of lines of communication provided by the large assembly of nerve cells or neurons. Neurons are the fundamental unit or building block of the nervous system and to understand the activity in the large network of neurons, it is of paramount importance to observe and understand the activity in a single neuron or a small cluster of neurons. Fortunately, due to a significant number of researches done in the past, a good amount of understanding has been achieved of how neurons transmit and receive signal. It is now well known that neurons communicate with each other in a network by transmitting electrical signals known as "action potential" [2]. It has been also discovered that the electrical signals are mostly identical in all nerve cells of the body and also very similar in different animal species [2]. Although the action potential is similar irrespective of the location of the nerve cell, depending on the origin and the destination of the nerve fibers and the frequency or patterns of firing of action potential, the same electrical signal is interpreted differently in the brain [1-3].

Action Potential

As mentioned in previous section, neurons communicate by transmitting electrical signal called action potentials. An action potential in a nerve cell is initiated by a stimulus which can depolarize the cell in such an extent that exceeds the threshold membrane potential. In absence of action potential, the ratio of permeability of sodium and potassium ion channels (P_{Na}/P_K) stays approximately at 0.02 and thus the resting potential is dominated by potassium ion channels and it stays approximately close to the Nernst potential for K^+

(~-70mV) [1]. Schematic representations of the different phases in action potential generation and the gating of voltage gated ion channels are provided in Figure 1.1.

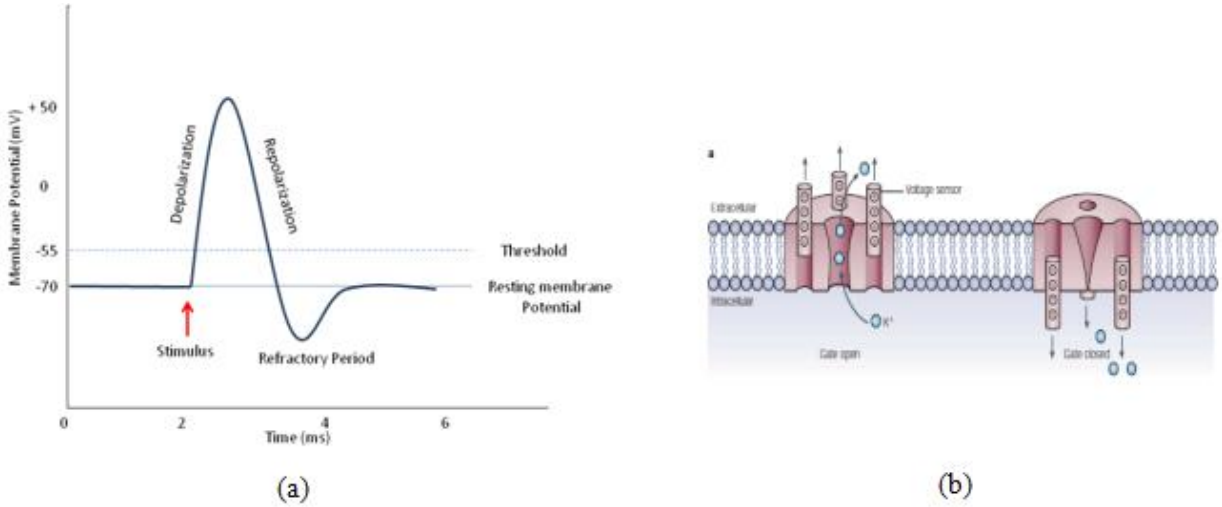

Figure 1.1: (a) A schematic showing different phases of an action potential generation in a cell membrane. (b) Schematic of a voltage gated potassium ion channel. It illustrates the mechanism of channel gating (close and open states) in the membrane [32].

Any depolarizing stimulus increases the permeability of voltage gated sodium channels in the membrane and when the depolarization is above the threshold, the ratio of permeability of sodium and potassium ion channels (P_{Na}/P_K) increases enormously peaking at a value of around 20 [1]. Due to this increased permeability of sodium channels, Na^+ ions enter the cell rapidly and this process is regenerative due to the nature of voltage-dependent sodium channels. When the membrane potential reaches its peak of action potential (~+30 to +50mV), sodium channel closes because of the negative effect of the inactivation gates (h gate). On the other hand, there are also voltage gated potassium channels which also open due to depolarization albeit relatively slowly. When sodium channels close, the effect of potassium ions leaving the cell becomes evident and

within a very short time, the membrane potential becomes negative again and finally returns to its resting potential. Just before the end of action potential, a small undershoot of membrane potential is briefly observed due to the leakage of potassium channels [1]. This action potential is propagated along the nerve in similar way electric current flows through an insulated conductor. The mechanism of propagation is very simple owing to the fact that once the one end of the neuron is depolarized, the strong depolarization will bring the neighbor region of the cell above threshold and thus sets up a regenerative depolarization in that region. The impulses propagate in only one direction since the refractory period of the preceding region of cell prevents it from being excited again. Therefore, action potential is a self propagating wave of depolarization that sweeps along the length of the nerve. Once this impulse reaches the end of the nerve, it transmits a signal to the next neuron through electrical or chemical synaptic communication. In short, this is the mechanism of how signals are propagated through the neurons and reach their destination through different neural circuitry.

Significance of Action Potential Detection

It is quite clear from the above discussion that a detailed investigation of a neural network or the nervous system overall is largely dependent on the monitoring of neural activity at the neuron level. Neurobiological research experiments greatly rely on the recording of neural activities and a reliable recording technique is of utmost importance for the success of these research studies. Apart from applications to neurobiological research, assessment of the physiological condition of neurons either in research or in

clinical applications strongly depends on the recording of action potential propagation through those cells. So, there is no doubt that detection of neural activity is a fundamental requirement for neuroscience research. Fortunately, these action potentials are associated with different kinds of transient physical, chemical and optical changes in nerve cells. By taking the advantage of these responses, various techniques have been developed over the years which can detect the presence of action potentials.

In the next section, a literature review has been presented focusing on the major kinds of detection techniques developed recently. Subsequent sections describe the principle and recent applications of the imaging technique, "optical coherence tomography" and explicitly emphasize the potentials of this technique to be a new method for action potential detection.

2. Action Potential Recording Techniques

A number of techniques have been employed in the detection of action potential propagation. A brief review on past and current methods that have been used for action potential detection is presented here.

a. Electrical Recording Methods:

Luigi Galvani showed for the first time in 1791 that frog muscles could be stimulated by electricity, and this finding initiated high amount of interest to researchers to measure electrical activity in biological samples. Successful measurement of nerve impulses was reported in the 1920s, when microelectrodes were used to record activity. The technique

of microelectrode is very simple as it uses a circuit where the potential difference between ground and microelectrode tip that touches the nerve is amplified to show and record the activity. Depending on requirement, different kinds of electrical recording techniques can be used.

Intracellular Recording:

In case of intracellular recording, the tip of a microelectrode, filled with a concentrated salt solution, is inserted into the cell with the help of a micromanipulator and is used to measure the potential difference between the inside and outside of the cell [2]. This recording method is very useful to obtain information about excitation and inhibition processes in neurons and also to investigate the mechanism of spike generation [4-10]. Intracellular methods include voltage clamp methods where the membrane of a cell is clamped to a certain voltage and then the flow of ionic current is measured with time. In current clamp methods, membrane potential is recorded by injecting current into cell though recording electrode and thus it allows studying the cell response to the entering current. Patch clamp methods use a different approach than conventional intracellular recording methods. A microelectrode with a slightly larger tip is placed close to the cell and a suction applied to it, causing part of the membrane to become attached with the tip to form a high resistance seal between glass tip and cell membrane. This considerably reduces the thermal noise in measurement as thermal or Johnson noise is largely dependent on the input impedance of the electrode [11].

Extracellular Recording:

A fine wire insulated almost to its tip or a capillary tube filled with salt solution can be used as an electrode for extracellular recording. Extracellular recording can reveal information about the functional state of a neuron or a group of neurons. It can also provide information about whether the rate of firing is increasing or decreasing [2]. Pine used an array of 32 microelectrodes for high SNR extracellular recording of cultured neurons obtained from cervical ganglia of rats and he successfully recorded neuronal activity [12]. Extracellular recordings have been employed in a number of studies to provide a significant amount of information about different regions of central nervous system [13-16, 19-20].

Limitations: Electrical recording techniques are by far the best currently available methods for action potential detection. Since their first use in 1920s, neurobiology research has progressed rapidly and now these techniques are part and parcel of the field. However, these electrical recording methods, depending on the application environment, raise some concerns which prompt us to think for better alternatives. Firstly, intra-cellular, extra-cellular, and planar-array electrodes require contact, or at least close proximity, between the structure of interest and the electrode. However, these electrodes are not feasible in many applications due to inaccessibility, e.g. retina or optic nerve. Secondly, intracellular recording methods require puncturing the nerve cell to insert the tip into the cell and poor accuracy in doing those highly sensitive measurements may lead to potential damage to the nerve fibers. Also, difficulty arises in using a large number of electrodes in a limited field. Furthermore, high charge injection densities at the electrode-

cell surface may cause corrosion induced degradation of electrode and thus may injure the tissue surface. So, because of being contact based mechanisms, electrical recordings of neural activity are more or less invasive.

b. Magnetic Detection Methods:

Some interesting studies on magnetic detection of action potential propagation have shown that the signal propagation through it can be detected by measuring the magnetic fields around a nerve. The principle is that when there is any neural activity taking place in an axon, the dipoles inside the axon are redistributed spatially due to transient intracellular current and this rapid change in distribution of dipoles originates a magnetic field. Roth et al. has shown that magnetic field in the action potential site of an axon can be measured from the transmembrane potential measurement and alternatively, the shape of membrane potential can be measured from the measurement of magnetic field [21]. Wickswo et al. developed a low noise solid state amplifier to record magnetic field variation during the nerve activity and their recorded signal corresponded to the shape and magnitude of an action potential [22]. Trontelj et al. investigated action potentials in plant intermodal cells by using magnetic detection technique. They demonstrated that action potential propagation in an axon of the plant, *Chara coralline,* can be magnetically recorded by using a device with 37-dc-SQUID magnetometers mounted on a plane close to the intermodal cell [23].

Limitations: Although these studies on magnetic techniques showed promising results and evolved a completely different approach to action potential detection, one of the main

drawbacks of these detection techniques is their low signal-to-noise ratio. SNR is a critical issue in detecting rapid and transient signals like nerve impulses. In particular, the signal to noise ratio in magnetic detection falls very sharply at low frequencies (< 10Hz), i.e. for slow activities, the reliability of this probe goes down. Besides this, the magnetic detection requires that the probe is in close proximity of the nerve because the magnetic signal falls of very rapidly in radial direction. These toroid based detection schemes are also limited by the fact that one end of the nerve has be incised or dissected completely before measurement so that it can be threaded through the toroid for picking up the magnetic signal by the attached pick up transformer. Moreover, magnetic measurements are also sensitive to the magnetic fields originated from the neighbor cells and this may cause crosstalk during measurement.

c. Optical Methods:

Fluorescence Based Methods

Fluorescence imaging is one of the most widely used optical methods for investigation of neural activity. A large number of studies in last decade have studied and improved the viability of fluorescence methods for neural studies. As early as 1964, Shtrankfeld and Frank observed a 10% reduction in fluorescence intensity for cells stained with primulin [24]. The intrinsic fluorescence of neurons has also been utilized for optical imaging. Two classes of molecules naturally found in axons are fluorescent: NADH (reduced nicotinimide-adenine dinucleotide) and other metabolic intermediates, and proteins, particularly those with tyrosine and tryptophan side chains. More recently, Levene *et al.*

used multi-photon microscopy of intrinsic fluorescence to image nerve cells, but this method was not sensitive to fluorescence changes due to activity [25]. Similarly, Jung *et al.* utilized one- and two-photon fluorescence microendoscopy to image red blood flow dynamics, but no dynamics were observed [26]. However, a promising study by Kasischke in 2005 used 2-photon fluorescence imaging of NADH to provide sensitivity and spatial resolution to resolve metabolic signatures in processes of astrocytes and neurons deep in highly scattering brain tissue slices [27]. One of the main reasons behind the failure of the above studies is their very low signal to noise ratio. Therefore, in most cases the intrinsic signal cannot be used reliably as an indicator of spike propagation and hence contrast agents are required to enhance the indicator signal. The major two types of fluorescent dyes used as contrast agents are voltage sensitive dyes and ion sensitive dyes. Voltage sensitive dyes (VSD) exhibits increased fluorescence in presence of action potential. Significantly, in 1968, Tasaki and Watanabe measured the fluorescence intensity changes for cells with ANS (1-anilino-8-naphthalene sulfonate), a voltage sensitive dye [28]. Grinvald et al. in 1981 studied the application of voltage sensitive dyes to detect the evoked activity in rat hippocampus pyramidal neurons (CA1) and their recorded activity matched with the electrophysiological recordings [29]. There are few other studies that also used voltage sensitive dyes as a contrast agent in their neural recording [30-31].

Due to the lack of strength in VSD signals, recent studies are mostly focusing on ion sensitive dyes which exhibit signal few orders of magnitude higher than VSD signals.

These dyes, depending on their chemical structure and properties, target particular ions in the active site of neuronal activity. The major motivation behind fluorescence imaging using Ca^{2+} sensitive dyes is that during action potential, a transient influx of Ca^{2+} ions is triggered in neurons and this influx occurs through the voltage gated calcium channels located almost all over the nerve cell. So, propagation of an action potential through the axon or synapse can be detected by observing Ca^{2+} concentration in that region [33-36]. Calcium ion sensitive dyes provides more than 100 fold greater fluorescence signal during activity than any other ion and as a result, Ca^{2+} indicators allow the monitoring of nerve activity even for single neurons due to ubiquitous presence of calcium channels in neuron, activity can be resolved in a population of neurons [34-40]. Although these dyes provide very good contrast in depicting level of activity in different regions of the neural circuit, the technique of introducing these dyes into a specific location remains a challenge as it involves invasive procedures in most cases. Therefore, genetically encoded calcium indicators based on recombinant fluorescent proteins have been recently developed which can be used for long term investigations and by using these indicators, cell specific imaging of neuronal activity has been possible in living animals [41-44].

Limitations: Although fluorescence based techniques have proved their feasibility as a tool for monitoring neural activity, there are some limitations with these methods. Firstly, voltage sensitive dyes may not be suitable in conditions where noise level is so high that it almost surpasses the low optical signal from VSD. Synthetic dyes are disadvantageous in case of long term use because they may cause pharmacological side effects. Different chemical dyes may have different pharmacological side effects in different cellular

environments. It is quite difficult to set a standard level of toxicity for these synthetic dyes. Another drawback of using dyes is that their optical signal can be significantly reduced due to bleaching effect. Bleaching usually occurs when the exposure time is relatively high [29]. Photodynamic damage is another issue involved with fluorescent dyes. Some of these dye molecules sensitize the formation of reactive singlet oxygen, mostly when there is intense illumination. Some of the studies have shown that these reactive radicals attack membrane components and damage the cells [45-46]. This puts a strong restriction on the duration of experiments. Sometimes the delivery of these dyes to the proper locations becomes challenging due to their variations in cell specificity and difficult loading mechanisms [44]. Due to all these limitations of fluorescent methods, *in vivo* application of these methods is still quite questionable.

Absorption Based Methods:

A limited numbers of studies have been done which focused on absorption based optical methods for detection of nerve activity. These methods looked at the changes in absorption of voltage sensitive dyes which have been used in staining the nerve tissue. Studies have found that depending on the properties of dye, some specific dyes have shown larger change in absorption than fluorescence during activity and this gives a better signal-to-noise ratio in recording. This increased absorption signal was observed in experiments with ganglia cells of *Aplysia califonica and Hirudo medicinalis* with the Oxonol dye RGA509 [47-49]. However, these are very specific cases where changes in

absorption were larger than any other optical change and in majority cases, changes in fluorescence or scattering dominates.

Nonlinear Optical Microscopy:

Non-linear microscopy techniques have the advantage of having relatively larger imaging depth than scattering based optical methods [50-52]. Previous studies have investigated the ability of non-linear microscopy techniques for monitoring changes in cell membrane potential [50, 53-54]. Second harmonic generation (SHG) is an available nonlinear microscopy methods that has been used in a recent study to monitor nerve activity in *Aplysia* [50]. SHG was able to detect the action potential propagation and the spatiotemporal resolution was very good compared to other optical methods (0.833msec and 0.6μm). However, the limitation of this kind of study is poor signal-to-noise ratio (~1 for single scan and ~6-7 while averaging 50 scans) and possible photodamage to the cell. Although the long term effect of this photo damage was not quantified, it definitely puts a limitation on imaging for longer duration.

Surface Plasmon Resonance:

The applicability of surface plasmon resonance (SPR) technique in detecting action potential has also been demonstrated very recently by Kim et al. [55]. This study reported the development of an SPR device with a metal surface as sensor which can detect the nerve impulses by monitoring the optical changes at the metal-nerve interface. However,

the requirement of attaching the nerve to the metal surface may reduce the application area significantly. Moreover, development in scanning speed and obtaining improved spatial resolution will be required to do real time studies with this kind of technique.

Scattering Based Methods:

Studies have discovered that optical scattering also changes during nerve activity. According to literature, in 1949 Hill and Keynes first reported an increase in optical scattering during action potential propagation in a crab nerve placed in Ringer's solution [56]. However, a later study found that optical scattering actually decreased during trains of action potentials in crab nerves in seawater [57]. In both these experiments, only the presence of a change could be determined; the timing of the scattering change was not determined. Improvements in instrumentation made this possible later, when Cohen and Keynes were able to determine that the time course of these scattering changes in crab nerves was similar to that of action potential propagation [58]. Further study revealed that the scattering change consisted of two components: a transient signal that accompanied the action potential followed by a second long-lasting component that reaches a peak about 20 msec. afterwards [59]. Both these scattering changes were shown to be current-dependent. Experiments by Cohen, Keynes, and Landowne in 1972 demonstrated that the scattering changes were due to a volume change in the periaxonal space [60]. Later, a very significant work by Stepnoski et al. in 1991 described that the refractive index of axon membrane changes during the spike propagation and this was hypothesized to be the result of reorientation of dipoles in membrane due to increased membrane potential

[61]. However, their results showed a linear relationship between optical change and the membrane potential which slightly disagrees with an earlier study by Cohen et al. where they observed quadratic dependence for a larger membrane potential range [60]. Significantly, these studies have confirmed activity induced scattering changes in neurons and this has led to a new area of research which investigates the design and development of more sophisticated techniques in order to measure these very small transient changes. As suggested by Stepnoski et al. and others, interferometry can be a very good technique to detect these voltage induced changes. Surprisingly, some recent and past studies based on interferometry, such as laser interferometry and optical coherence tomography, have shown significant promises to be able to detect these transient changes and thus attract attention for further research [62-65].

Chapter 2

Optical Coherence Tomography

Optical Coherence Tomography (OCT) is an emerging optical imaging technique that has found growing interest in recent times because of its capability to generate high resolution cross sectional images of internal microstructure of biological tissues. The underlying principle of this technique is described below in addition to a brief description of some of its major modalities. Later on, a brief summary of application areas of OCT and its applicability, specifically in neural recording is discussed.

1. Principle of Optical Coherence Tomography

Optical Coherence Tomography is, in principle, analogous to ultrasonography. In ultrasonography or ultrasound, sound wave from an acoustic source is transmitted into the tissue structure and the time delays of reflected sound waves are used to measure the depth of the reflecting structures in tissue sample. In OCT, light waves are used instead of sound and because of the fact that light travels at a much faster (~10^6 times) velocity than sound, similar measurement of the time delays of reflected light waves is quite impossible. Therefore, a different detection method is used in OCT where time delays are measured from the interference fringes resulting from the backscattered lights from sample and a reference reflector. A mirror with very high reflectivity (>95%) is usually used as a reference reflector.

Huang et al. (1991) first successfully developed this imaging technique and they also demonstrated *in vitro* cross sectional imaging of retina and coronary artery [75]. This breakthrough study proved the feasibility of OCT imaging in biomedical field and opened a new door of imaging research. In principle, OCT is basically a Michelson interferometer that uses low coherence interferometry as detection technique. A general schematic of OCT system is shown below (Figure 2.1).

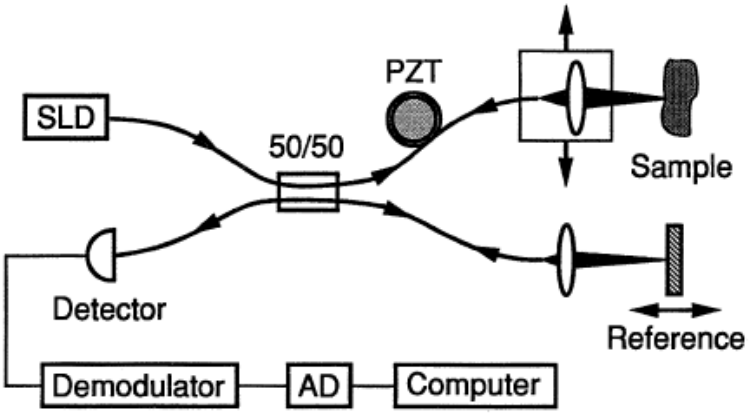

Fig. 2.1 Schematic of a Basic Time Domain OCT System based on Michelson Interferometer [75]

OCT uses low coherence interferometry technique where a low coherent light source is used to send light through a beam splitter which sends part of light to the reference arm and rest of it to the sample arm. A galvanometer controlled scanner is used in the sample arm to scan the sample in the lateral direction. When the light waves reflected back from the reference arm and sample arm are collected at the detector, they form interference. These detected interference patterns are used to extract information about the structure of the sample. After several steps of image processing on the extracted information, a cross

sectional image of the sample is obtained. OCT images have axial and lateral resolution usually in the range of 1~15μm and 5-20μm, respectively.

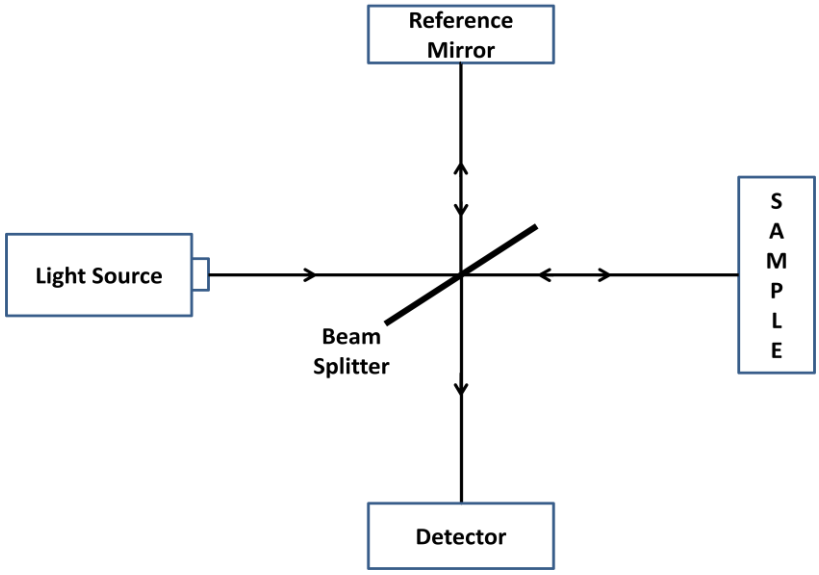

Fig. 2.2 Schematic of a Michelson Interferometer to illustrate the principle of Low Coherence Interferometry

Low Coherence Interferometry

When two or more waves of similar wavelength are superimposed on each other, they produce interference. Low coherence interferometry technique measures the interference of two optical fields. A light source is used which has low temporal coherence but high spatial coherence. This partially coherent light beam is directed onto a beam splitter that splits the light into two portions – a reference beam and a sample beam (Figure 2.2). These two beams travel the set distances in reference arm and in sample arm, respectively. Once they reach the reflectors at the end of each arm, these light beams are reflected back in the opposite direction and they are combined in the splitter. Then the

resulting interference fringes are collected by the detection device in the detector arm. LCI uses broadband light source and because of broadband nature, mutual interference between two optical fields only occurs when the optical path difference between these two fields are within the coherence length of the source. As these sources have very small coherence length (2~20μm), OCT can provide images with very high axial resolution. Alternatively, this means that by using very wideband light source, OCT can provide very strong resolving power in axial direction.

This low coherence interferometry technique, being a one dimensional measurement, cannot form a cross sectional image of a three dimensional volume. When multiple parallel low coherence interferometry scans are performed over a dimension of a sample, and then these reconstructed data provides tomographic or cross sectional image. This is how OCT images are formed from the lateral LCI scans performed along a dimension of a sample. Each LCI scan or depth profile is called an A-scan (z-axis) and the lateral scans are termed as B-scan (x-axis). OCT can also provide 3D volumetric images by reconstructing all the cross sectional images or "slices" obtained by scanning in the third dimension (y-axis). This third dimensional scan is called C-scan. This outstanding ability of producing high resolution volumetric images of microstructures has enabled OCT to earn significant attention from the biomedical imaging research community.

Mathematical Description of OCT

A mathematical representation of OCT will give us a better perspective about this measurement technique. Let us assume that the sample placed in the sample arm is a

simple mirror with high reflectivity and the polarization effects are ignored. We also assume for this case that the detector collects all the light that is coming back from the two arms – reference and sample arm. Now if the electric fields of backscattered light in reference and sample arm are denoted as $E_r(t)$ and $E_s(t)$, and the optical path length in two arms are referred as l_r and l_s, respectively, where $\Delta l=|l_r - l_s|$, then the intensity of light detected in detector can be expressed as:

$$I_d(\tau) = \langle [E_S(t) + E_r(t+\tau)][E_S(t) + E_r(t+\tau)]^* \rangle \quad (2\text{-}1)$$

where τ is the time delay between the two reflected beams due to their optical path difference, i.e. $\tau = \Delta l/c$ where c is the velocity of light in air medium. This path difference Δl is two times of the physical path difference between two arms because optical path includes round-trip distance. The sign $\langle . \rangle$ means that the measured intensity is the time average of the integrated intensity over the integration time of the detection device. Now in equation (2-1), the intensity is calculated by using square law detection rule which means intensity of detected light is the squared term of the detected electric field. Using the same rule, we can write $I_s = \langle [E_S(t) E_s^*(t)] \rangle$ and $I_r = \langle [E_r(t+\tau) E_r^*(t+\tau)] \rangle$ where I_s and I_r are individual component intensities of detected light that were backscattered from sample arm and reference arm, respectively. So, equation (2-1) becomes:

$$I_d(\tau) = I_S + I_r + 2\sqrt{I_S I_r} Re[V_{rs}(\tau)] \quad (2\text{-}2)$$

Equation (2-2) is termed as the generalized interference law for partially coherence light. In this equation, first two terms represent the portion of detected light which results from

the autocorrelation of sample arm beam and reference arm beam, respectively. But the third term denotes the mutual interference or cross correlation between two optical fields. $V_{rs}(\tau)$ is the normalized mutual coherence function and it contains the information about the degree of coherence between the reference and sample arm optical fields. The amplitude of the last arm represents the amplitude of the interference fringes detected at the detector and this amplitude depends on the optical path difference or time delay between reference arm position and the position of different scatterers inside the sample. In this way, the mutual coherence function contains the information about the structure of the sample. Mutual coherence function (normalized), $V_{rs}(\tau)$ can be expressed as:

$$V_{rs}(\tau) = \frac{\langle E_S(t) E_r^*(t+\tau) \rangle}{\sqrt{I_S I_r}} \tag{2-3}$$

As equation (2-2) takes into account only the real component of $V_{rs}(\tau)$, we can rewrite equation (2-2) as follows:

$$I_d(\tau) = I_S + I_r + 2\sqrt{I_S I_r}|V_{tc}(\tau)| \cos(2\pi \upsilon_0 \tau) \tag{2-4}$$

The argument of cosine function in (2-4) is the corresponding phase difference for the optical path difference between two arms and υ_0 is the center optical frequency of the light source. Later on, we will consider the entire spectrum of the source to obtain the total detected intensity. Spatial coherence is ignored from the mutual coherence function as we are mostly interested in temporal coherence between two beams. Therefore, mutual coherence function in equation (2-2) is replaced by temporal coherence function, $V_{tc}(\tau)$.

This temporal coherence function, according to Wiener-Khintcine theorem, is the Fourier transform of power spectral density S(υ) of the light source:

$$V_{tc}(\tau) = \int_0^{\infty} S(\upsilon) \exp(-j2\pi\tau)\, d\upsilon \tag{2-5}$$

Now it can be inferred from equation (2-4) and (2-5) that the properties of source spectrum like shape, width, and center wavelength have a very significant impact on the system's sensitivity of resolving very small phase differences due to the difference in optical path delay lines. This, in turn, signifies how source spectrum plays a major role in determining the axial or depth resolution of an OCT system. Now for convenience, if we express detected intensity as a function of optical path difference ($\Delta z = \Delta l$), we get:

$$I_d(\Delta l) = I_S + I_r + 2\sqrt{I_S I_r}|V_{tc}(\Delta l)| \cos(k_0 \Delta l) \tag{2-6}$$

As we have switched from time domain (τ) to space domain (Δz or Δl), equivalently frequency is now replaced by its corresponding average wave number, which holds the relationship as: $k_0 = 2\pi/\lambda_0 = 2\pi/(c/f_0)$. All the calculations till the derivation of equation (2-6) considered the sample as a perfectly reflecting mirror. To obtain a mathematical representation of OCT system for a more realistic situation, we will consider the sample as a structure having multiple layers of non-uniform thickness with varying reflectivity at different layers. Due to this consideration, now the optical path measurement for sample arm will be:

$$l_s{}' = l_s + \sum_{m=1}^{N} n_m\, l_m \tag{2-7}$$

Here N is the number of layers in the sample and n_m and l_m are the group refractive index and thickness of m-th layer of that sample. Because of this change in expression of optical path in sample arm, the detected electric field which is backscattered from the sample arm will be also modified. By replacing the $E_s'(t)$ term in equation (2-1), we can derive the following expression:

$$I_d(l_s, l_r) = I_S + I_r + 2\sqrt{I_S I_r}\int_{-\infty}^{\infty}\sqrt{R(l_s)}|V_{tc}(\Delta l)|\cos(k_0\Delta l)dl \quad (2\text{-}8)$$

Here $R(l_s)$ is the normalized path length resolved diffuse reflectance which represents the fraction of power backscattered from the particular location at l_s in the sample. The integration over the entire length of the sample gives the total reflected power from the sample arm and the third term in equation (2-8) now gives us the mutual coherence function for the entire effective reflective length of the sample. From the concept of convolution, we can rewrite the last term of above equation in terms of convolution of two functions:

$$I_d(l_s, l_r) = I_S + I_r + 2\sqrt{I_S I_r}\,[\sqrt{R(l_s)} \otimes G(\Delta l)] \quad (2\text{-}9)$$

Here $G(\Delta l)$ is the coherence function for an ideal situation where the sample is a perfectly reflecting mirror and this is expressed as:

$$G(\Delta l) = |V_{tc}(\Delta l)|\cos(k_0\Delta l) \quad (2\text{-}10)$$

Or we can replace $V_{tc}(\tau)$ with its full expression in terms of $\omega=2\pi f$, and Δl with time, τ, which yields:

$$G(\Delta l) = \int_0^\infty S(v) \exp(-j2\pi\tau) \cos(k_0 \Delta l) dv \quad (2\text{-}11)$$

Here G (Δl) is the system response for only one single reflector at a location l_s and this is known as the point spread function or PSF of the system. So, in equation (2-9), the convolution between this PSF and the path length resolved reflectance of the sample, $R(l_s)$, implies that the last term gives the system response to the sample reflectance variations at different depths and OCT takes the advantage of this reflectance contrast in mapping the sample microstructures according to their location and reflectance, which eventually forms an OCT image of that sample.

Time Domain OCT vs. Fourier Domain OCT

The OCT principle described above requires the scanning of reference arm back and forth for imaging in axial direction of sample. This is because interference between backscattered light from reference and sample arm is observed only when the path difference between them is within the coherence length of the source, which is termed as "coherence gating". So, in order to image the entire depth of the sample, reference arm has to be scanned over time. This general modality of OCT is known as time domain OCT (TD-OCT) [97, 98]. The mathematical expression for detected intensity in detector for a particular reference mirror position will be:

From (2-8):

$$I_d(l_r, l_s) = \underbrace{I_S + I_r}_{\text{DC or Autocorrelation Terms}} + 2\sqrt{I_S I_r} \underbrace{\int_{-\infty}^{\infty} \sqrt{R(l_s)}}_{\text{Normalized Path Length Resolved Reflectance}} \underbrace{|V_{tc}(\Delta l)|}_{\text{Temporal Coherence Function}} \underbrace{\cos(k_0 \Delta l) dl}_{\text{Point Spread Function (PSF)}} \quad (2\text{-}12)$$

Now, if we consider N finite number of reflecting surfaces along the depth of the sample and the corresponding path difference for each surface is, $\Delta l_i = l_r - l_{si}$, then the expression for the detected signal (avoiding DC terms) becomes:

$$I_{d(signal)}(l_r) = 2\sqrt{I_S I_r} \sum_{i=1}^{N} |V_{tc}(l_r - l_{si})| \cos[k_0(l_r - l_{si})] \quad (2\text{-}13)$$

After scanning for a range of l_r distances, obtained data can be processed to form a depth scan along the optic axis. This is one A-scan in TD-OCT system. Now by using lateral scanning, more depth profiles can be obtained. Subsequently, this 2D scan forms a cross sectional image of the sample.

One limitation of TD-OCT is its low imaging speed due to the requirement of mechanical scanning of reference mirror. Fourier domain OCT (FD-OCT) is another modality of OCT where no mechanical movement of reference arm is required, i.e. the reference arm length is kept fixed. The detector detects the wavenumber-dependent current and by using Fourier analysis, that detected output is converted to internal sample reflectivity

profile at different depths [i.e. $R(l_s)$ term in equation (2-12)]. Now depending on the detection process, FD-OCT has two different modalities. One is spectral domain OCT (SD-OCT) where a broadband light source is used and the single photodetector is replaced by a spectrometer consisting of a diffraction grating, a focusing lens and an array of detectors. The spectrometer collects all the spectral components of detected light at the same time and Fourier transform of that spectrum gives the depth profile along the optic axis. The other kind is known as swept source OCT (SS-OCT) where the spectral components are detected sequentially by using a single photodetector while synchronously sweeping the wavelength of a swept laser source. FD-OCT has the advantage of higher imaging speed and also increased signal-to-noise ratio (SNR) compared to TD-OCT [97, 98].

Spectral Domain Optical Coherence Tomography

In spectral domain OCT, the single photodetector of TD-OCT is replaced by a spectrometer. The diffraction grating in that spectrometer disperses different wavelengths of the detected light in different angle and thus it forms a spectrum. The camera with array of detectors detects this spectrum. The expression of this spectrum can be derived by expressing Equation (2 – 13) as below [97]:

$$I_d(k) = 2\sqrt{I_S I_r}\ \sum_{i=1}^{N} S(k)\cos[\,k(l_r - l_{si})] \qquad (2\text{-}14)$$

Here, $I_d(k)$ is the detected intensity for wavenumber k where $k = 2\pi/\lambda$. S(k) is the normalized Gaussian function which denotes the power spectral density function of the

source and it is related to temporal coherence function of Equation (2-13) by the following equation:

$$V_{tc}(l_r - l_{si}) = \int_0^\infty S(\upsilon) \exp(-j2\pi(l_r - l_{si}))\, d\upsilon \qquad (2\text{-}15)$$

Here, υ is the optical frequency which is related to the wavelength (λ) and thus related to the wavenumber (k). So, temporal coherence function is the Fourier transform of source spectrum. But in SD-OCT, light is dispersed first and then is detected as individual wavenumber component. Hence, in Equation (2-14), only the k-th component of the spectrum is shown and thus we replace V_{tc} (l_r - l_{si}) of Equation (2-14) only by the k-th spectral component of source light.

In addition, if we replace the optical path lengths (l_r and l_{si}) by physical distances (z_r and z_{si}) for both reference arm and sample, Equation (2-14) can be written as:

$$I_d(k) = 2\sqrt{I_S I_r}\,[S(k)\ \textstyle\sum_{i=1}^{N} \cos\{2\,k(z_r - z_{si})\}] \qquad (2\text{-}16)$$

Equation (2-16) is the expression of detected intensity in SD-OCT. For simplicity of explanation, Gaussian shaped light source spectrum is considered as it approximates the actual shape of light source and also it has useful Fourier transform properties. So, if S(k) is Gaussian shaped, then we can write:

$$S(k) = \frac{1}{\Delta k\sqrt{\pi}}\ e^{-[\frac{k - k_0}{\Delta k}]^2} \qquad (2\text{-}17)$$

And its inverse Fourier transform is given by:

$$\gamma(z) = e^{-z^2\Delta k^2} \tag{2-18}$$

Once the spectral interferogram of Equation (2-16) is detected in the array of detectors, an inverse Fourier transform is performed for $I_d(k)$ and this gives estimated sample reflectivity profile $R(z_s=l_s/2)$ as in Equation (2-12) for TD-OCT. So, after doing inverse Fourier Transform of Equation (2-16), we get:

$$i_d(z) = 2\eta\sqrt{I_S I_r}\,[\gamma(z) \otimes \sum_{i=1}^{N} \frac{1}{2}\,\delta(z \pm 2(z_r - z_{si}))] \tag{2-19}$$

Here, η is the detector conversion efficiency, (Amp/Watts). After doing convolution by using sifting property, Equation (2-19) becomes:

$$i_d(z) = \eta\sqrt{I_S I_r}\,\sum_{i=1}^{N}\{\gamma[2(z_r - z_{si})] + \gamma[-2(z_r - z_{si})]\} \tag{2-20}$$

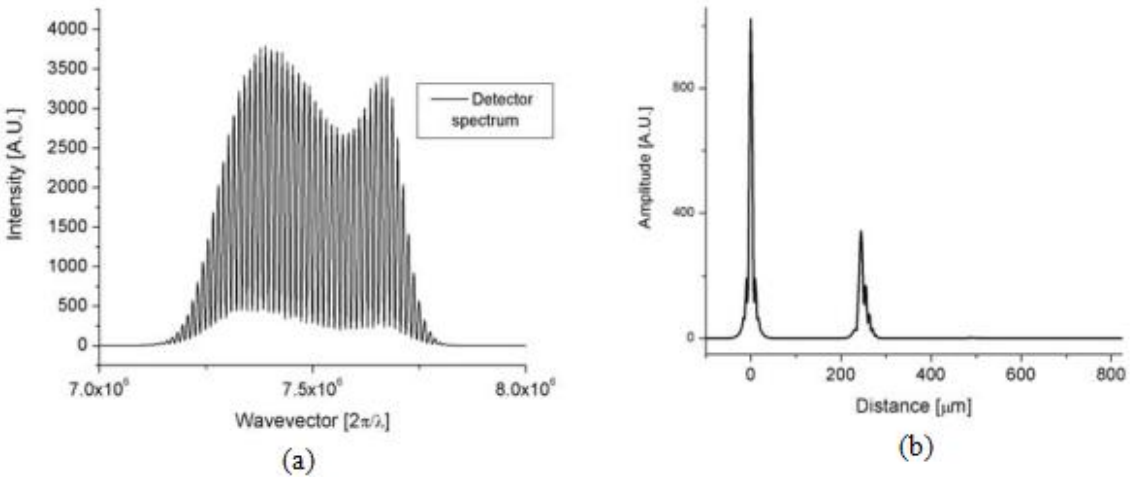

Fig. 2.3 (a) Detected spectrum in an SD-OCT system and (b) the corresponding reflectivity profile obtained after doing Fourier Transform [72].

Equation (2-19) is the final expression of the SD-OCT from where reflectivity profile of the sample from difference distances (z_{si}) along the depth can be derived. One important thing to note here is that the delta function in Equation (2-19) is convolved with $\gamma(z)$ and this broadens the delta function to a width close to the width of the coherence length of the source. As coherence length is inversely proportional to the source bandwidth, wider the spectrum of the source, narrower the reflectivity profiles will be and thus axial resolution will be improved.

So, Equation (2-20) is the expression for one A-scan in SD-OCT. Subsequent A-scans for different lateral positions along the sample length (or width) can be plotted together and this forms a cross sectional image of the sample.

Phase-resolved Optical Coherence Tomography (pr-OCT)

In phase sensitive SD-OCT, the system measures the phase variation of the detected signal [$i_d(k)$ in Equation (2-20)] for a particular reflector in the sample arm over time and in this way, it can detect very small movements (microns to picometer level) of that reflector. The phase difference can be calculated over time with respect to the phase of the detected signal at a reference time, t_0. This reference phase can be calculated as:

$$\varphi_{t=t_0}(z) = \tan^{-1}\left(\frac{Im[i_d(z)]}{Re[i_d(z)]}\right) \tag{2-21}$$

Now the movement of the reflector at time t=t, can be calculated from the expression:

$$\Delta z = \frac{\lambda_0 \Delta\varphi}{4\pi n} + \frac{m\lambda_0}{2n} \tag{2-22}$$

Here, Δz is the subresolution motion of the reflector, λ_0 is the center wavelength of the source, $\Delta\varphi$ is the phase variation over time $t - t_0$, n is the refractive index and m is an integer number. First term accounts for the corresponding distance for the phase difference, $\Delta\varphi$ for the center wavelength and second term denotes the integer multiple of half wavelengths which accounts for phase wrapping.

A good way to eliminate the common mode noise of the interferometer is to consider two reflectors (one at the location of interest and another as a reference) in the sample arm in two preferred depths and then observe the change in phase difference between the signals from those two reflectors over time. The expression of the phase difference for an instance to time can be expressed as:

$$\Delta\varphi(z) = \varphi_1(z_{ref}) - \varphi_1(z) \tag{2 – 23}$$

Now if the phase difference is observed over time, we obtain,

$$\Delta\varphi(z) = (\varphi_1(z_{ref}) - \varphi_1(z)) - (\varphi_2(z_{ref}) - \varphi_2(z)) \tag{2-24}$$

Or, $$\Delta\varphi(z) = \varphi_2(z) - \varphi_1(z) \tag{2-25}$$

A significant factor in phase calculation is the presence of noise in the system. For correct detection of phase of the detected signal, signal-to-noise ratio (SNR) has to be above a certain threshold because otherwise the induced phase noise will appear in the detection process and thus may be mistakenly represented as the movement of the reflector. Phase sensitivity has an explicit relationship with SNR where phase variance is inversely proportional to the signal-to-noise ratio (SNR) [106]:

$$\langle \Delta\varphi^2 \rangle \propto \frac{1}{2(SNR)} \tag{2-26}$$

Once the phase difference over time is recorded, observed change in the phase difference can be readily expressed in terms of spatial movement by using equation (2-22). Necessary phase adjustments will be required in order to get rid of the phase wrapping. So, in brief, this is how phase sensitive SD-OCT can detect very small transient movements of the sample.

2. Applications of OCT

Since the first appearance in literature in 1991, OCT has been gaining significant interest in the imaging research and recently it has established itself as one of the major biomedical imaging techniques. OCT has emerging applications in various fields of research, such as ophthalmology [73, 76, 78-80], cardiology [77], neuroimaging [81-82, 64], dental imaging [83, 84], dermatology [85], developmental Biology [86-88], tissue engineering [89-90], nanodevices [91-93], Materials [94-95], etc. The key advantage of OCT is that it can provide cross sectional images of biological tissues at similar

resolutions as histology images. This "optical biopsy" requires no contact with the tissue and thus it is a minimally invasive imaging technique. In addition to the advantage in resolution and noninvasiveness, OCT can also do video rate imaging and thus it has potential applications where real time imaging is required [17-18]. In neuroimaging, current methods like CT-scan, MRI and PET-scan provide excellent images of the biological tissues. However, those images lack the resolution and speed to image in cellular/neuronal level in real time. In contrast, OCT can provide submicron resolution cross-sectional and volumetric images of nerve bundles at real time imaging speed. So, optical coherence tomography has great potentials in near future to be one of the key major structural and functional neuroimaging methods.

3. OCT for Neural Recording:

Although the mechanism of scattering changes during action potential propagation is not well understood till now, results from most of the recent studies indicate that activity induced rapid transient thickness change of nerve is one of the main sources of these optical changes [62, 66-71]. Recently developed new technologies such as optical coherence tomography (OCT), also known as low coherence reflectometry (LCR), have allowed for novel methods of observing structural and optical changes associated with nerve activity. OCT/LCR distinguish themselves from laser interferometry by their sectioning capability. Phase changes are only measured at a particular location along the beam. LCR was used independently by Akkin *et al.* and Fang-Yen *et al.* in 2004 to

observe a thickness change during nerve activity [64, 65]. Akkin *et al*. used a phase-sensitive LCR system to demonstrate a transient neural surface displacement, coincident with the action potential arriving to the optical measurement site. Akkin's configuration used two orthogonal polarization states incident on the sample. One state was aligned to provide a reflection from a reference glass surface above the nerve tissue. The second polarization state was aligned to provide a reflection from the saline bath/nerve tissue interface. The experimental configuration detected phase changes between these orthogonal polarized interference fringes, and was able to detect transient motion on the order of 0.4-1.0 nm of the saline bath/nerve tissue interface on a time scale of 1-2 ms. Fang-Yen *et al.* used a similar configuration that also measured the displacement with respect to a reference glass surface. They detected a 5 nm swelling with duration of 10 ms on a lobster nerve, indicating a compound response. These provided the first measurement of these fast transient changes detected by an OCT/LCR configuration. A drawback of these configurations was that a phase difference could only be measured between two fixed locations, in this case between a glass reference surface and one surface of the nerve. While these methodologies are highly sensitive and capable of detection of thickness changes on a rapid time-scale, they can only observe these changes at a particular point through changes in displacement between the reference surface and the nerve. They lack the capability to image the entire cross section of the nerve in order to obtain a more direct measure of the transient thickness change of the nerve itself. Furthermore, these studies required averaging of few hundred trials in order to improve the SNR.

Rapid development of spectral-domain OCT (SD-OCT) has revolutionized OCT imaging. A recent study demonstrated a 150 fold sensitivity improvement over conventional OCT and showed video-rate 3-D imaging of the human retina *in vivo*, which constituted a speed increase by a factor of 73 and a resolution improvement of nearly a factor of 2 over state of the art commercial systems [72-73]. The sensitivity improvement, combined with the absence of mechanical scanning in the reference arm, has improved the phase stability to 25 picometer and the time resolution to 35 microseconds [74]. SD-OCT acquires a depth profile in a single shot and is capable of simultaneously detecting a phase difference between arbitrary points along the depth profile. Phase differences between the top and bottom surface of a nerve bundle can be detected, and in addition, a structural image can be recorded to identify a nerve bundle location prior to action potential measurements.

4. 800nm OCT System Design and Specification:

Basic instrument/parts specification

Maximum Camera Acquisition Rate	144000 A-lines/sec	*Source*	Ti:AlO_2 Laser
Camera Pixel Size	10µm	*Source Center Wavelength*	800nm
Total Camera Pixels	4096	*Source FWHM Bandwidth*	170nm
Spectrometer Grating	1200lpm	*Collimators*	X7, X11
Spectrometer Lens	f = 150mm, 4 inch	*Microscope objective*	Olympus, 4X, NA = 0.16
Spectrometer PBS Cube Size	4 inch	*Microscope Tube Lens*	f = 150mm
Isolator	830	*Common path pBS*	70:30

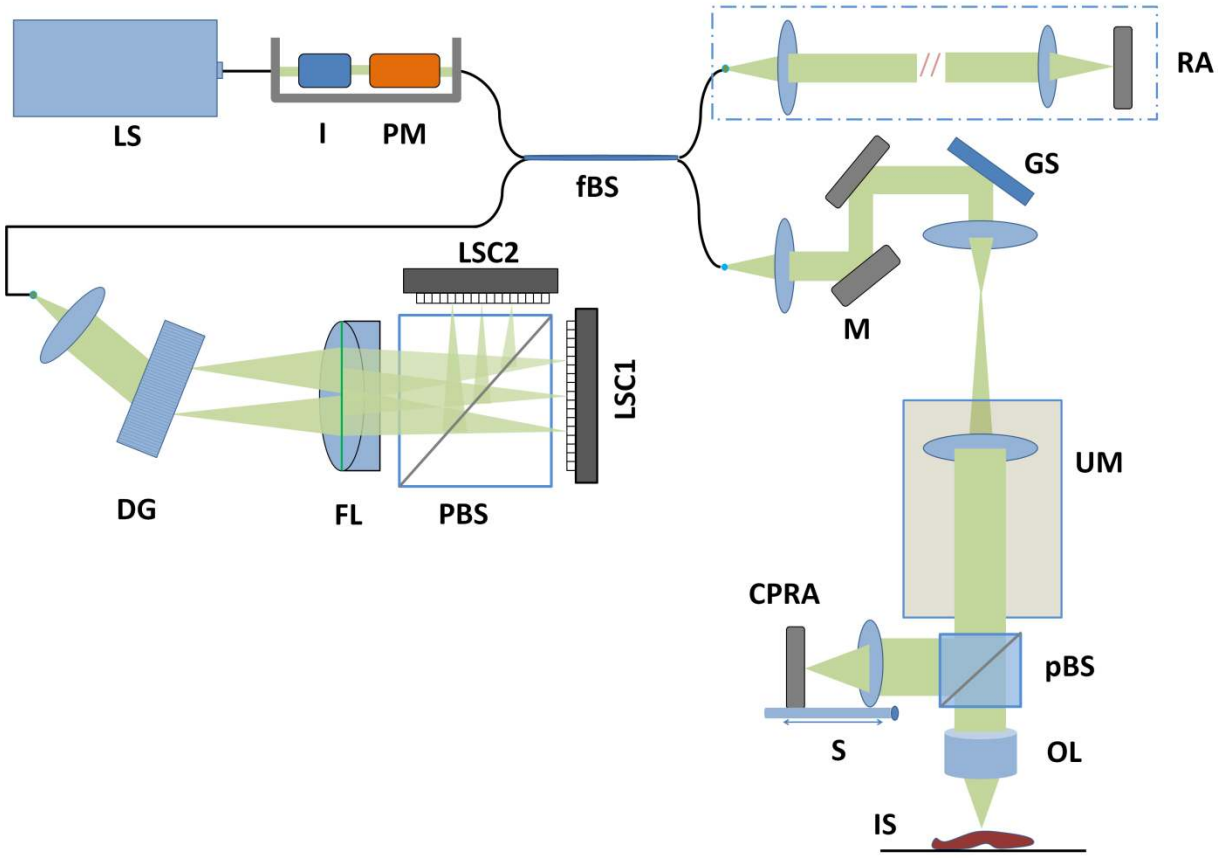

Fig. 2.4 Overall setup of the dual configuration 800nm pr-OCT system (both reference arm and common-path based configurations). LS: light source, I: isolator, PM polarization modulator, fBS: fiber beam splitter, RA: reference arm, M: Miror, GS: galvo scanner, UM: upright microscope, CPRA: common-path reference arm, pBS: plate beam splitter, S: 1D stage, OL: objective lens, IS: imaging sample, DG: diffraction grating, FL: focusing lens, PBS: polarization beam splitter, LSC: line scan camera.

System Description

An 800nm wavelength based dual configuration spectral domain OCT (SD-OCT) was used in this study. A schemtatic is shown in Figure 2.4. A Ti:Saph broadband mode locked laser (Femtolasers, Inc., Integral OCT 2709, center wavelength 804nm,

bandwidth 170nm) was used as the light source. The source light is sent to the reference and sample arms by a 2x2 fiber-based beam splitter, and backscattered lights from both arms are collected by a custom built spectrometer. The reference arm is a fixed travel distance where light is finally reflected back from a mirror and this is used only for reference arm based configuration. The sample arm is incorporated on an upright microscope (Olympus, BX61) through the camera port, with raster scanning controlled with a galvanometer based scanner (Cambridge Technology, Inc., 6210H). The sample arm is incorporated with a small reference arm placed after the tube lens (for common-path configuration). A plate beam splitter (Thorlabs BS111) splits the sample arm beam into 70:30 ratio while 30% light goes to the small reference arm that consists of a lens and a mirror both mounted on a 1D moving stage. The remaining light is transmitted through an objective lens (Olympus, UPLSAPO 4x) on the sample which rests on a micromanipulator controlled stage (Sutter Instruments). The spectrometer consists of a diffraction grating (Wasatch Photonics, 1200lpmm, 830nm), a focusing lens (JenOptik Optical Systems, f=150mm), polarization beam splitter cube (Rocky Mountain Instrument Co., 4 inch Cube) and two line scan cameras (Basler sprint camera, sp4096-140km). The axial resolution of the system was measured to be 3µm in air and the lateral resolution to be 5µm with a 4x objective. The maximum acquisition speed of the line scan camera is 144000 lines/seconds and yields a temporal resolution of the order of 7µs. The detected spectrum in the camera is sent to the computer through a frame grabber (National Instrument, NI1429). Another data acquisition card (National Instrument, NI 6259) runs two BNC breakout boxes (BNC 2110 and 2120) which generate the controls

signals for the line scan camera, scanning mirrors, stimulation shutter and electrophysiology recording unit. A PCI-e chassis (Magma) accommodates all these PCI-e cards and a workstation computer is used for controlling data acquisition. A multithreaded software program written in Microsoft Visual C++ is used to synchronize all the devices during acquisition. Another computer, with CUDA enabled Tesla GPUs (C1060), is used for rapid post processing of raw data. MATLAB 2011b is used for image processing and AMIRA is used as visualization software for volume rendering and 3D analysis.

5. Acquisition Program and Post Processing:

Acquisition Program

An acquisition program was written in Visual Studio C++ (Figure 2.5). It is a multithreaded program mainly responsible for continuous data acquisition and synchronizing the entire OCT system through control signals. The programs controls the line scan cameras through TTL trigger signal and the galbanometer scanners through sawtooth signals. All these signals are designed within the program and then executed by the BNC breakout boxes through the NI 6259 DAQ card. The program also controls the polarization modulator states through TTL signals.

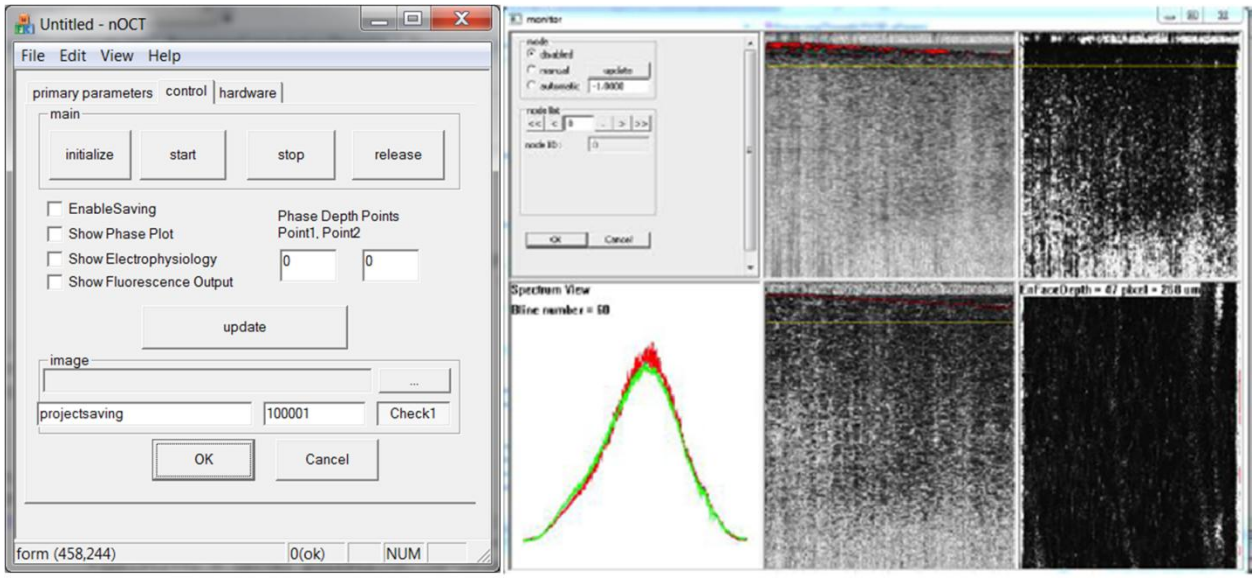

Fig. 2.5 Acquisition program graphic user interface and display windows (written in Visual C++)

In addition to continuous data acquisition and synchronization, this multithreaded program also does data processing in a different thread and displays the continuously updated OCT cross-section images on the screen. Another parallel thread operates to save the camera raw data on the computer hard disk for post processing. The programs display consists of multiple sections where different modality images and plots are displayed, such as, detected spectrum, intensity image, flow image, phase-retardation image, phase difference over time, etc.

Auto-calibration and dispersion correction GUI

A calibration procedure according to Mujat et al. has been followed to calibrate the line scan cameras [96]. In order to make the process automatic, a MATLAB graphic user interface (GUI) was developed. A snapshot of the GUI is shown below.

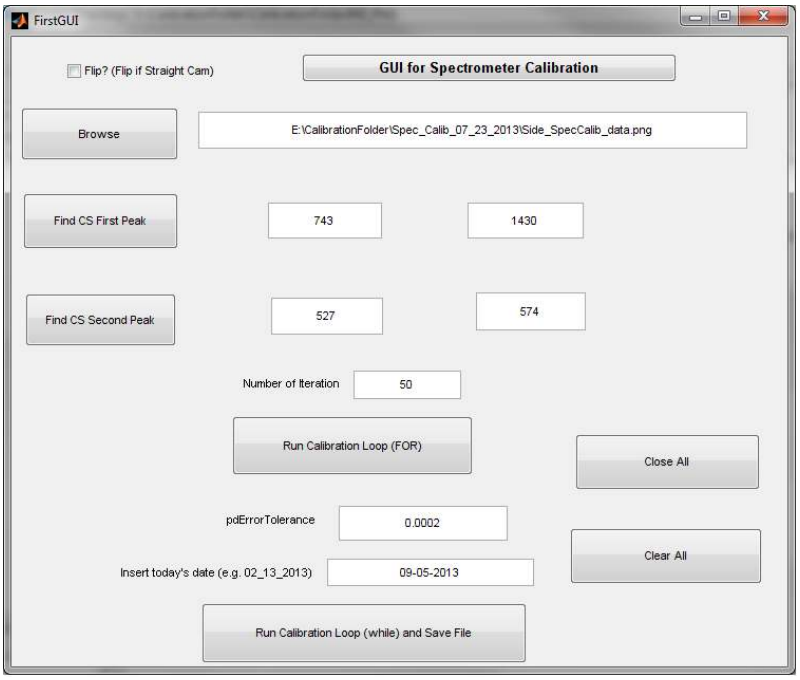

Fig. 2.6 Graphic user interface of the MATLAB program for spectrometer auto-calibration

Image Processing GUI

A graphic user interface has been created for post processing of OCT raw data and formation of cross-sectional images (Figure 2.7). A user can select all the required processing parameters from the GUI and define the quantity and location of processed images for saving. This GUI also allows visualizing the cross-sectional images of a volume from all three sectioning dimensions – xy, yz, and zx.

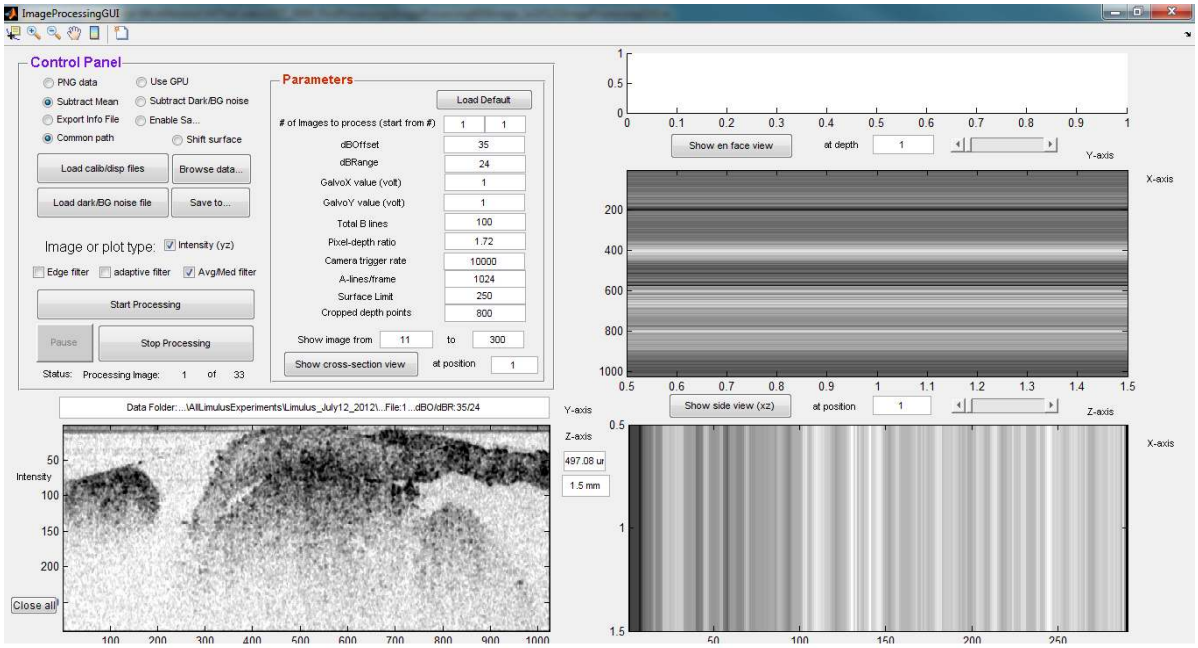

Fig. 2.7 Graphic user interface of the MATLAB program for image processing and orthoslice display

Phase analysis GUI

Another similar GUI is written for phase analysis of OCT data (Figure 2.8). 1D data were saved from M-scanning of sample (e.g. M-scan on Limulus nerve for nerve activity analysis). A user can use this GUI to select the depth layers to process for measurement of phase difference. A combination of 5 different layers can be given as input for phase analysis. The phase measurements can be also filtered for removing noise frequencies and the signal in both time and frequency domains are displayed.

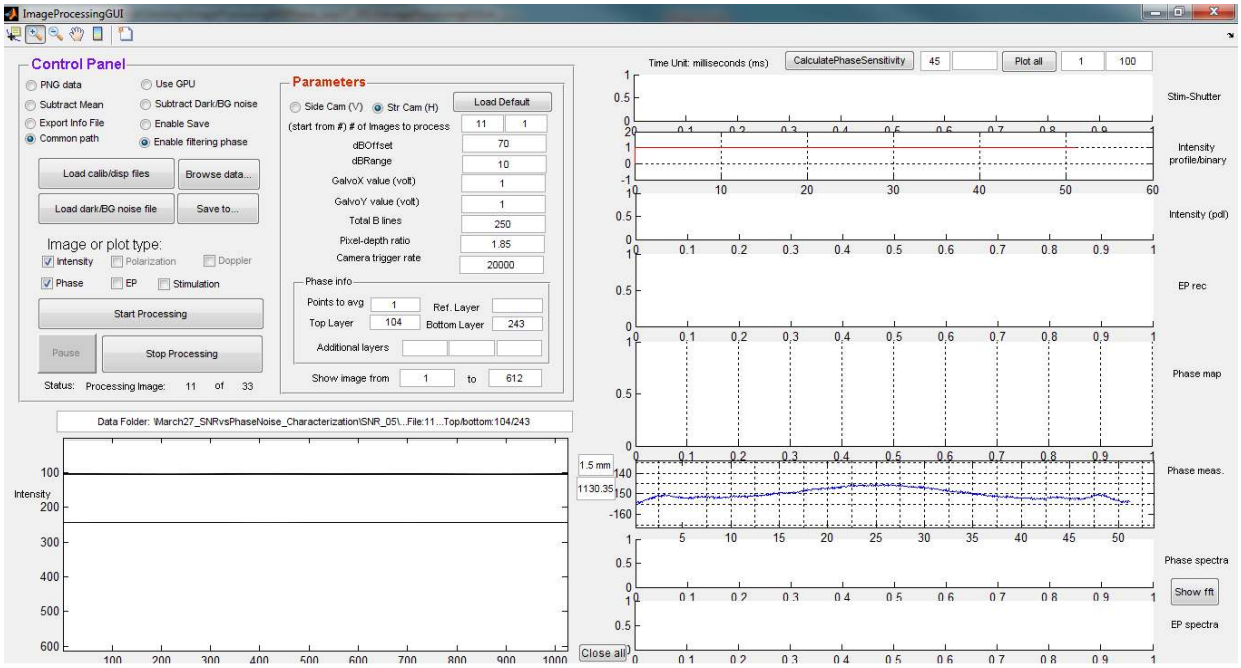

Fig. 2.8 Graphic user interface of the MATLAB program for phase analysis of OCT data

Chapter 3

Calibration, Characterization and Imaging

1. Spectrometer Calibration

In order to obtain better resolution images, spectrometers need to be calibrated first. Spectrometer calibration means having proper wavelength mapping on the camera pixels. The procedure and results of spectrometer calibration are described in next two sections.

The standard cover slip method was followed to properly map the wavelengths onto camera pixels [96]. Figure 3.1 shows an OCT depth profile of a cover slip as a sample. The peaks are not well resolved due to incorrect wavelength mapping. Figure 3.2, 3.3, 3.4 and 3.5 show important steps in calibration process. Figure 3.2 depicts the procedure where a cover slip is placed in the source arm to create two waves, one that passes through the cover slip once and another one which passes through twice. Figure 3.3 shows the modulation of source spectrum for the presence of cover slip (representing the interference between the two waves) and Figure 3.4 depicts corresponding depth profile for the source arm cover slip. The phase of this spectrum, which is expected to be linear in k-space, is shown in Figure 3.5. The goal of the calibration process is to assign wavelengths in such a way so that the error or discrepancy in phase reduces to a minimum and the linearity of phase in k-space increases in every iteration. Once the maximum error reduced to at least below a threshold (in our case, 0.0002 radians) after a

number of iterations, the spectrometer can be safely considered to be well calibrated. Figure 3.6 shows the calibrated depth profile of the same cover slip as in Figure 3.1.

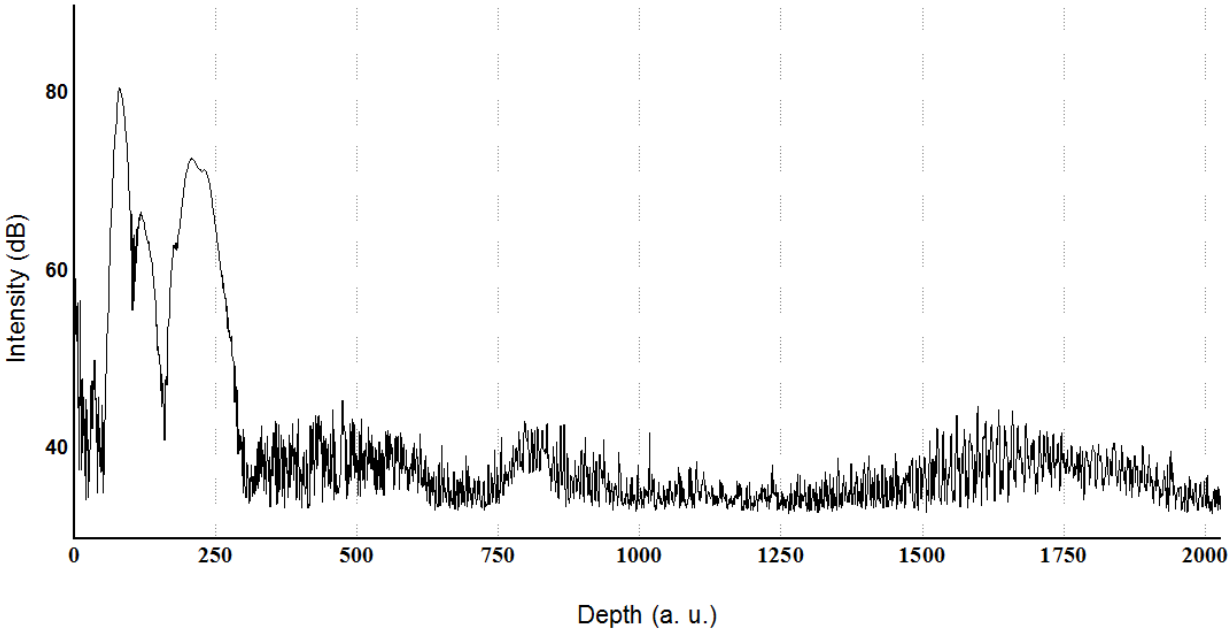

Fig. 3.1 Uncalibrated depth profile of a cover slip sample where two peaks, representing top and bottom layers of cover slip, are poorly resolved due to uncorrected wavelength assignment.

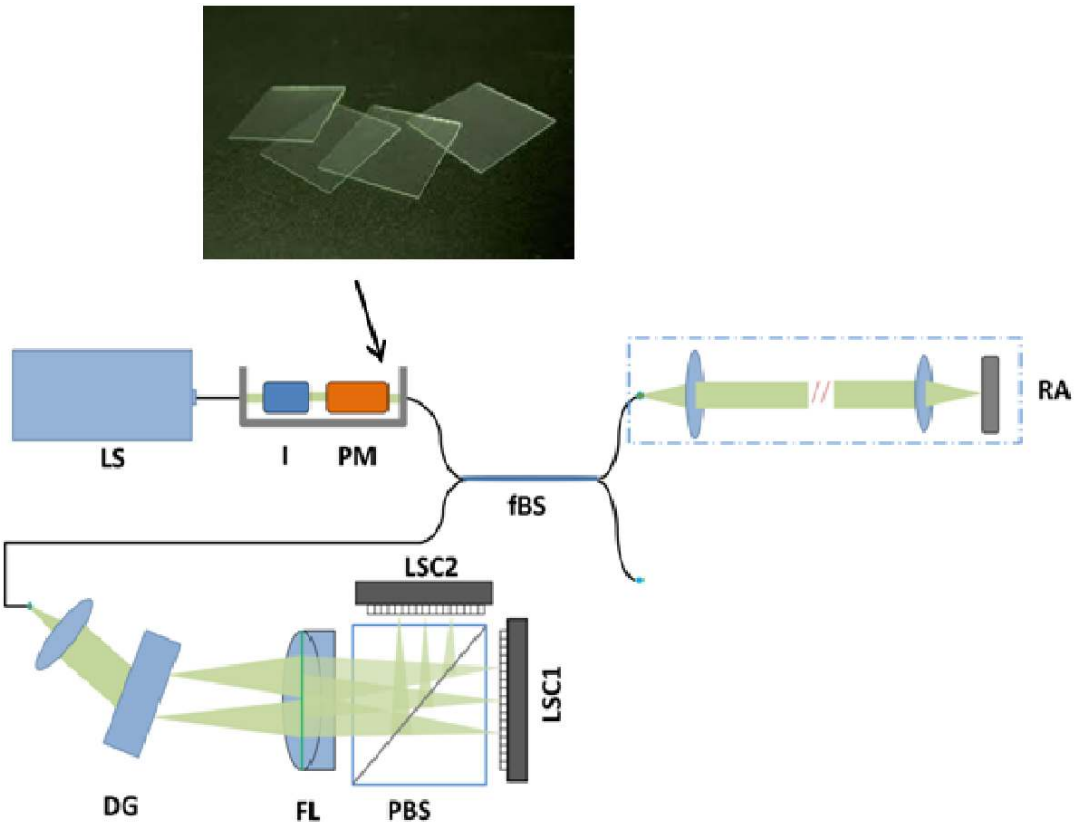

Fig. 3.2. System setup for spectrometer autocalibration using a cover slip in source arm of OCT.

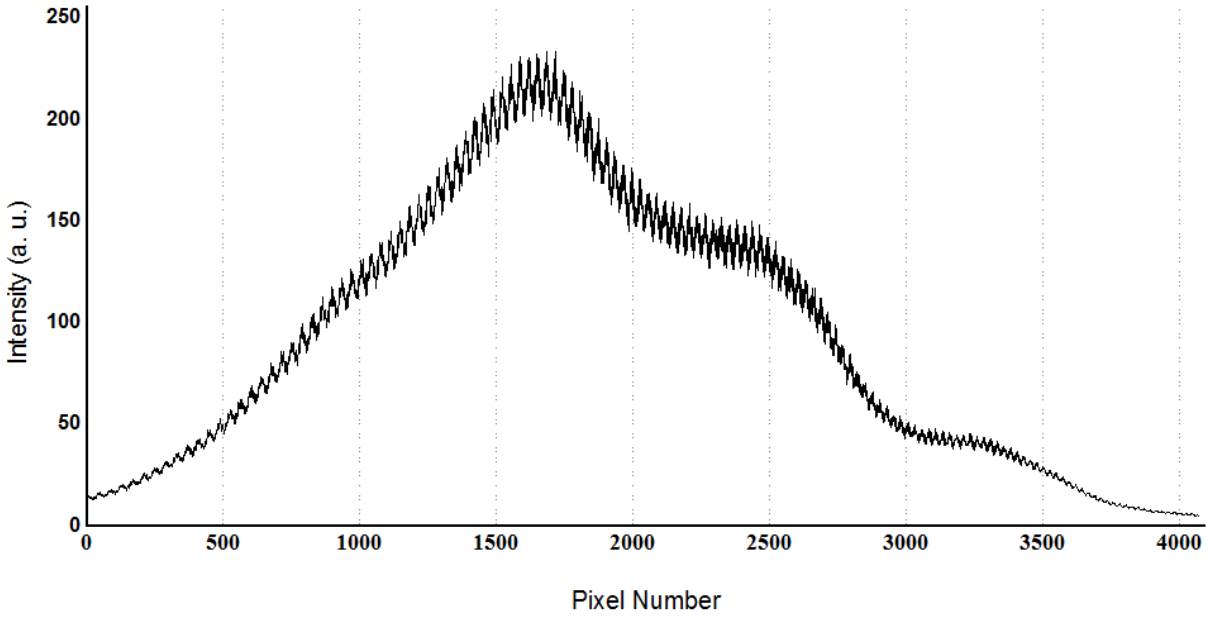

Fig 3.3. First step in calibration process. A cover slip is placed in source arm of OCT system and the detected spectrum is shown here. The sinusoidal modulation represents the interference caused by the two beams originating from the two layers of cover slip.

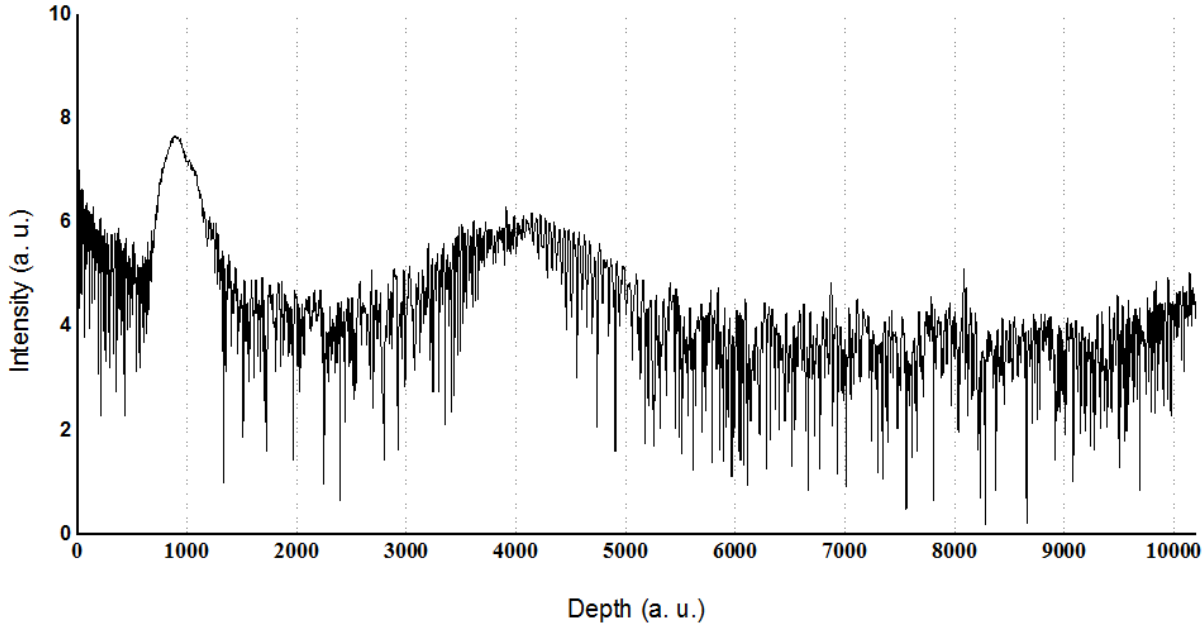

Fig. 3.4 Fast Fourier transform (FFT) of the spectrum shown in Fig. 3.2. The peak at position 1000 represents the thickness of the cover slip placed in the source arm for calibration.

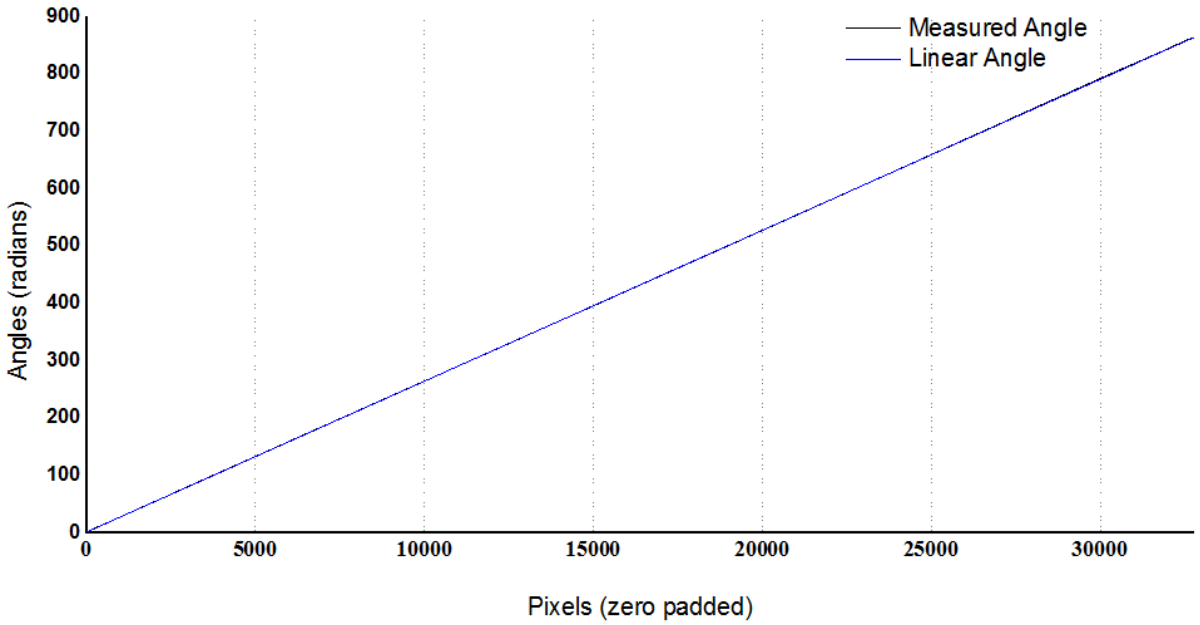

Fig. 3.5 Unwrapped angle calculated from the complex depth profile of Fig. 3.3. The red curve represents the angle measured at one stage of the calibration process while the linear angle is the required angle for a fully calibrated spectrometer.

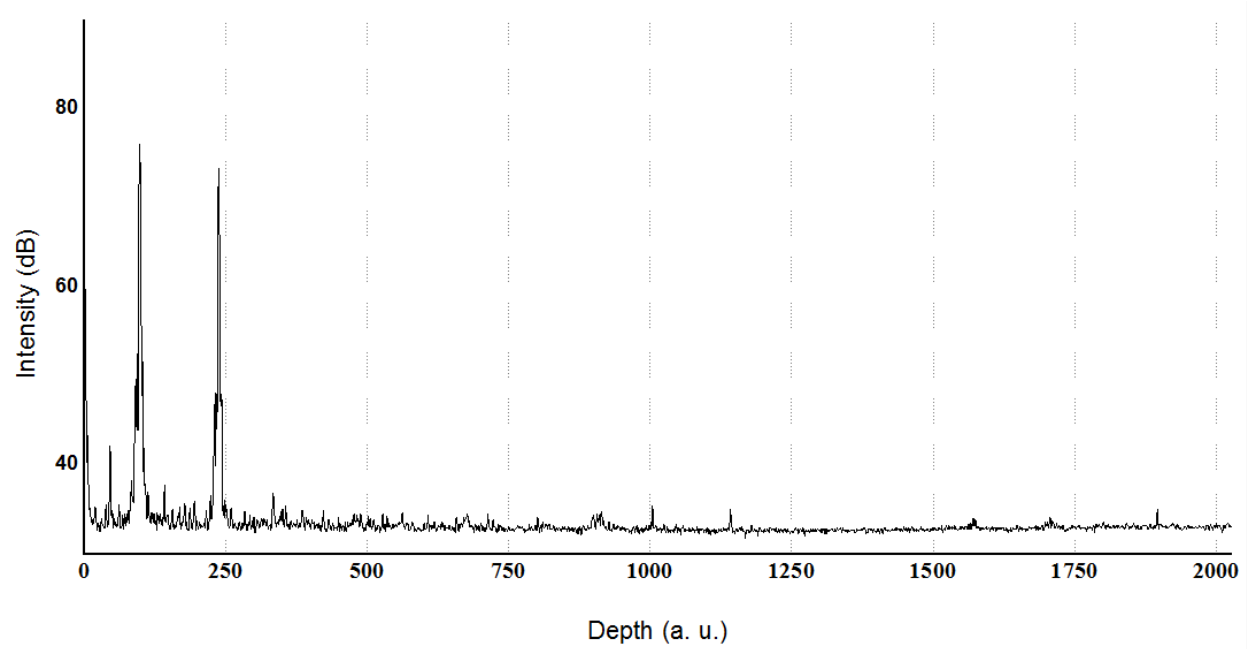

Fig. 3.6 Calibrated depth profile of a cover slip sample where two peaks, representing top and bottom layers of cover slip, are much better resolved than that in Fig. 3.1. The improved shows the effect of proper wavelength assignment.

2. Basic System Characterization

Once the OCT spectrometer is calibrated, a set of system characterization measurements is required to get the specification of the built imaging system. The basic characterization measurements are axial resolution, lateral resolution, sensitivity drop off, imaging range, and depth correction analysis.

Axial resolution

Figure 3.7 shows the depth profiles of a mirror placed in the sample arm. The peak represents the point spread function (PSF) of the system in axial direction and the magnitude of the peak refers to the reflected intensity from the mirror. As we move the mirror (sample) in the axial direction, the peak position moves accordingly and the amount of this shifting in graph exactly matches the actual movement of the sample. Axial resolution of the system is calculated from the full width half maximum (FWHM) of the PSF. Measured axial resolution was between 2.7 ~ 3μm (in air) at depth from zero to 1mm and then the resolution dropped gradually towards around 10μm. This result matches our theoretically predicted axial resolution value which is half of coherence length of the source, i.e. 4μm/2 = 2μm.

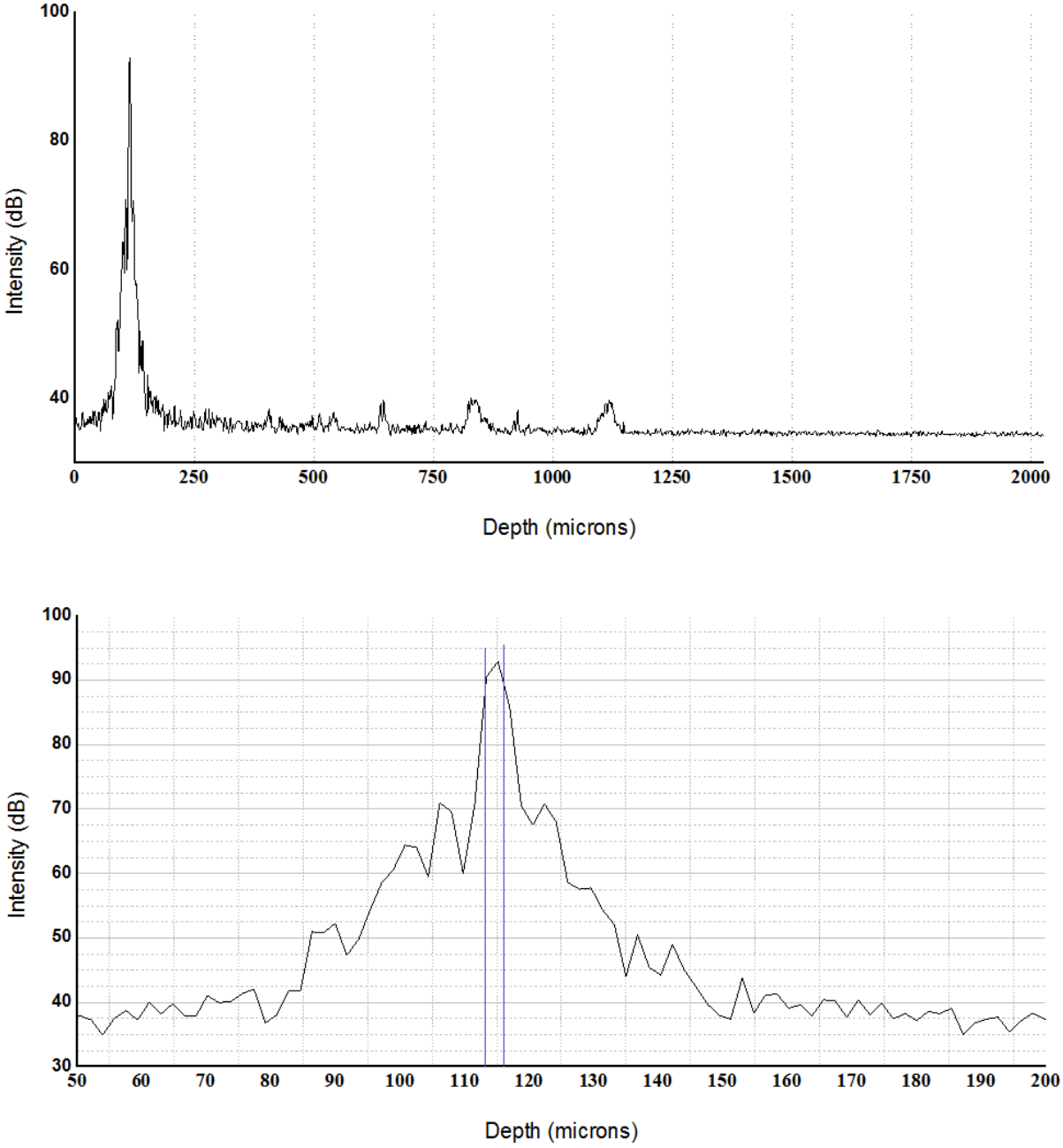

Fig. 3.7 Characterization of system axial resolution. (top) Depth profile of the sample when a mirror was placed as a sample. The distance from the zero position refers to the corresponding path difference between reference and sample arm. (bottom) The enlarged version of the peal shows how to calculate the axial resolution from the FWHM of the peak.

Lateral resolution

A US Air Force target is scanned by OCT to image the different groups of lines on it. Figure 3.8 shows such an OCT cross-sectional image of the scanned area. After averaging few depth lines to reduce noise, the average intensities along a scanned line are plotted in Figure 3.9. The low and high levels of intensities represent the transparent and non-transparent areas in USAF target, respectively. Figure 3.10 is the first derivative of intensity values and Figure 3.11 is the first derivative as in Figure 3.10 but in logarithmic scale. In Figure 3.12, FWHM of the peaks in Figure 3.10 gives us the lateral resolution of the system for the particular objective lens used in the sample arm (Olympus, 4X, USPLANO, NA = 0.16).

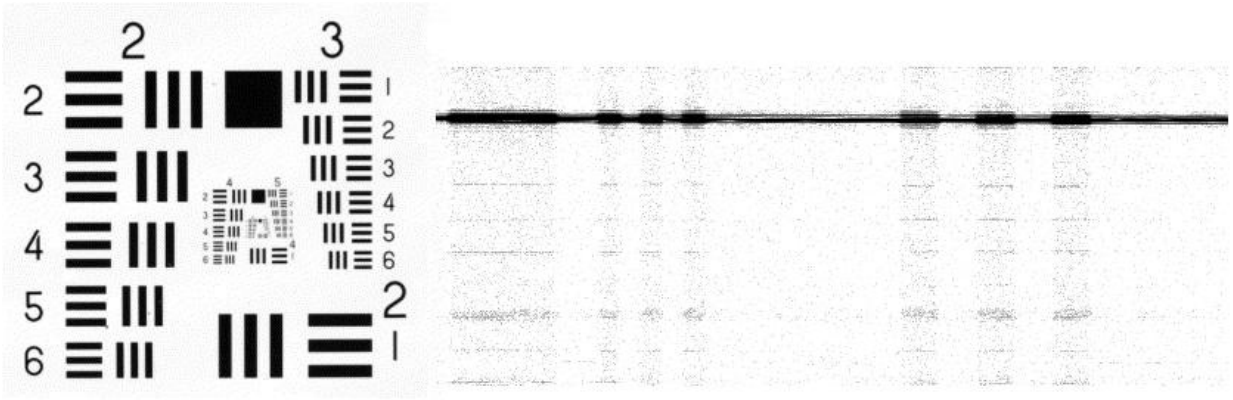

Fig. 3.8. US Air Force target imaging for lateral resolution measurement

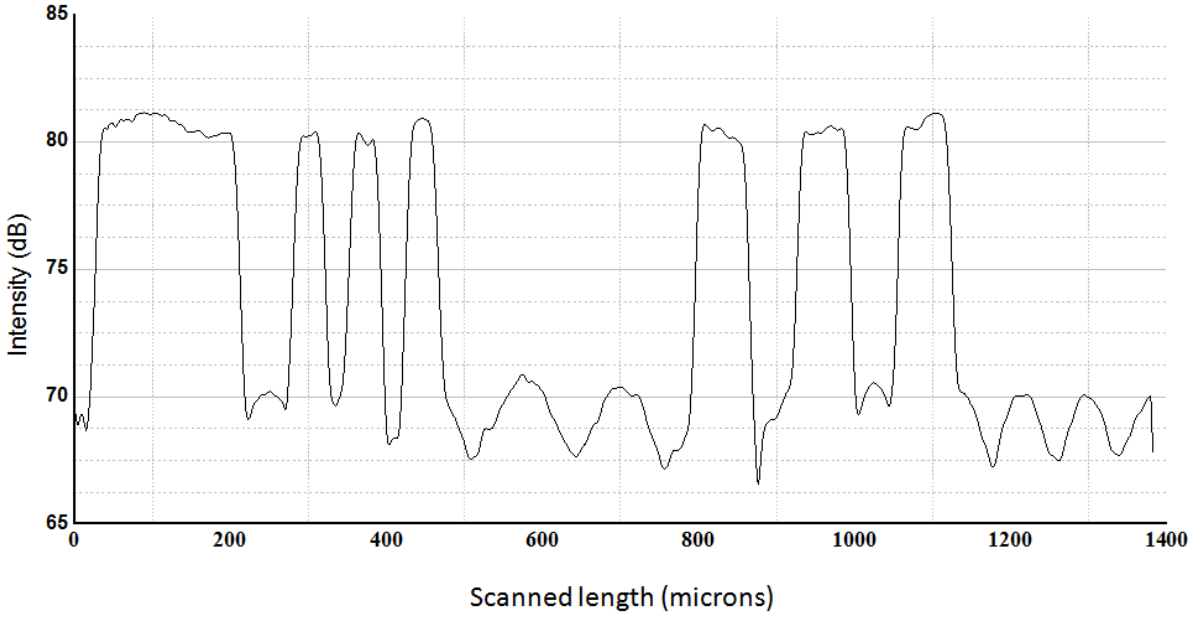

Fig. 3.9 Intensity of a line scanned across 3 different USAF line groups.

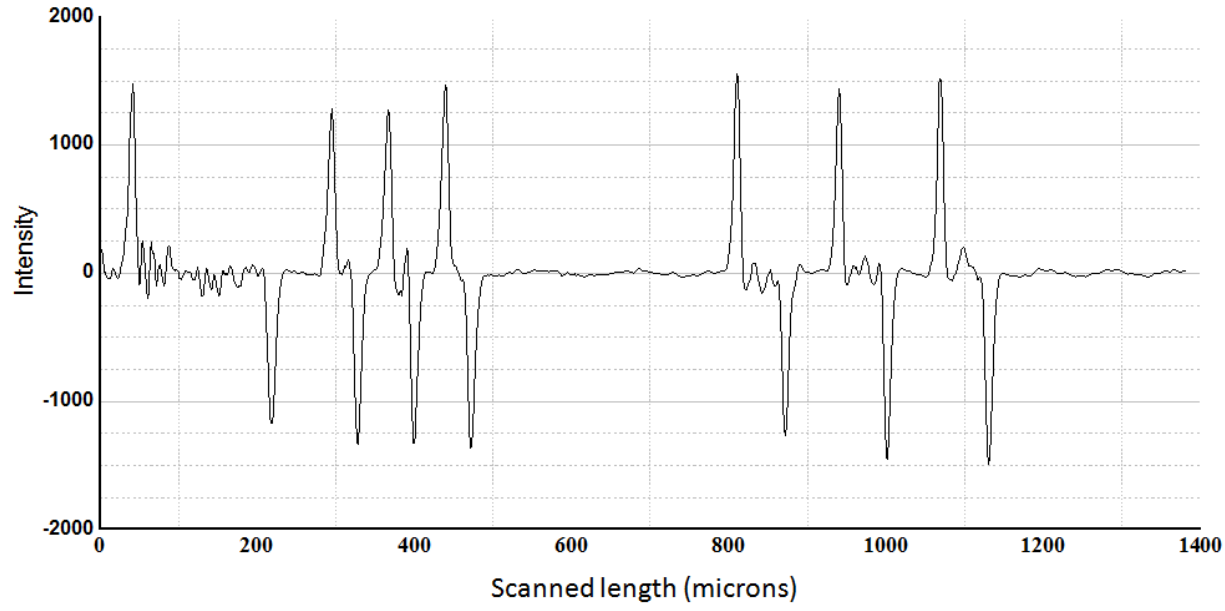

Fig. 3.10 Differentiation of the intensity plot in Fig. 3.9, the peaks represents the edges of the USAF lines.

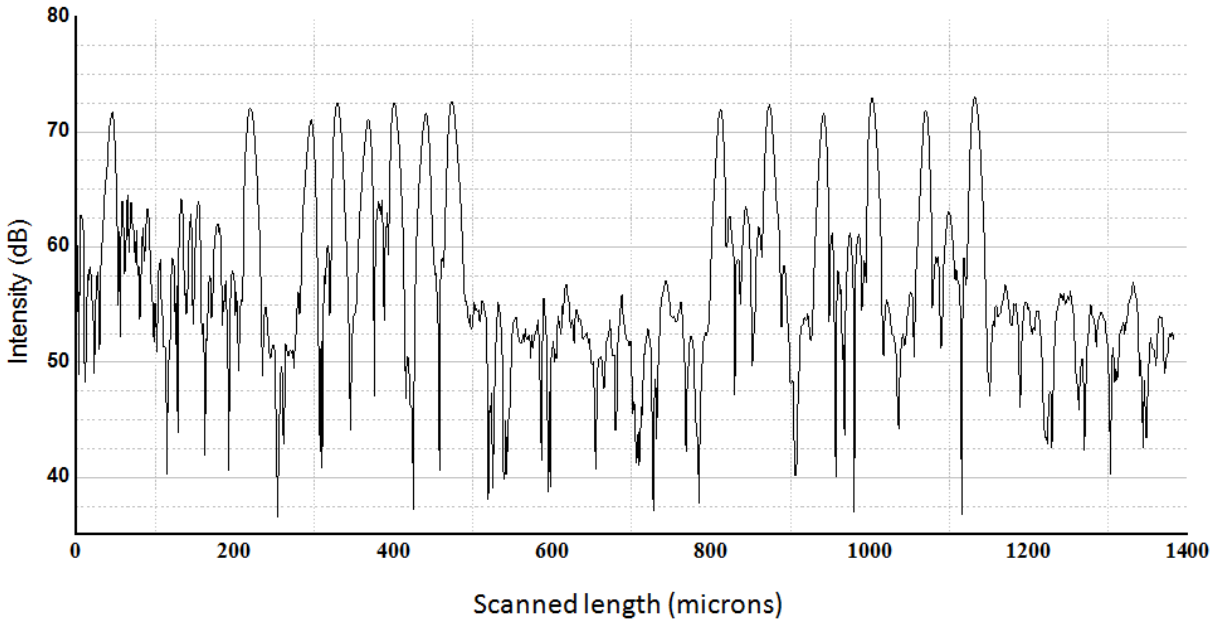

Fig. 3.11 Differentiated intensity signal of Fig 3.9 in logarithmic plot.

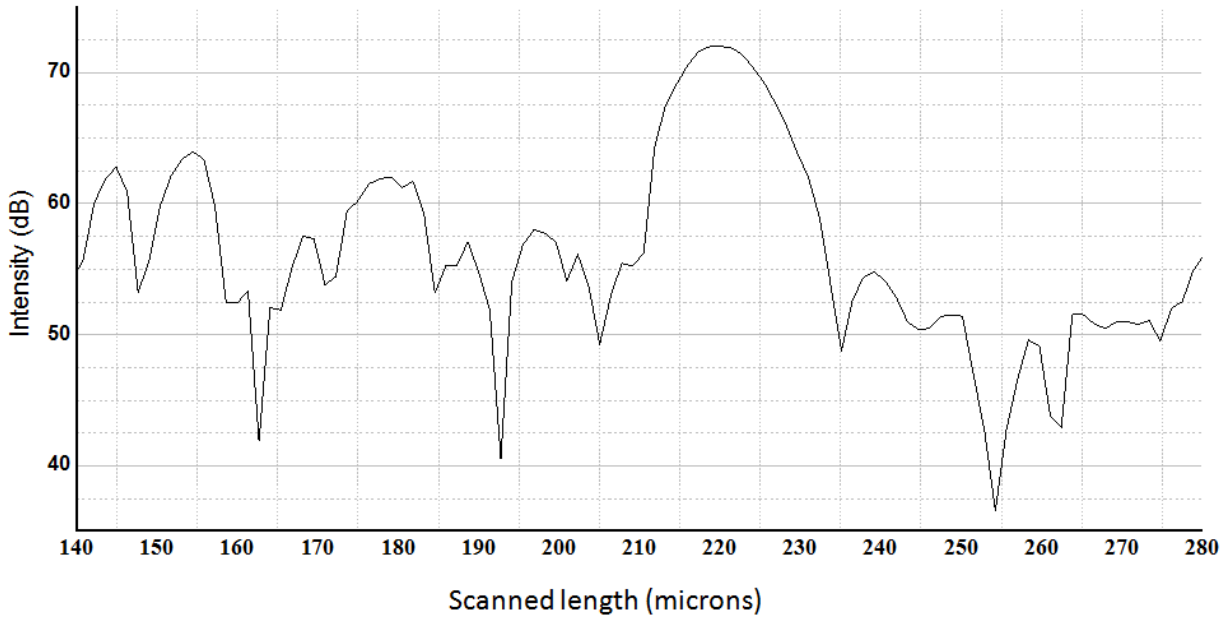

Fig. 3.12 Measurement of the system lateral resolution from the FWHM of the plot in Fig 3.11 (enlarged version).

Imaging Range

Imaging range is the maximum depth range in sample up to which the image forms without any aliasing. The mirror in the reference arm is moved gradually at a step of 20μm and data was acquired at every position. The mirror is moved until the mirror peak in OCT depth profile starts folding back at the zero position again. This defines the maximum depth range which can be imaged without any overlap or aliasing. In this case, the imaging range of the spectrometer was found to be 3.85mm which is close to the theoretically calculated value of 3.81mm.

Sensitivity drop-off and Depth Correction

The mirror was moved by 20μm at every step and data was recorded for each case. Then processed depth profiles were analyzed to measure the sensitivity drop off (signal intensity drop off). Figure 3.13 shows such depth profiles (only some are shown here) and it is apparent that the sensitivity drops off gradually as the depth increases. This drop off in sensitivity is a fundamental limitation of SD-OCT systems due to limited spectrometer resolution. As the sample is moved to deeper position (larger path length difference with reference arm), the modulation frequency of the spectrum becomes higher and less resolved by the spectrometer according to Nyquist's rule. As a result, the signal intensity drops and the axial resolution degrades. However, a good design of spectrometer can ensure that this drop off in sensitivity is with 10-15dB for 2mm imaging range. In this case, in Figure 3.13, a 12dB drop off is visible at 2.5mm imaging depth (97dB to 85dB) which demonstrates a well designed spectrometer. To overcome the

sensitivity drop off problem, we can adopt depth correction technique. By analyzing the sensitivity drop-off data, a set of correction factors can be generated for compensating the signal losses at different depths. Figure 3.14 shows the depth correction plot (in both linear and log scale).

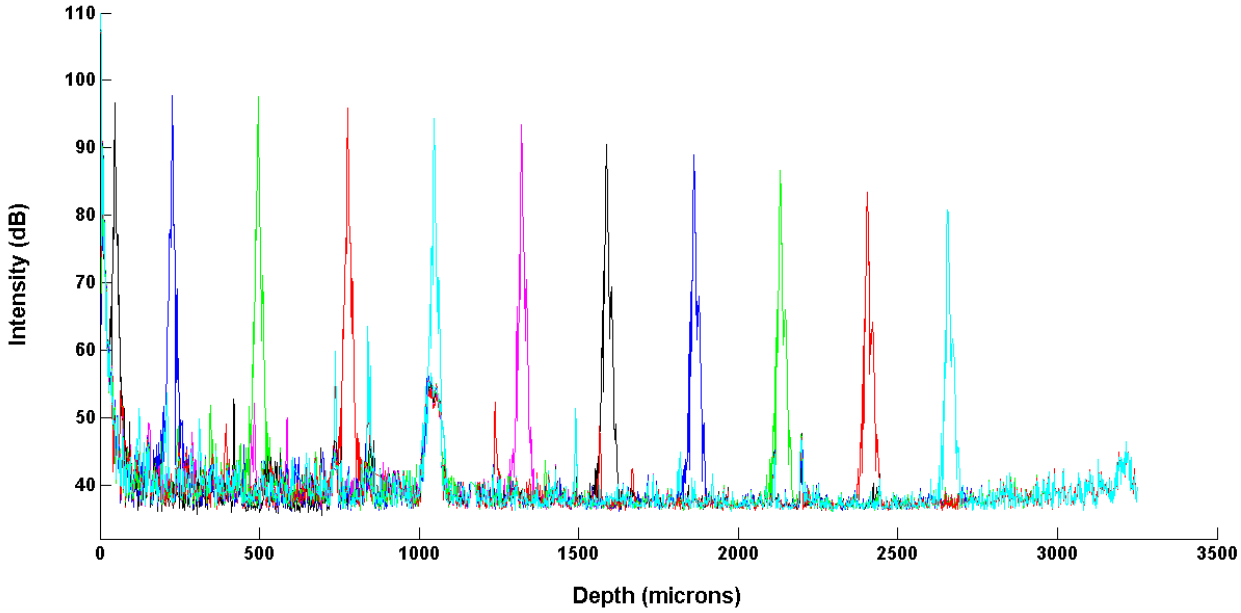

Fig 3.13 Depth profile for the same mirror as a sample but location of the mirror is moved along the optic axis. The plots showing SNR drop off at various depths of the sample.

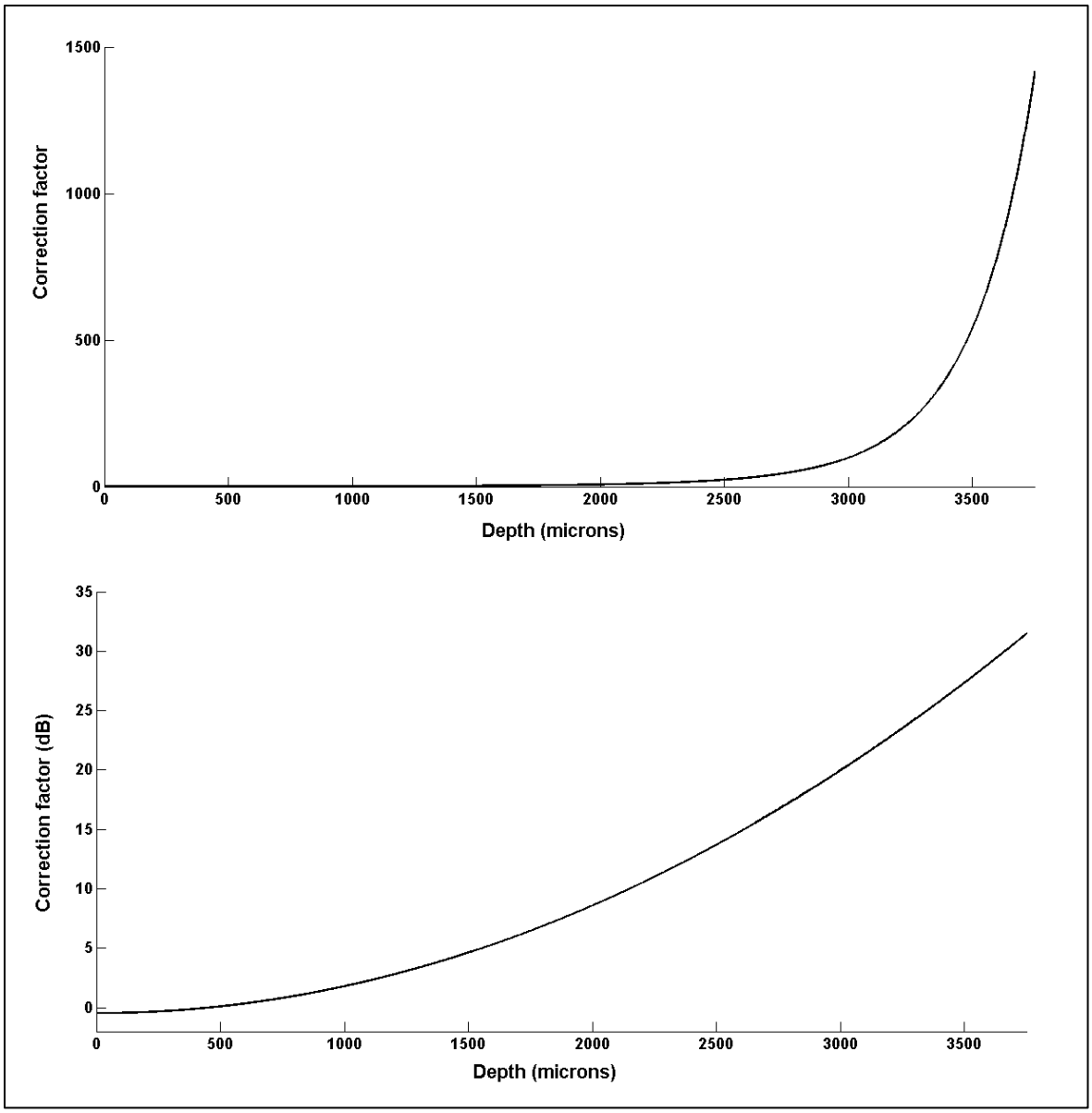

Fig. 3.14 Calculated depth correction values at different depths in order to compensate for the depth-dependent sensitivity drop-off. The values shown in both linear and log scale.

3. Phase-sensitivity Characterization

Phase-sensitivity characterization is a critical step before doing pr-OCT measurements from optic nerve. Phase noise characterization requires the measurement of phase over time from a known sample. In this case, we used a cover slip. Phase of two surfaces of cover slip (top and bottom) are extracted and the phase difference is calculated after unwrapping the phases. The standard deviation of the phase is calculated which yields an estimate of the noise in phase signal, in other words, defines the limit of minimum detectable phase change using the system.

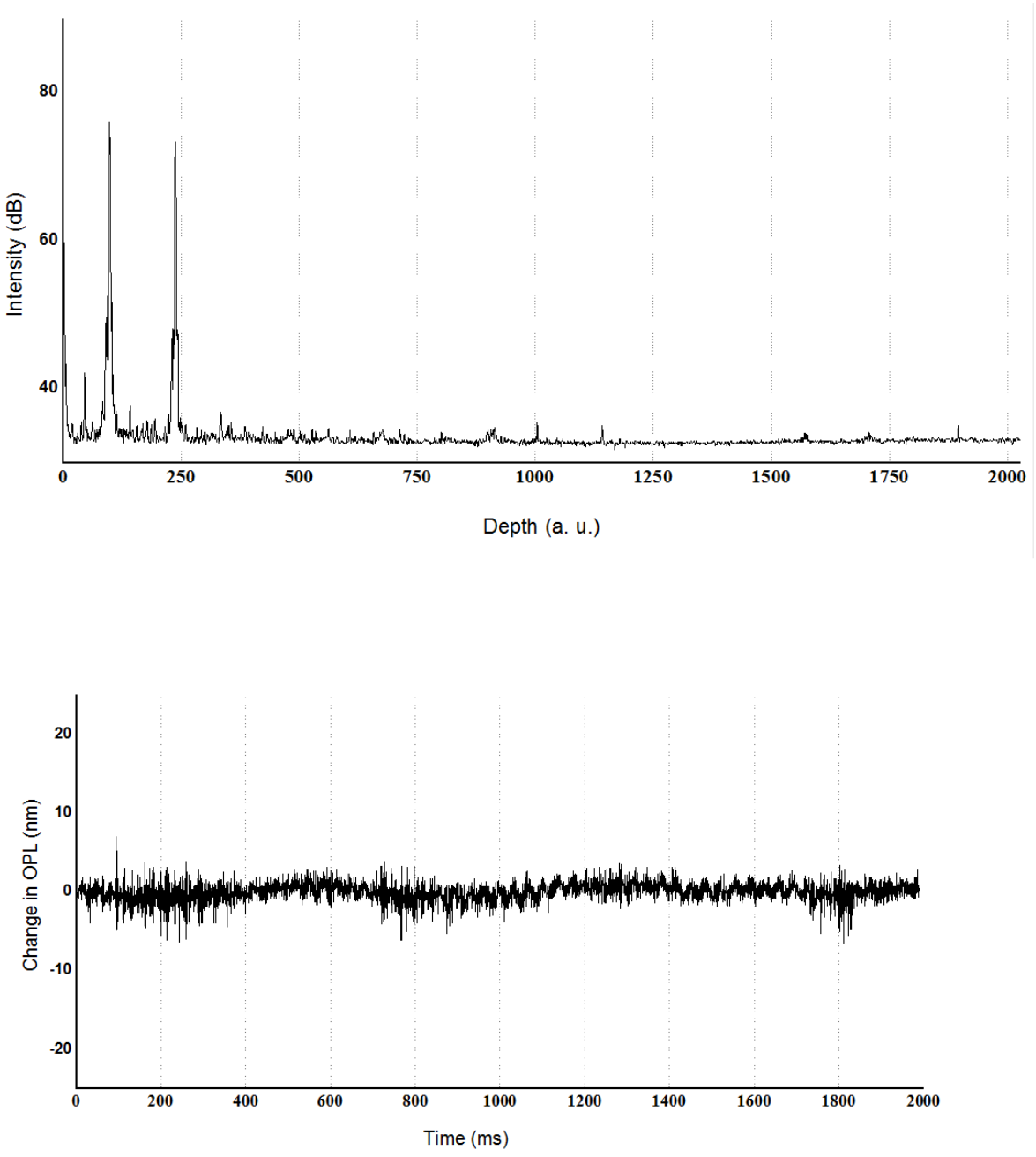

Fig. 3.15 Depth profile showing the cover slip peaks for its top and bottom layer (top). The change in phase difference between those two peaks over time. The standard deviation of these values represents the noise margin.

Phase noise from cover slip has been calculated for different signal-to-noise ratio. The measured phase noise is compared with theoretically calculated phase noise for each case. The values are listed in the table below.

Table 3.1 Measured and theoretically calculated phase noise margins

Signal-to-noise ratio (SNR)	Standard deviation of calculated phase noise (nm)	Standard deviation of measured phase noise (nm)
49.40061632	0.3052	1.7118
47.9013558	0.3627	2.0141
45.89968668	0.4567	1.9456
43.09998282	0.6304	2.8431
36.48627496	1.3499	3.1726
31.90052952	2.2887	4.0245
27.75813744	3.6873	5.8156
24.20050219	5.5538	7.1961
20.63904313	8.3688	10.7738
15.70058144	14.777	19.7749

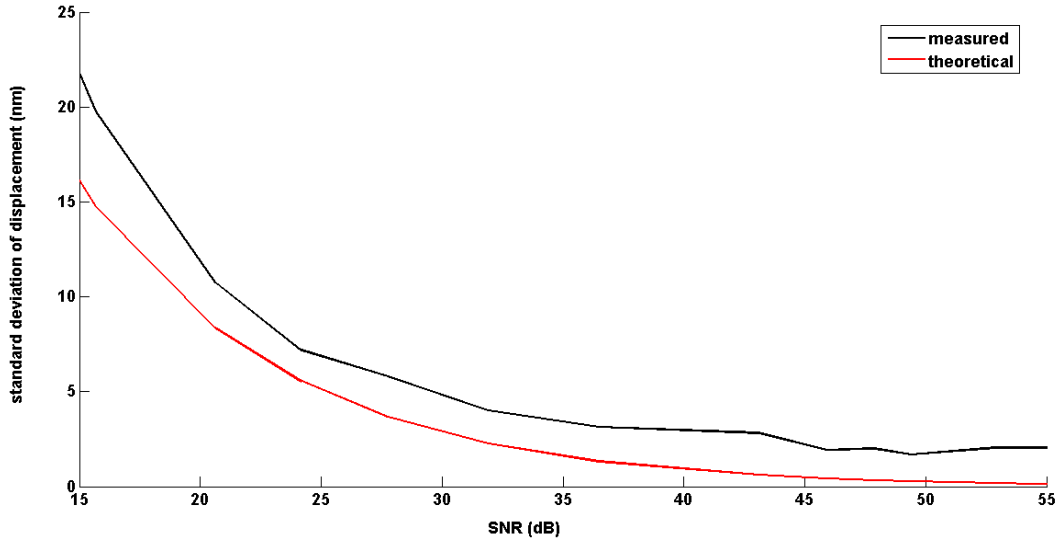

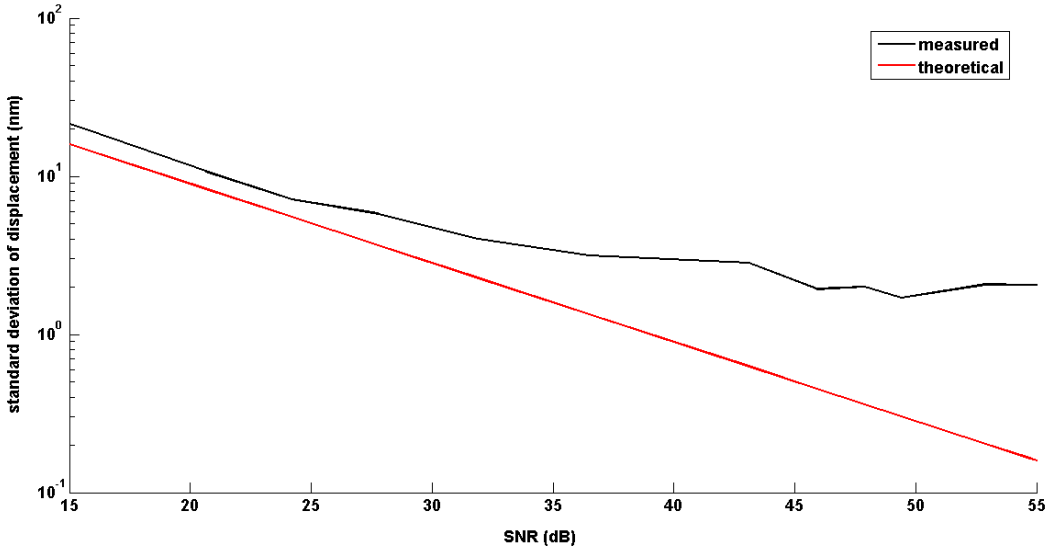

Fig. 3.16 Standard deviation of phase noise vs. signal to noise ratio (SNR). In both linear and log graphs, both measured and theoretically calculated values are plotted.

Phase measurement of piezo-driven subnanometer movement

Second level of phase characterization is to measure subnanometer level displacements by the pr-SD-OCT system. A cover slip was placed on top of the stationary microscope stage and a glass slide was placed above that keeping the two ends of the glass slide on top of the slide insert of a piezo stage that provides high resolution z-axis positioning (ASI, PZM-2000). As a result, when the piezo-controlled plate moved upward or downward, the glass slide also moved with the stage but the cover slip remained stationary. That movement in z-direction changed the vertical distance between the bottom surface of the glass slide and the top surface of cover slip. The piezo stage can be externally triggered to move in the z-direction with a resolution of 1.5nm. In Figure 3.17, the stage was moved by 10nm at every trigger pulse. Same was followed for two other

cases where the movements are 20nm and 75nm, respectively. The response to these subnanometer movements was calculated from the OCT phase measurements and it shows in Figure 3.17, Figure 3.18 and Figure 3.19 that this system is capable of measuring very small relative changes in path length within a reasonable noise margin.

Step of 10nm:

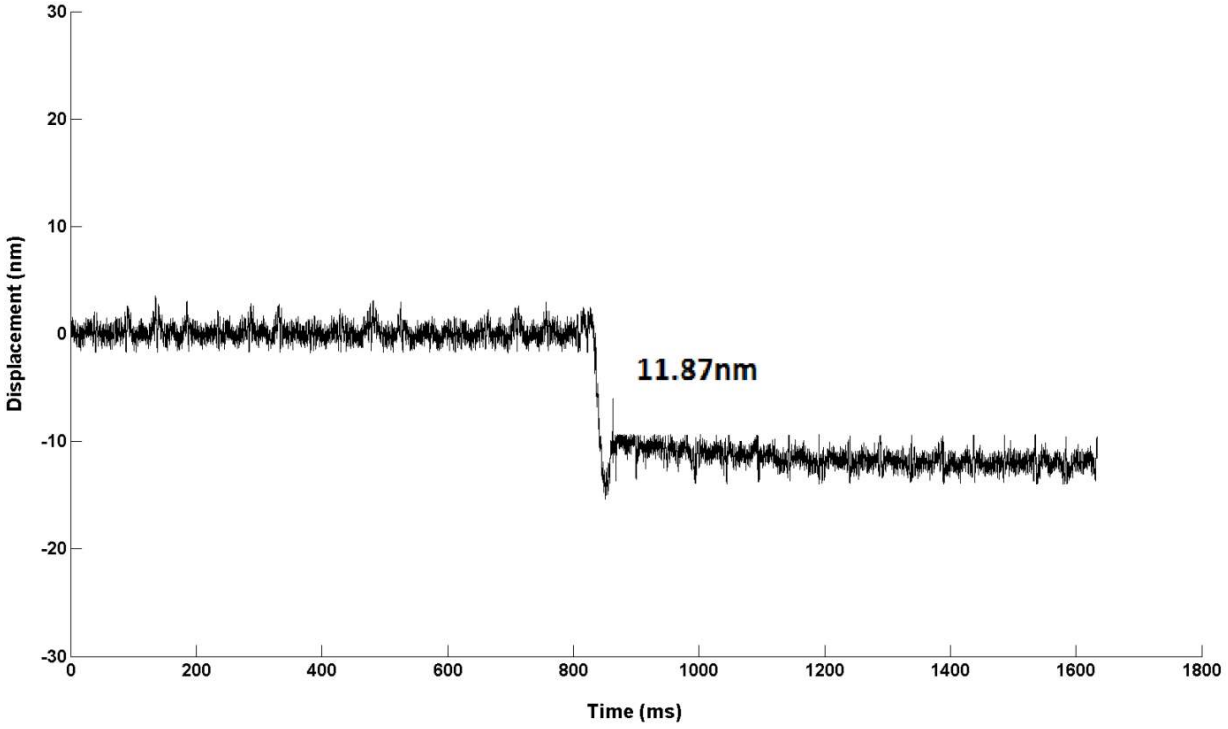

Fig. 3.17 pr-OCT measurement of a 10nm displacement by piezo stage.

Step of 20nm:

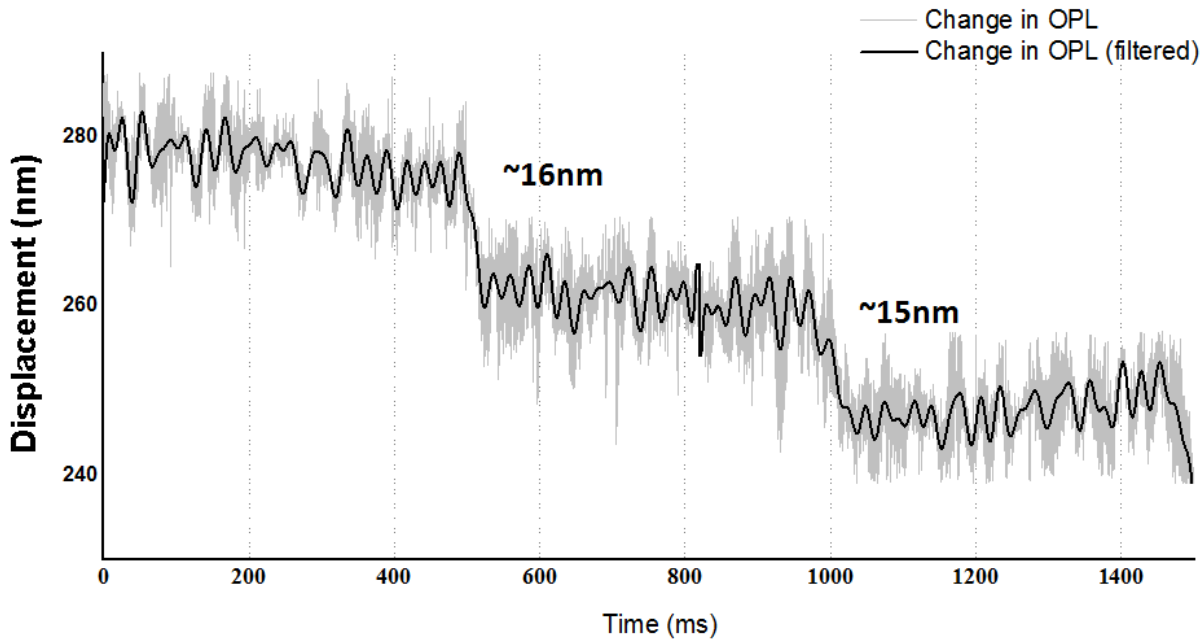

Fig. 3.18 pr-OCT measurement of a 20nm displacement by piezo stage (both raw and filtered values of displacement measurement).

Step of 75nm:

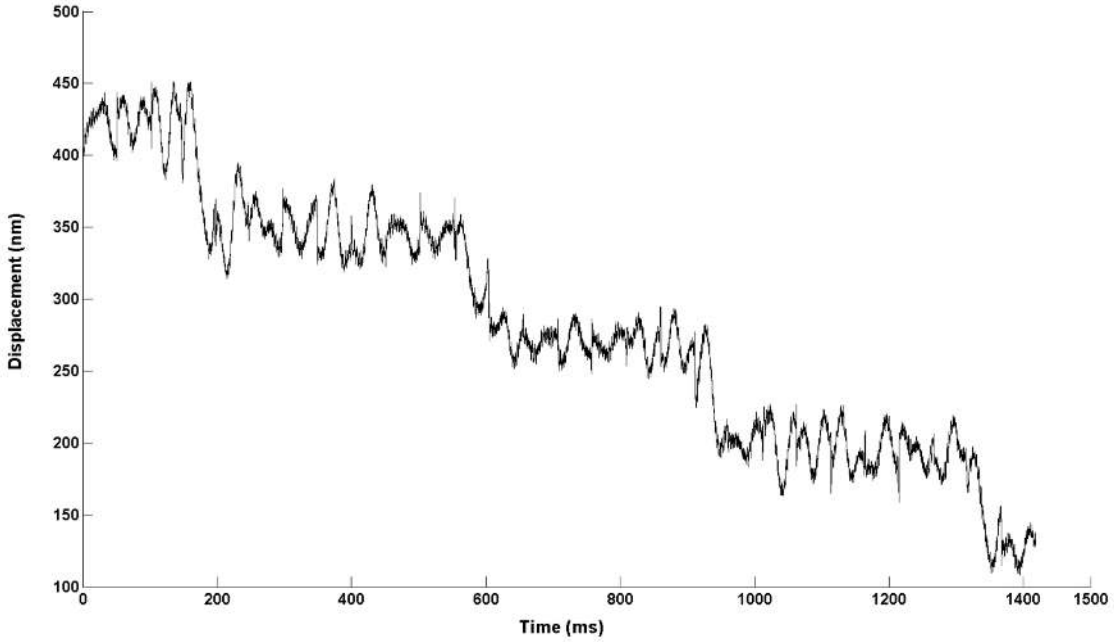

Fig. 3.19 pr-OCT measurement of a 75nm displacement by piezo stage.

4. Imaging of Biological and Non-Biological Samples

Although, primarily this project was focused on Horseshoe crab, the built OCT system has been used for imaging in different other experiments as well. As a result, there have been a number of biological and non-biological samples that have been imaged using this system.

a. Limulus optic nerve

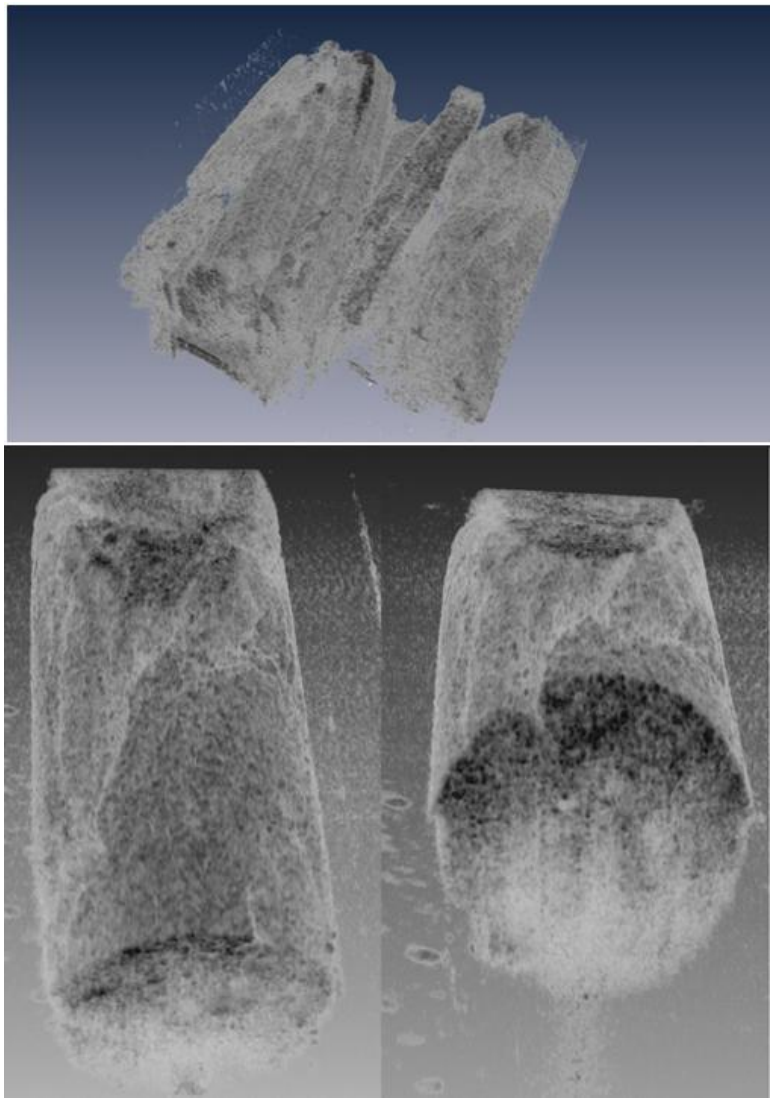

Fig. 3.20 3D reconstruction from OCT cross-sectional images of Limulus optic nerve.

b. Fruit fly brain

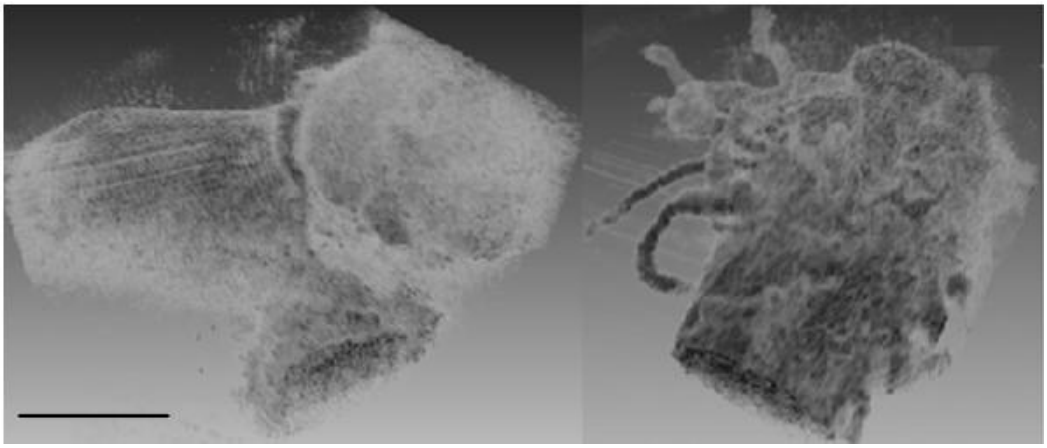

Fig. 3.21 3D reconstruction from OCT cross-sectional images of fruit fly brain stem. Scale bar 500µm.

c. Mouse brain slice

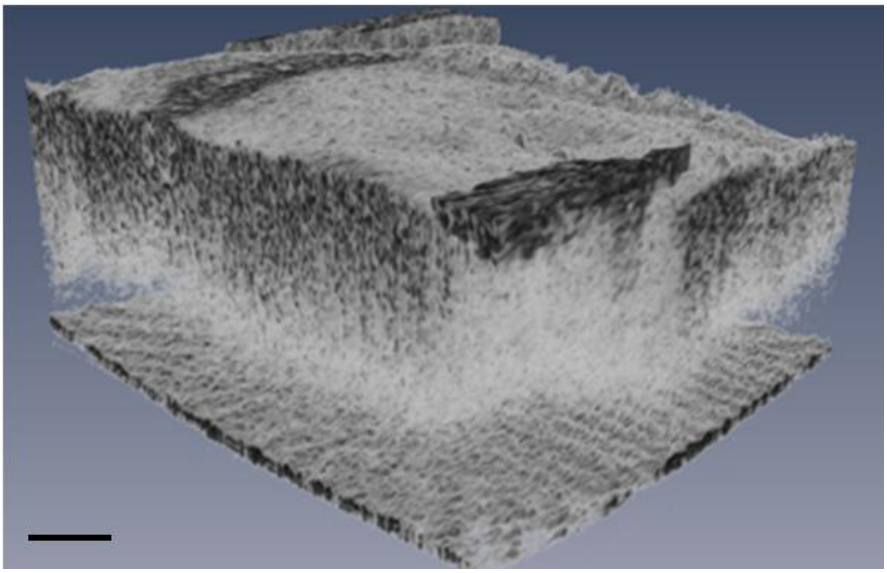

Fig. 3.22 3D reconstruction from OCT cross-sectional images of mouse brain slice on top of MEA. Scale bar 100µm.

d. Ti and Mg Implants

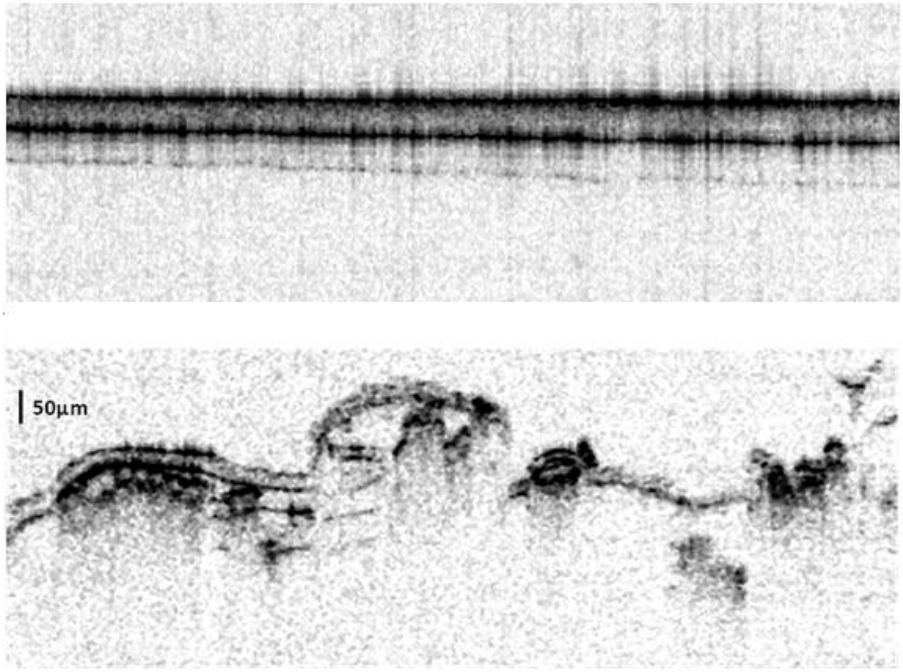

Fig. 3.23 OCT cross-sectional images of 24-hours degraded titanium (top) and magnesium (bottom) implants with PLGA+HA coating on top of metal layer.

e. Tissue scaffolds

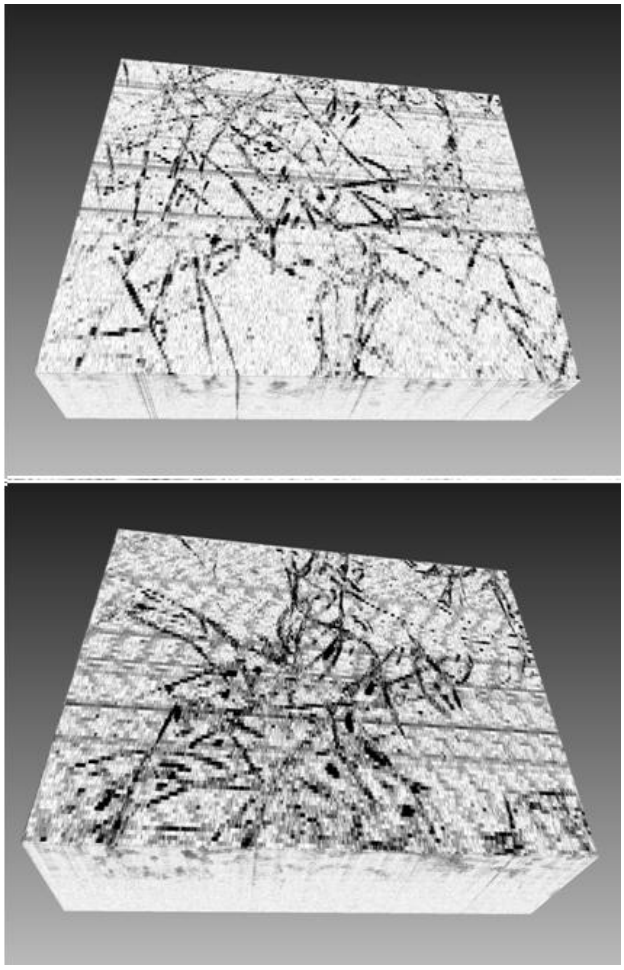

Fig. 3.24 3D reconstruction from OCT cross-sectional images of tissue scaffolds with no cell (top) and with cell (bottom) inside scaffolds.

Chapter 4

Optical detection of neural activity

1. Animal model and sample preparation

Animal Model Selection

Horseshoe crab (*Limulus polyphemus*) is one of the primitive species on this earth, evolved roughly 350 million years ago. Although they belong to the class Arthropod, their anatomy resembles more that of spiders. Lateral eyes of horseshoe crab are used in vision research and their blood is also vastly used in pharmacological research [99-101]. A lateral compound eye of Horseshoe crab with its associated optic nerve is used as the animal model for this experiment. Lateral eyes of horseshoe crab have been studied for years and a great deal is known about the physiology of its visual system. It has two lateral compound eyes and each one consists of about one thousand small light receptors known as ommatidia. Each ommatidium is almost hundred times the size of rods and cones in the human eye and is the largest known retinal receptors in the animal kingdom [99]. Each ommatidium is connected to an eccentric nerve cell and when stimulated by light, this ommatidium sends electrical signal to brain through the cell axon. All the nerve cell axons together form the optic nerve [99, 100].

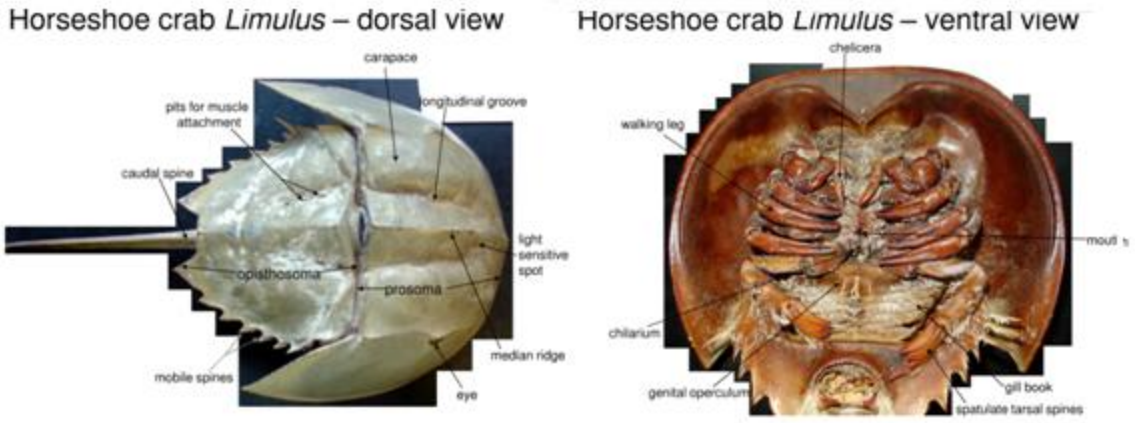

Fig. 4.1 Dorsal and ventral view of *Limulus polyphemus* (Horseshoe crab) [107]

Nerve Sample Preparation

Medium size male *Limulus* (Horseshoe crab) 6”-8” in diameter (Marine Biological Laboratory, Woods Hole, MA) with clear (non-injured) lateral eyes are chosen for dissection. Before the dissection, the *Limulus* is kept in an ice bucket for 20-25 minutes. The cold-anaesthetized *Limulus* is then fixated onto a wooden platform for dissection. After careful dissection, one lateral eye with associated optic nerve is extracted (Figure 4.2) and placed in a Petri dish with Ringer’s solution (430mM NaCl, 9.56mM KCl, 9.52mM $CaCl_2.2H_2O$, 9.97mM $MgCl2.6H_2O$, 50µM HEPES and pH maintained as 7.4). After further cleaning of the sample under the stereomicroscope, the sample is placed on the imaging chamber of the sample arm microscope for structural imaging and neural recording (Figure 4.3). A suction electrode (A-M Systems) with a silver wire is used for electrical recording. The output of suction electrode is filtered and amplified with a gain of 10,000 by a differential amplifier (Warner Instruments, DP-301) and then sent both to the acquisition computer (for recording) and to an oscilloscope (for display).

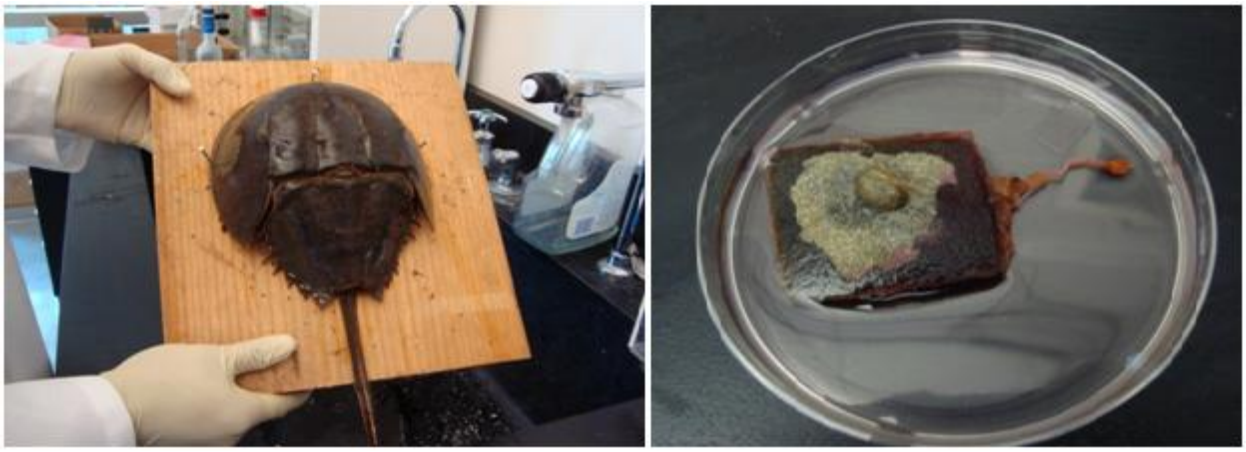

Fig. 4.2 A horseshoe crab just before dissection (left) and a dissected lateral eye with associated optic nerve on a Petri dish (right).

2. Functional Stimulation and Recording Setup

A schematic of the experimental setup is shown in Figure 4.3. The pH and temperature of the solution medium is adjusted so that it approximately mimics *in vivo* extracellular solution. The end of the optic nerve is guided towards the tip of suction electrode and is kept in close proximity to the tip before applying suction in the electrode. Generally, a threaded syringe is used for creating suction pressure. The electrical output of the suction electrode is connected to a differential amplifier and a band pass filter for signal conditioning. The processed signal is then sent to the computer for data acquisition and simultaneous display on an oscilloscope screen.

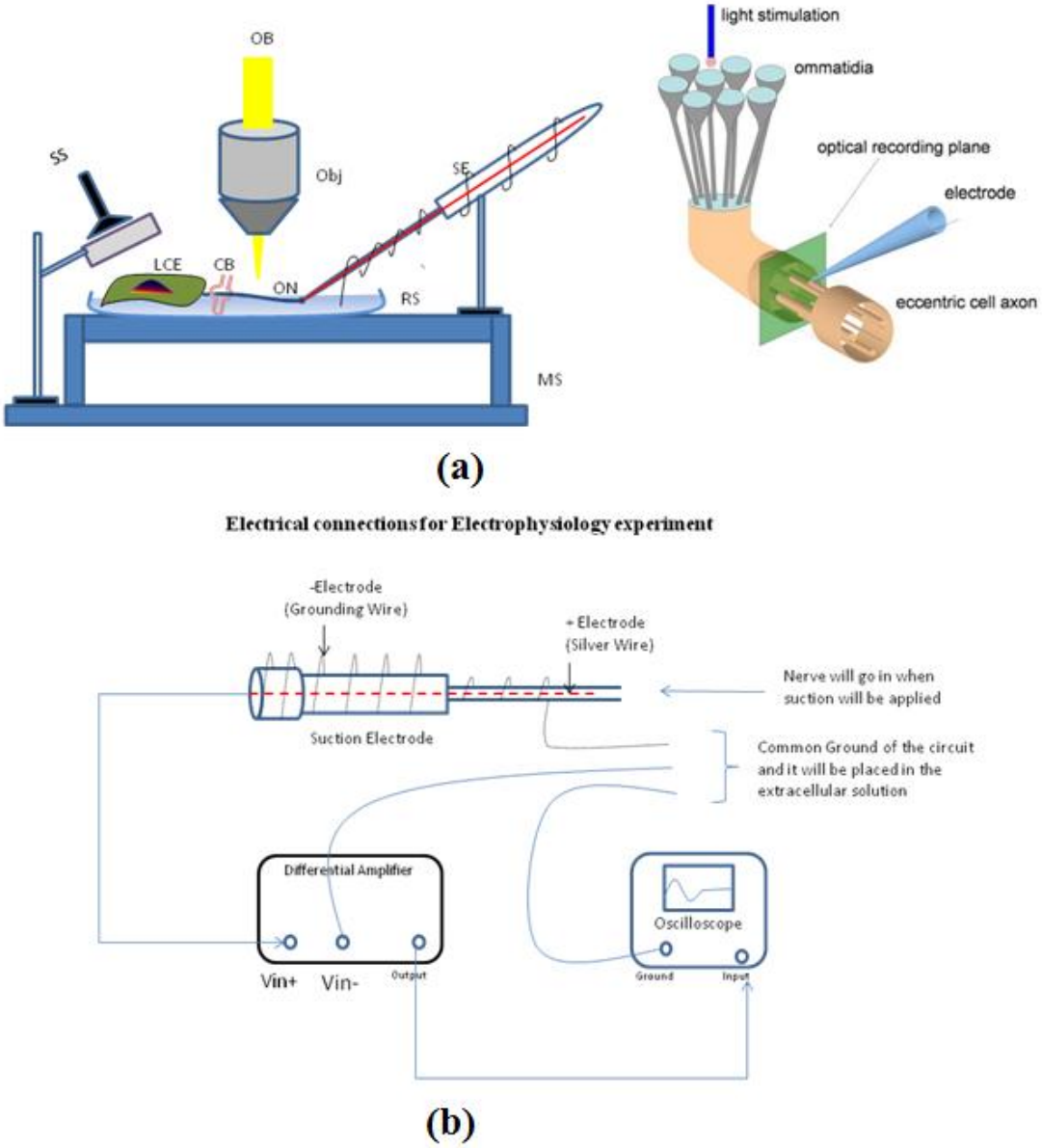

Fig. 4.3: (a) A schematic of experimental setup for simultaneous optical and electrical recording of action potentials. (b) Schematic of electrical connections for Electrophysiology.

Once the setup is ready, suction pressure is applied until the nerve reaches inside of the electrode and comes in contact with the electrode wire. Then the nerve is stimulated by

shining light on a particular number of ommatidia of the lateral eye and subsequent activity is observed in oscilloscope and also recorded in computer. When the nerve is stimulated, simultaneous recording by OCT system and suction electrode are acquired and monitored over time. Thickness change information are obtained from phase of top and bottom surfaces of the layer. In this measurement, the motivation behind choosing the bottom surface of the nerve as reference is that any other external reference may be subject to motion artifact and thus contribute to phase noise. In turn, this may cause wrong indication of action potential propagation induced thickness change. In comparison, in case of using bottom layer as reference, for any undesired movement of nerve, both the bottom and top surfaces are very likely to undergo similar amount of displacement and thus the difference between their phases remains the same. Therefore, common mode noises can minimally affect the action potential detection measurements.

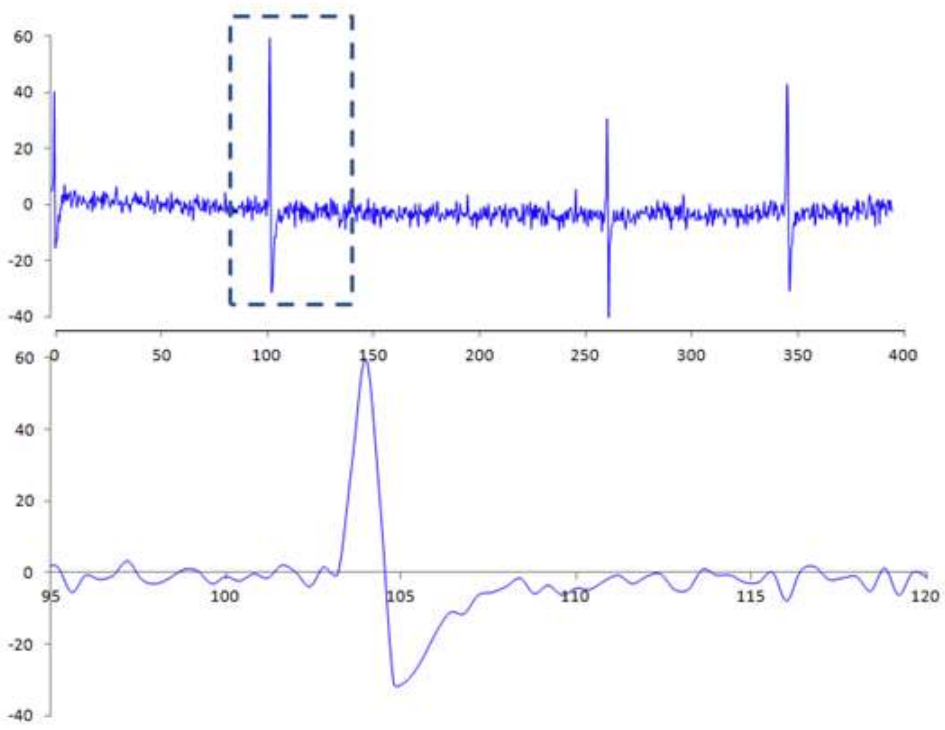

Fig. 4.4 Electrical recording data from a very small bundle of axons of Limulus optic nerve. Electrically recorded single action potentials and one single action potential (in dotted rectangular box in figure a) in more details in bottom figure. The time duration of single action potential was about 3ms.

Timing Diagram

In order to maintain synchronization between optical and electrical recording, control pulses are operated from a single computer. TTL (transistor-transistor logic) signal pulses are sent to the data acquisition cameras, to electrophysiology recording and sawtooth waveform to the scanning galvos. Top timing diagram below, in Figure 4.5a, shows the TTL signals during scanning the beam across the nerve to find a suitable position in the axon for phase measurement. No trigger to the electrical measurement is sent during this time. Once an area in the nerve is chosen for recording, there are no more pulses sent to

the X-galvo scanner, as shown in Figure 4.5b. Synchronized pulses will be sent to the camera trigger and electrical measurement trigger and thus optical and electrical recording will be performed simultaneously.

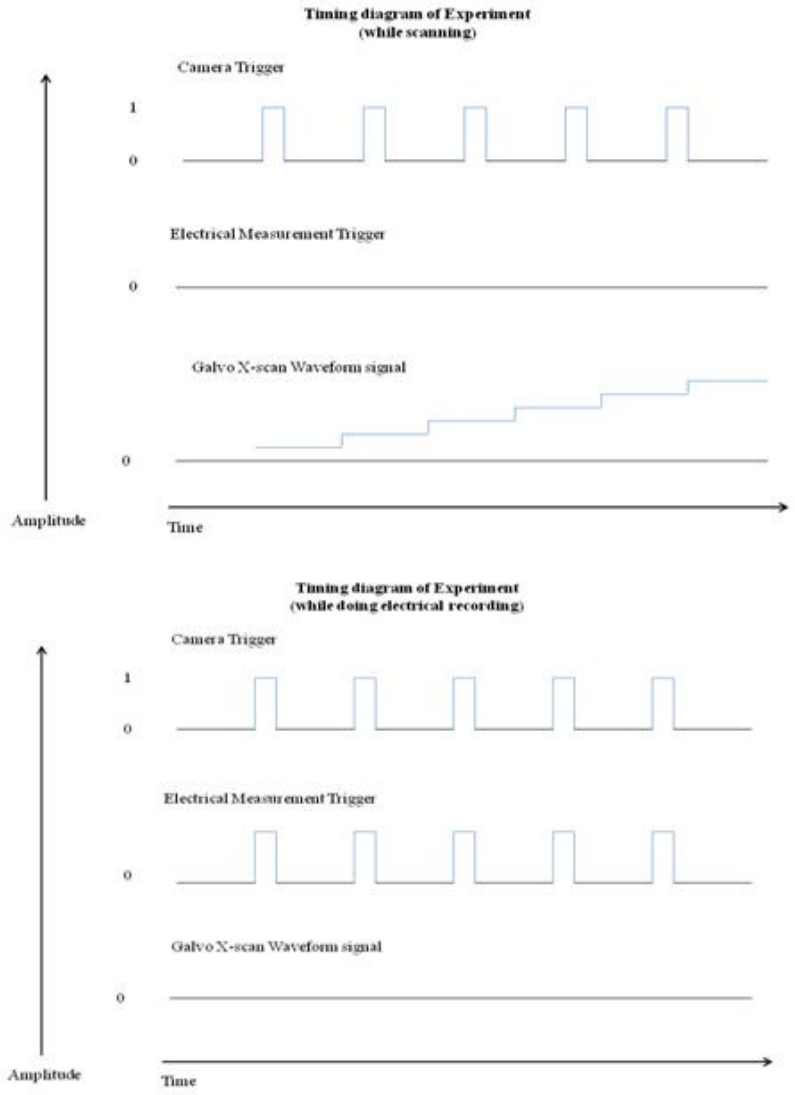

Fig. 4.5 Timing diagram while scanning for imaging only, no recording (top). Timing diagram for simultaneous optical (M-scanning) and electrical recording (bottom)

Phase Noise Characterization

Characterization of phase noise is very important to ensure reliable phase measurements. Phase noise is usually characterized by measuring phases from a cover slip or a glass slide. Phase difference between top and bottom surfaces of a cover slip is measured and the standard deviation of this phase difference is calculated. This standard deviation sets the limit for minimum detectable phase difference. Fortunately, this standard deviation is inversely proportional to the square root of signal-to-noise ratio (SNR) and thus with the increase in SNR of a system, minimum detectable phase difference decreases, i.e. phase sensitivity increases. In neural activity experiments, minimum detectable phase difference should be smaller than the actual phase difference between top and bottom surfaces of nerve during activity. System SNR is adjusted until the minimum detectable phase difference falls below the expected lower limit of phase difference. Phase noise is characterized for both the cameras and then corresponding acceptable SNR range is calculated.

A cover slip was used as a sample for measuring the phase stability of the system. The phase difference between lights backscattered from the top and bottom layer of a cover slip was monitored over time. Since the thickness of cover slip remained invariant, this phase difference should remain constant over time. Phase noise margin (i.e. lower limit of detectable phase change) was measured from the standard deviation of phase differences over time. Experimentally measured phase noise was about 500 picometers at an SNR of 45dB (Figure 4.6a). For this SNR, the theoretical limit of phase noise margin is ~$1/\sqrt{SNR}$

= 360 picometers. We assume that the remaining part of the phase noise was coming from environmental factors, such as vibration of the cover slip, slight variation of room temperature, etc. During the 30 seconds of phase measurement (only 2s is shown in Figure 4.6a), the phase remained stable for the entire time period and this demonstrates sufficient phase stability.

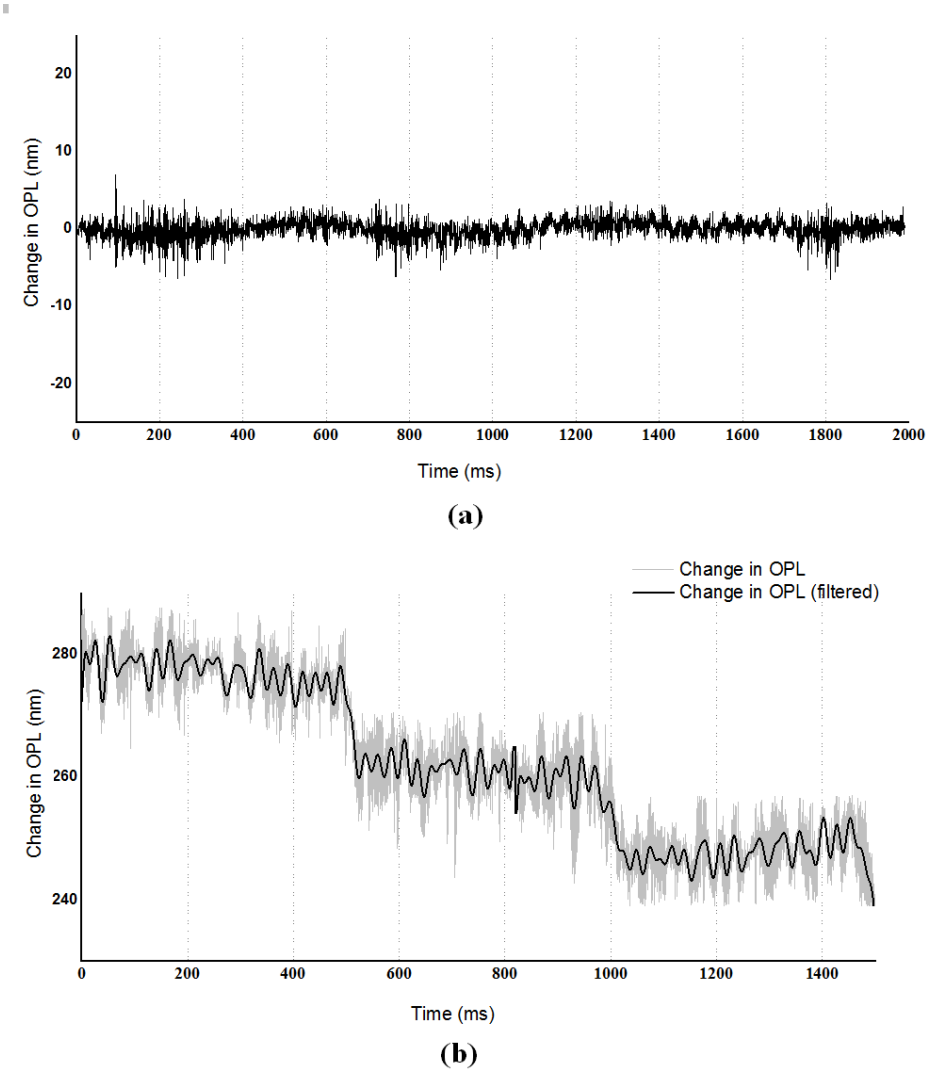

Fig. 4.6 Phase difference between two layers of cover slip measured over time. The standard deviation of this plot represents the phase noise margin or lower limit of detectable phase change (a). Pr-OCT detection of piezo-controlled 20nm stepwise displacements of a glass slide (b).

Another set of measurements was taken to verify the phase-sensitivity of the system in detecting subnanometer displacements or thickness changes. A cover slip was placed on top of the stationary microscope stage and a glass slide was placed above that keeping the two ends of the glass slide on top of the slide insert of a piezo stage that provides high resolution z-axis positioning (ASI, PZM-2000). As a result, when the piezo-controlled plate moved upward or downward, the glass slide also moved with the stage but the cover slip remained stationary. That movement in z-direction changed the vertical distance between the bottom surface of the glass slide and the top surface of cover slip. The piezo stage can be externally triggered to move in the z-direction with a resolution of 1.5nm. In Figure 4.6b, the stage was moved by 20nm at every trigger pulse in 500ms. The response to that movement was calculated from the OCT phase measurements and it shows in Figure 4.6b that this system is capable of measuring relative changes in path length of this magnitude within a reasonable noise margin.

Motion Artifacts and Other Noises

Nerve activity is usually characterized by propagation of action potentials and time period of an action potential is around 1~3ms. This signal contains frequency component in the range of 1/time period = ~333Hz - 1 kHz. On the other hand, displacement of nerve due to any vibration or undesired movement is usually slower process and in most cases, displacement frequency is of order of 1~10Hz. Due to this significant difference in speed of the two activities, they can be easily distinguished and identified in post experiment analysis.

3. Structural Imaging of Limulus Nerve

The end terminal of nerve sample is inserted into the suction electrode and OCT images are taken along the length of the nerve (Fig. 4.7a). OCT cross-sectional images of *Limulus* optic nerve sample were obtained at the beginning of each experiment. Figure 4.7 and 4.8 show representative OCT image of *Limulus* optic nerve cross-section and the rendered volume from 250 cross-sections taken along 4mm nerve length. Figure 4.8b shows a similar cross-section and reconstructed volume of another optic nerve sample. In this case, the volume is virtually sliced down to see the inside of nerve bundle and small axon bundles are clearly visible. In this way, it is possible to virtually dissect an optic nerve at any location and visualize the microstructures. Figure 4.8 shows few more examples of optic nerve volumetric images which are displayed from different angles to visualize the smaller nerve bundles and associated microstructures.

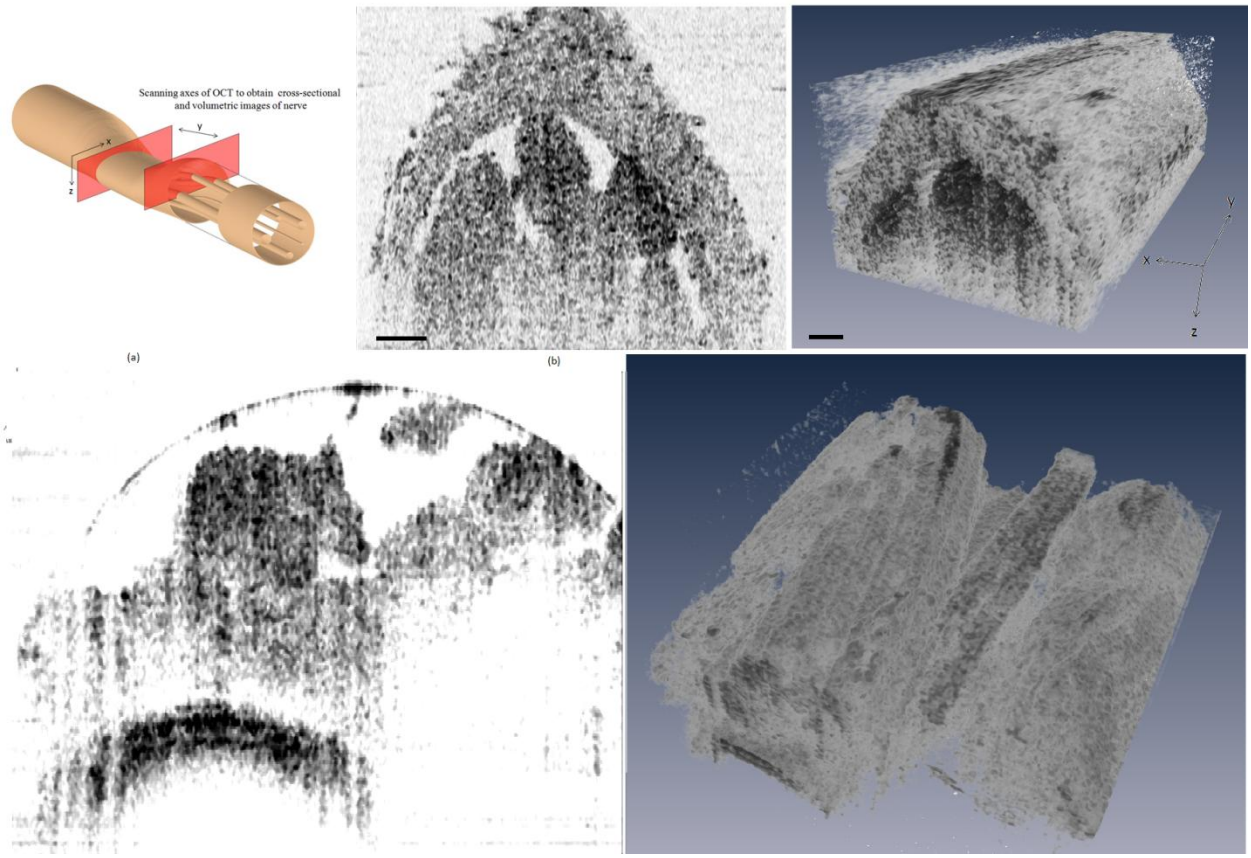

Fig. 4.7 Structural imaging of *Limulus* optic nerve using OCT. (a) Schematic showing the optic nerve bundles and scanning axes of OCT to obtain cross-sectional and volumetric images. XZ is the cross-sectional image plane and y-axis represents the third axis of scanning to obtain the 3D volume. (b) A representative cross-sectional image of the nerve sample. It shows three adjacent large axon bundles. (c) Volumetric reconstruction of a 1mm section of the nerve. Scale bar: 50µm in (b), 100µm in (c).

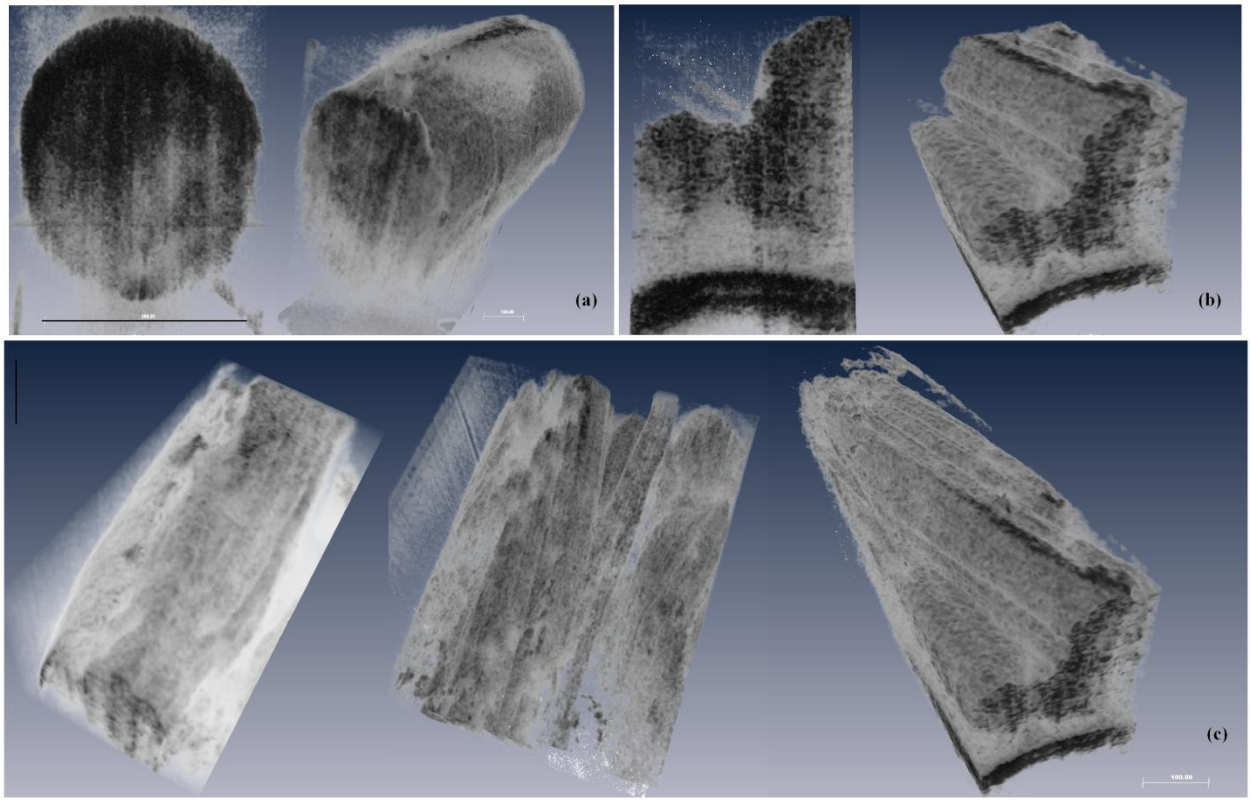

Fig. 4.8 Structural imaging of *Limulus* optic nerve using OCT. (a) Representative cross-sectional image of a nerve sample and its reconstructed volumetric image obtained from rendering such cross-sections. (b) Cross-section and volumetric image of another sample, here the smaller nerve bundles and their axons are more easily visible. The dark section under the nerve is the thin silver wire of the suction electrode (c) Examples of rendered volumes from different optic nerve samples and the internal microstructures of the optic nerve bundles are visible from different angles. Scale bar: 500µm (top section), 1mm (bottom section).

4. Point-scan of Limulus Nerve and Analysis Scheme

A cross-sectional image where bundles and the boundaries are clearly visible is chosen for taking time-lapse images. After acquiring data of same cross-section over time, it becomes easier to differentiate between speckles and real microstructures of nerve. Thereafter, from the chosen cross-section, an A-line (depth profile) is selected for M-scan

(line scan over time). A-line with maximum number of axon bundles with sufficient SNR is chosen so that maximum number of bundles is scanned over time in M-scanning. Once the A-line is chosen, to ensure consistency, all the remaining phase measurements are done on the same A-line of the nerve. The chosen A-line is scanned and recorded over time (M-scan). Stimulation on eye is timed within this time frame and nerve activity is simultaneously recorded using a suction electrode. In OCT, the camera records the spectrum and after FFT of that spectrum, we obtain the depth profile. Since the same lateral position is scanned over time, the spectrum and hence the depth profile remain identical over time. However, for measurement of very small scale changes, further analysis is required. By resolving the phases of every depth points in the depth profile, we get additional information to detect any subnanometer displacements or changes in thickness in nerve bundles.

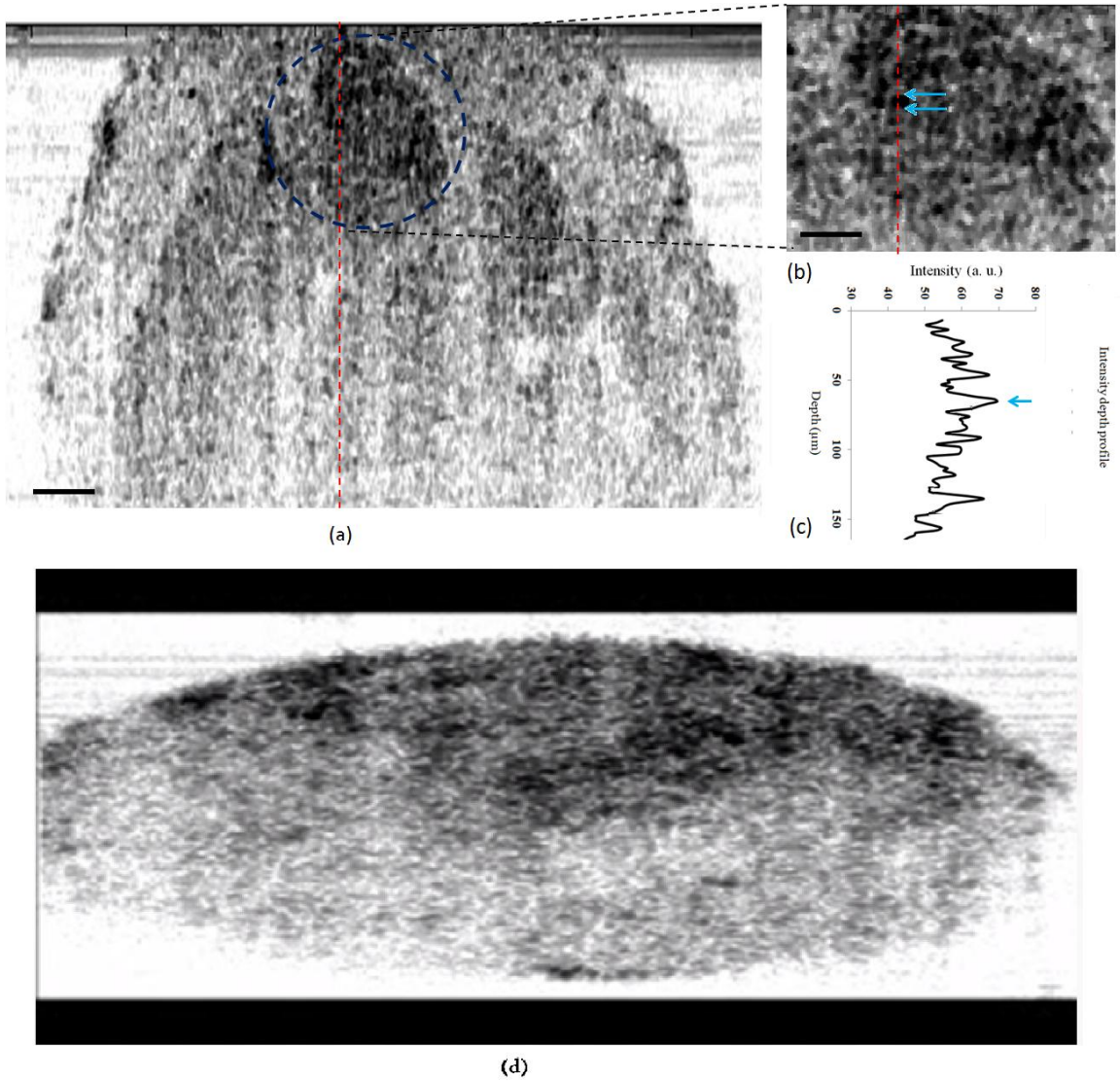

Fig. 4.9 Steps before M-scanning for phase measurement in *Limulus* optic nerve (a) Cross-sectional imaging to find the nerve bundles (b) Enlarged view of the bundles (c) Depth profile along the chosen bundles (d) Imaging same cross-section over time to differentiate between nerve bundle and speckle.

As mentioned earlier, a depth profile with maximum possible number of visible bundles is chosen for continuous scanning. Usually the nerve bundle is dissected small enough (size) so that only a small fraction of the entire nerve enters the small tip (size) of suction

electrode and we also limit our optical scanning within that small region. As a result, number of bundles is limited usually within the range of 5-20 bundles. For the analysis, both single bundle and multiple bundle analysis are done.

Single bundle analysis

A single bundle is usually in the range of 5-6 pixels (~9-11μm) in thickness in OCT image. The intensity profile shows marked points at different depths of the bundle. Points are marked as A, B, C, D and E. C is the peak intensity which corresponds to the center of the bundle and A, B are one side of the center and D, E are on the other side (Figure 4.10). Phase values of these points are extracted from detected spectrum and phase differences are calculated for different pairs, e.g. AB, AC, CE, etc.

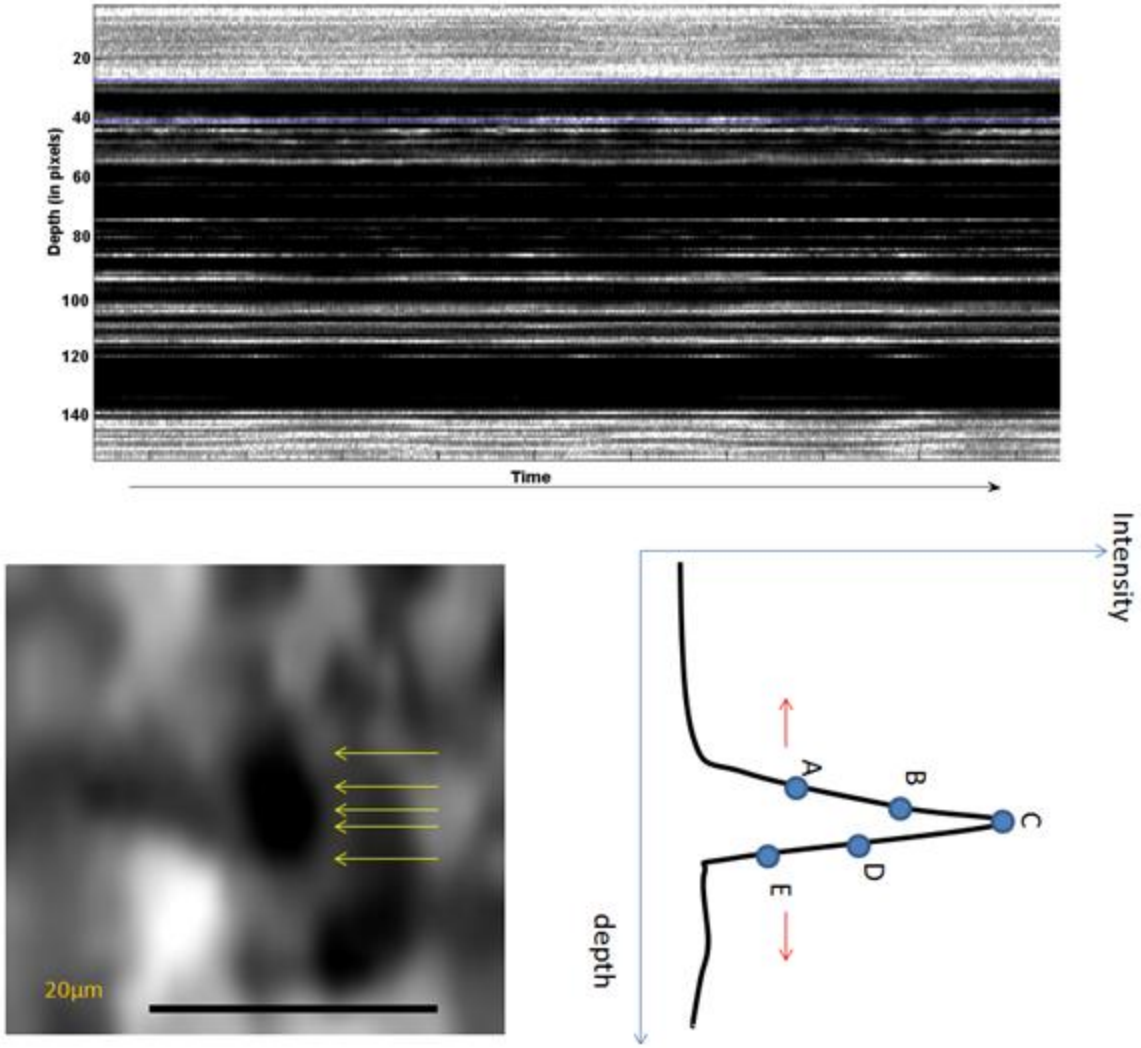

Fig. 4.10 Single bundle analysis of phase measurements data

Two bundle analysis

In a similar way, depth points of two bundles are marked and their phases are extracted. Phase differences between the points are calculated and plotted as a function of time. Phase difference between the peaks of these two bundles provides the relative changes in

position or thickness. Using multiple bundle analysis, one can have a larger number of points to analyze and this larger ROI with more axon depth points will hopefully help to understand the mechanism of these activity associated structural changes.

5. Single Shot Detection of Individual Impulses

We have been able to detect action potential associated transient structural changes in single shot measurements which has been reported first time from Limulus nerve as far we know. However, rate of single shot detection accuracy is still not up to the mark, so we have also tried averaging multiple responses and the results from each analysis are shown in following sections.

Figure 4.11 shows a set of measurements from both the regular reference-arm configuration and common-path configuration of OCT system. Figure 4.11a shows electrical recording and concurrent optical recording (thickness change measurement) obtained from common-path configuration. The recordings shown here are spontaneous neural activities in *Limulus* optic nerve. The plots demonstrate that change in thickness (~20-40μm) of the axon bundle has good temporal correlation with the action potential in electrical recording. Figure 4.11b shows similar set of recordings from reference-arm configuration. The magnitude of thickness change observed here is also in 20-40μm range. Here again, the action potentials recorded in electrical method have good temporal correlation with thickness change measurement. The analysis of large sets of data has shown that common-path configuration was capable of detecting activity in more

experimental trials in comparison to regular reference-arm configuration. The difference is presumably due to the common mode noise rejection in common-path setup and hence improved phase-sensitivity. Therefore, common-path configuration was used for phase measurements in rest of the experiments. In both plots of Fig. 4.11, the electrophysiology data was smoothed by a moving average filter (with a span of 5) and the phase data was filtered only for 60Hz noise.

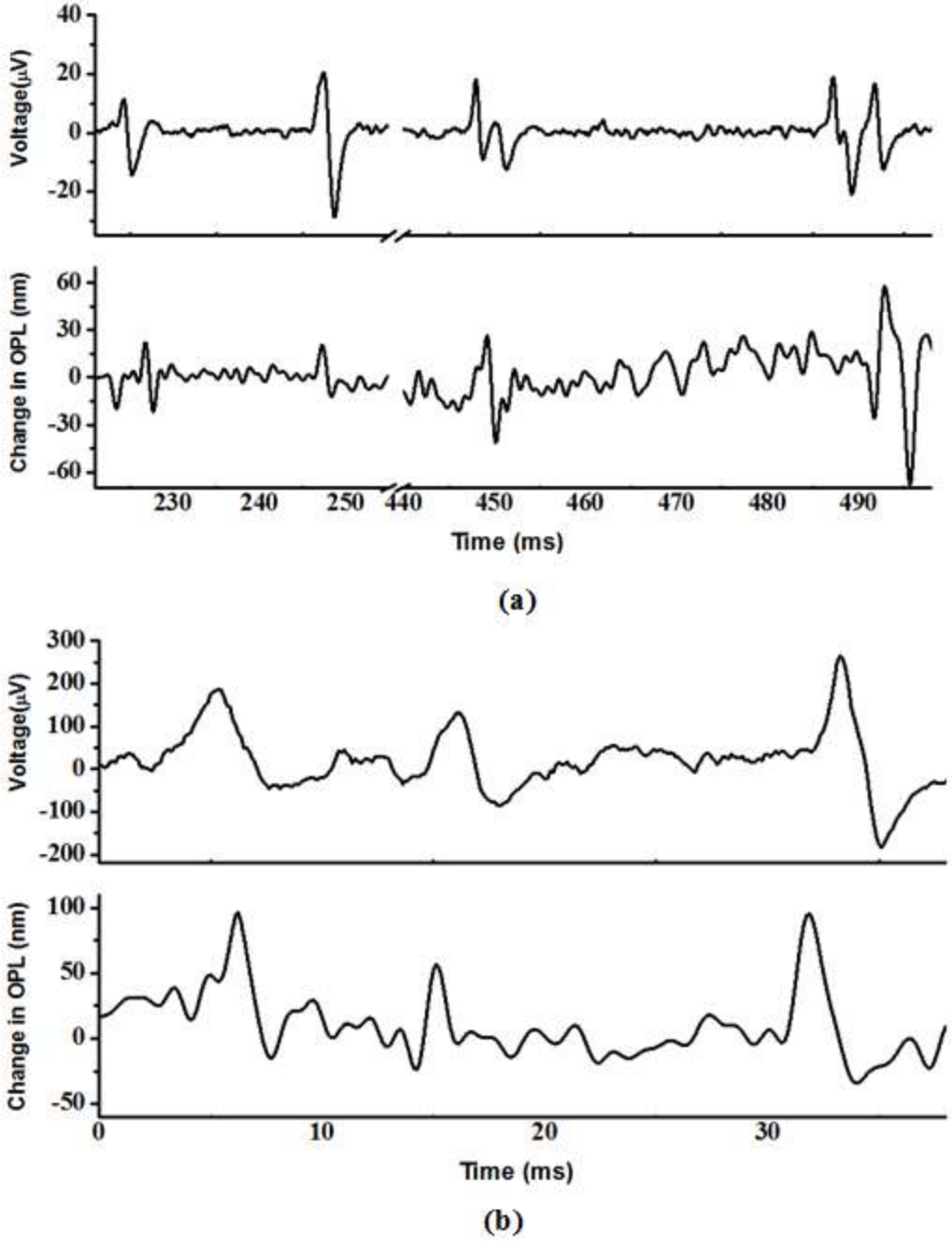

Fig. 4.11 Electrical and optical recordings of neural activity in *Limulus* optic nerve. Optical phase measurement data recorded from both (a) reference-arm configuration and (b) common-path configuration are shown here.

6. Averaging of Multiple Responses

Although single shot detection is the most desired outcome in detecting activity, however, due to limitation of system accuracy in detecting every single trial makes it less useful. As a result, averaging of multiple responses has been also investigated as an alternative to improve detection sensitivity. Figure 4.12 shows an example where multiple responses were averaged. Figure 4.12a is an average of 2 responses, 4.12b is an average of 5 responses, 4.12c is an average of 10 responses, and 4.12d is an average of 20 responses. It has been found that averaging of 8-10 trials provide reliable measurements in detecting activity.

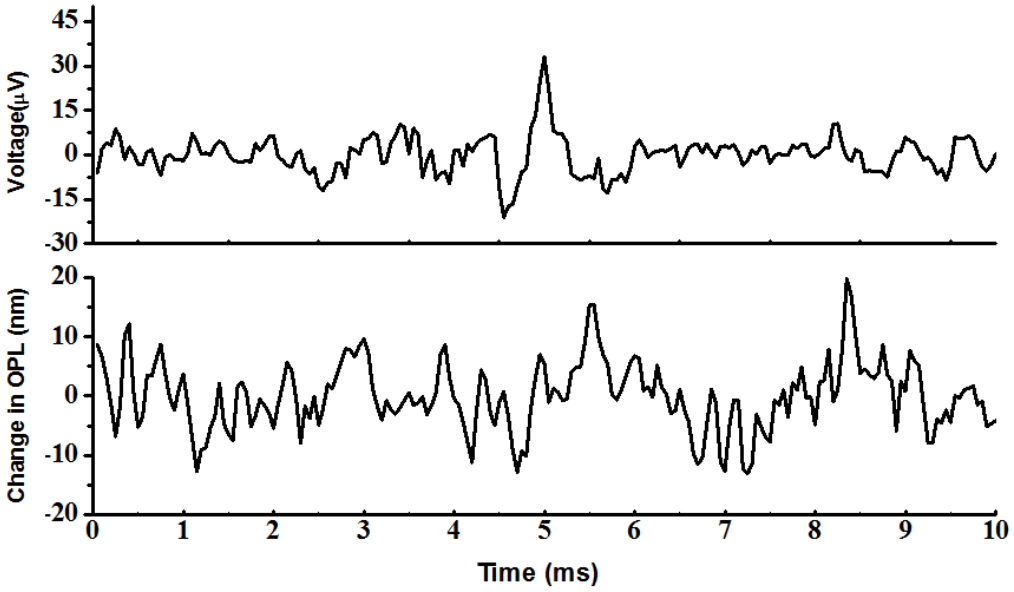

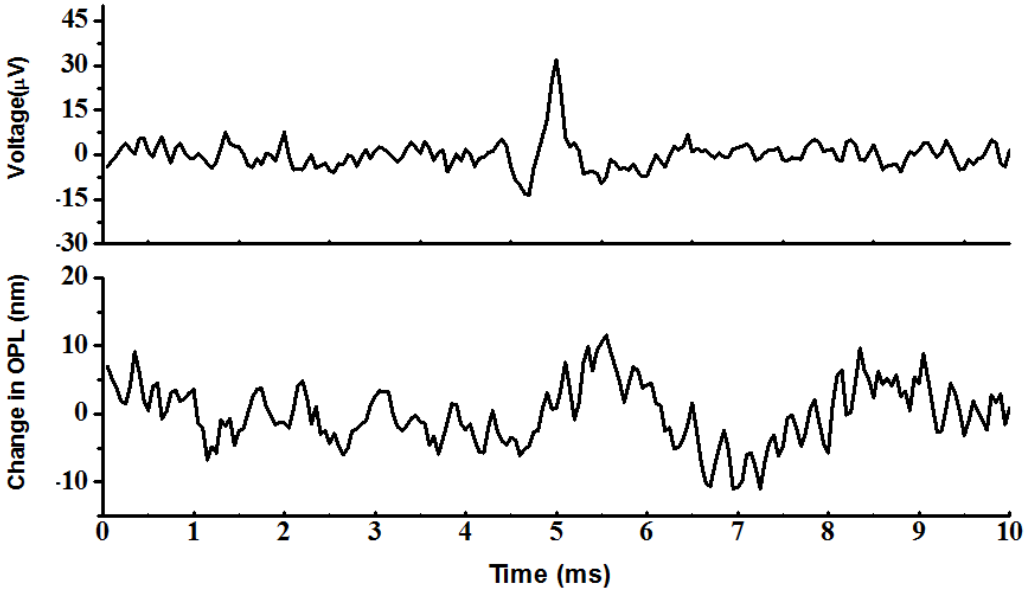
Voltage(μV)
45
30
15
0
-15
-30
Change in OPL (nm)
20
10
0
-10
0
1
2
3
4
5
6
7
8
9
10
Time (ms)

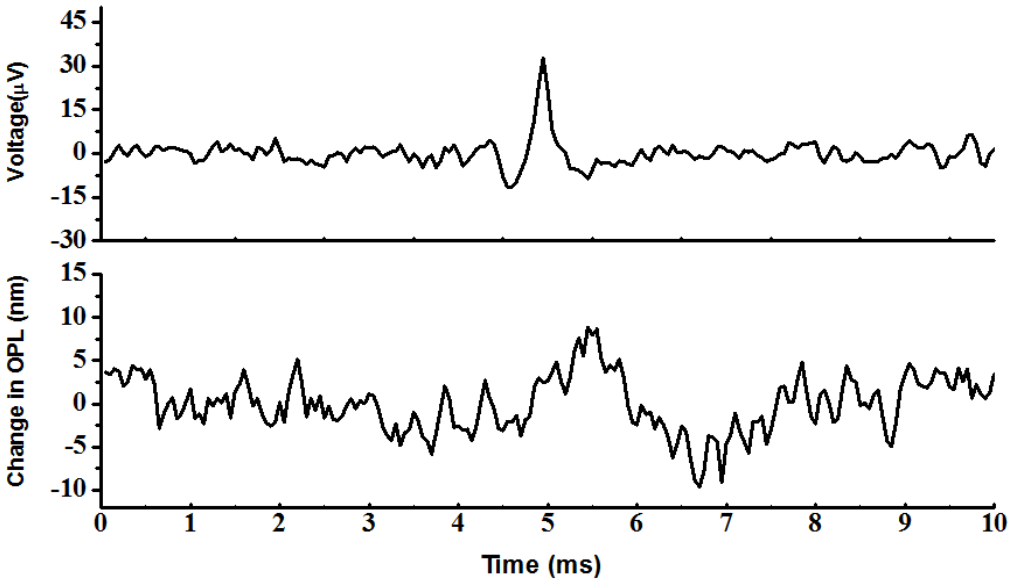
Voltage(μV)
45
30
15
0
-15
-30
Change in OPL (nm)
15
10
5
0
-5
-10
0
1
2
3
4
5
6
7
8
9
10
Time (ms)

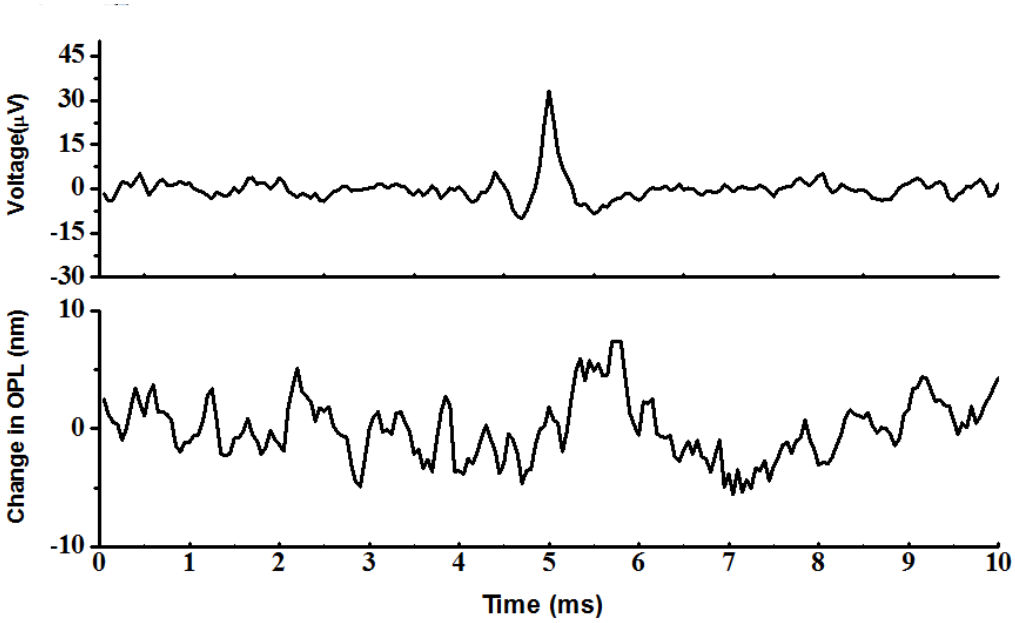

Fig. 4.12 Averaging of multiple responses. (2 responses, 5 responses, 10 responses and 20 responses)

7. Double Camera Detection of Activity

The pr-SD-OCT system already has a spectrometer that has two line scan cameras to collect two orthogonal polarization states of light. Since both cameras acquires at exactly same time, it will be more convincing to measure activity in both cameras simultaneously. One challenge in this is that two cameras have different levels of phase noise and sometimes the detected activity in one camera is not identified in another camera due to relatively higher phase noise in the second camera. Figure 4.13 shows an example where activity induced optical changes were detected in straight camera (H-polarization) and side camera (V-polarization), respectively.

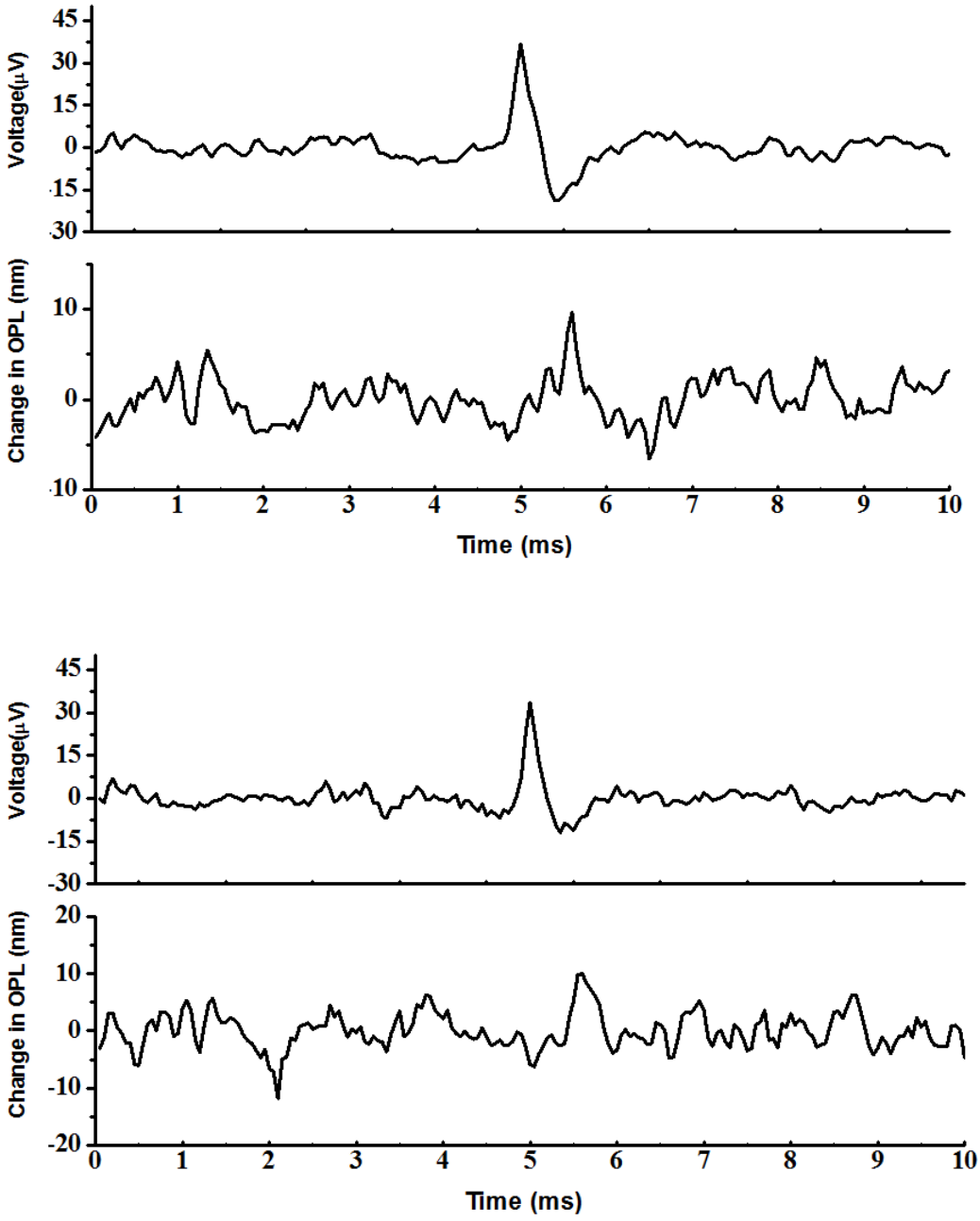

Fig. 4.13 Averaging of 10 responses from straight camera data (top) and average of 17 responses from side camera data (bottom) Note: these two responses are not simultaneous responses.

8. Depth-resolved Detection of Activity

OCT cross-sectional image of Limulus optic nerve forms from a number of A-lines acquired sequentially in lateral direction. Each A-line contains 2048 depth points which corresponds to a physical length of 3.8mm. However, only about 400-500 depth points constitute the nerve bundles and within these depth points, there can be multiple axon bundles at different depths. Therefore, this section was focused to analyze the structural changes of the nerve bundles at different depths and resolve the activity. In this way, it is easier to visualize how the overall trend of structural changes along the depth and how the changes progress over time. Figure 4.14 shows how M-scan data (continuously scanned same A-line) is analyzed. From the depth profile, multiple sets of depth points are analyzed and the based on a reference layer, relative phase differences are plotted for each depth layer. In Figures 4.15 to 4.19, the plots show the rapid change in phase differences (structural change) while there is electrical activity (blue plot). With further investigation, these depth-resolved activity analyses will allow us to detect almost every single activity associated changes in nerve thickness at any of its depth layers.

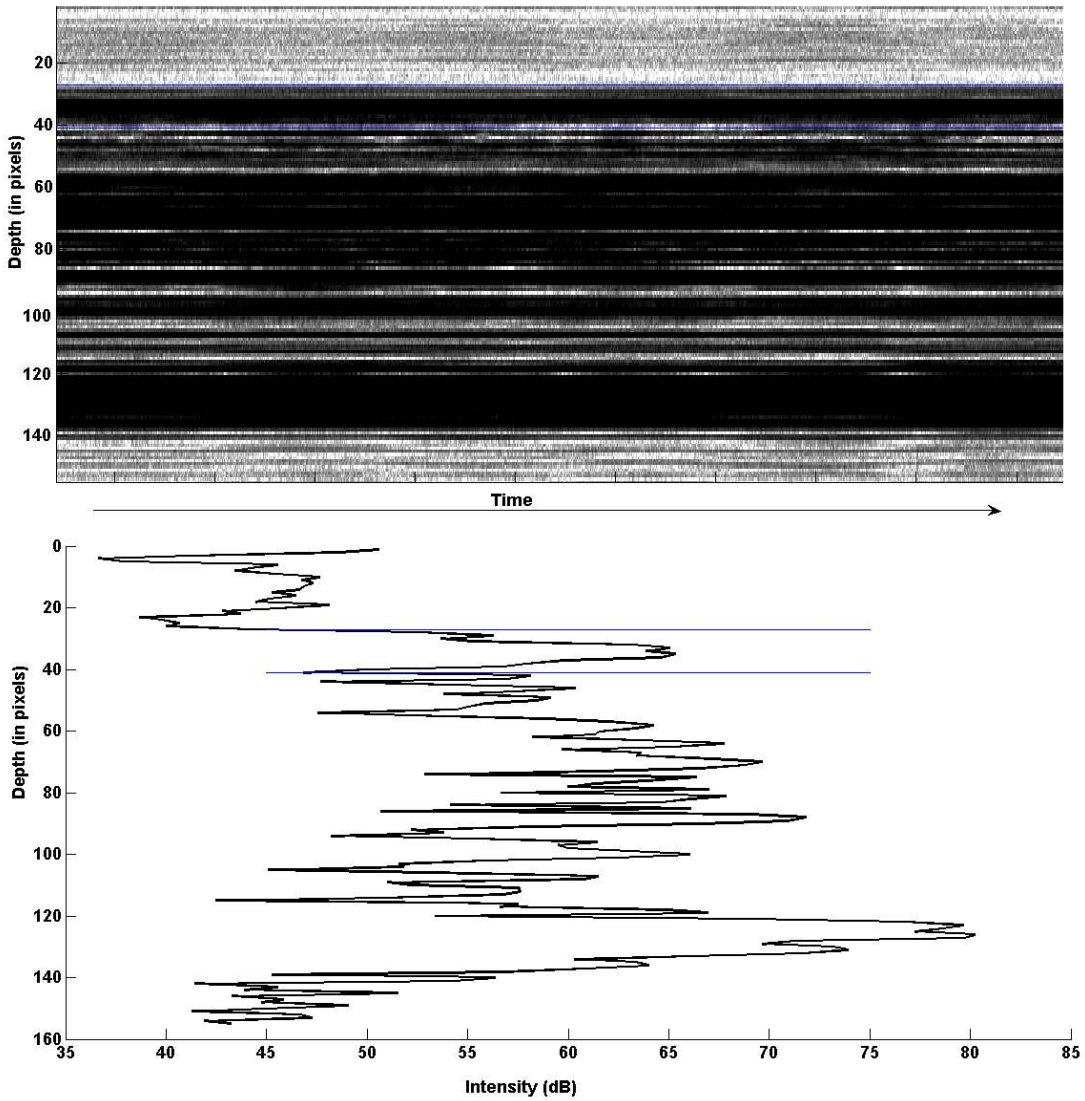

Fig. 4.14 Depth resolved activity (a) M-scan intensity image (b) Depth profile showing group of bundles.

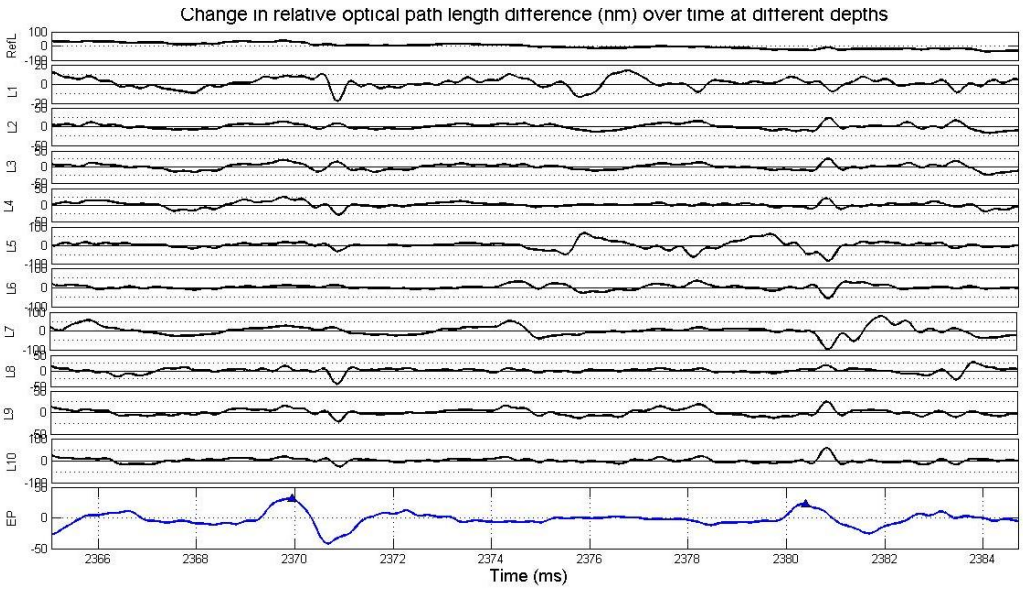

Fig. 4.15. Depth resolved activity (case 1)

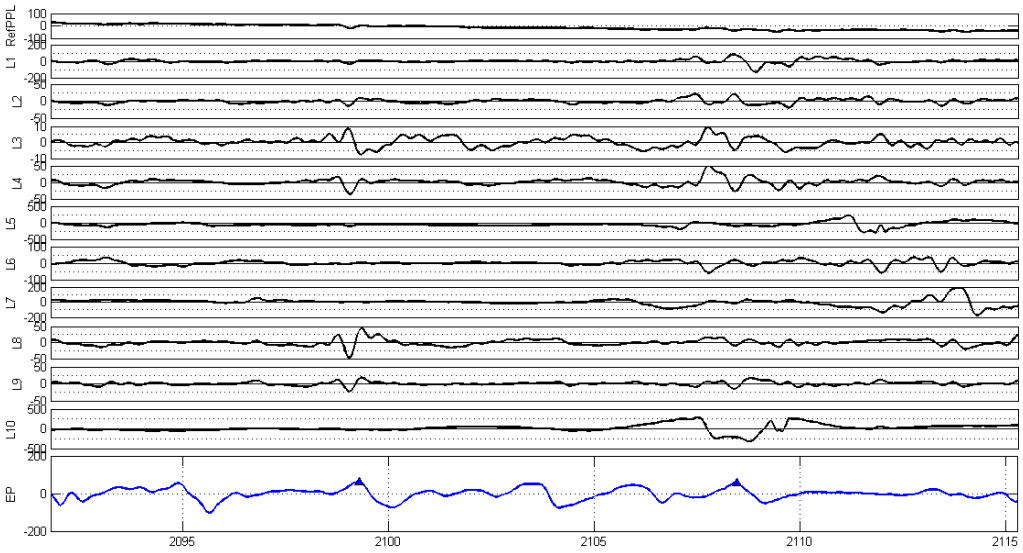

Fig. 4.16 Depth resolved activity (case 2)

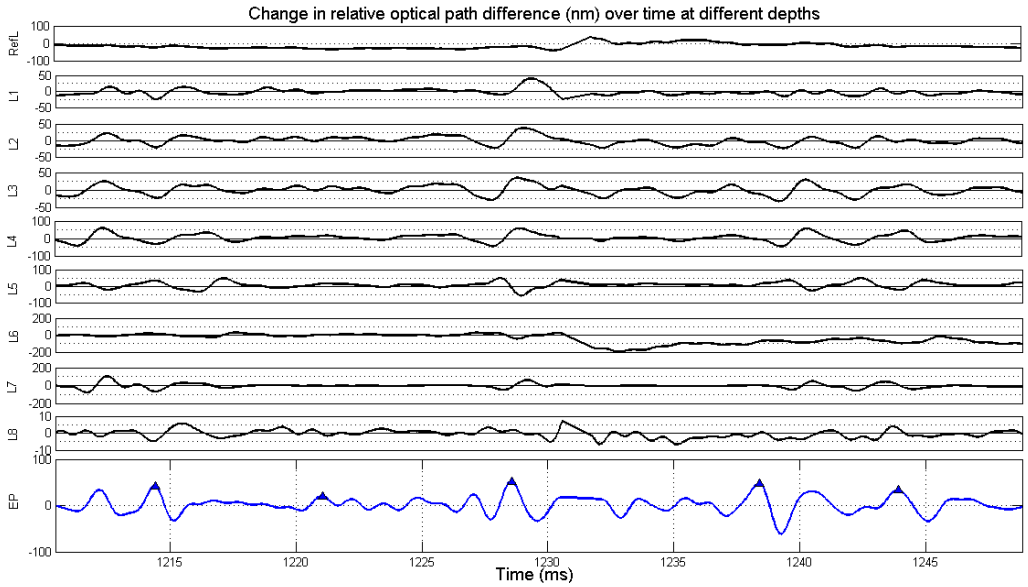

Fig. 4.17 Depth resolved activity (case 3)

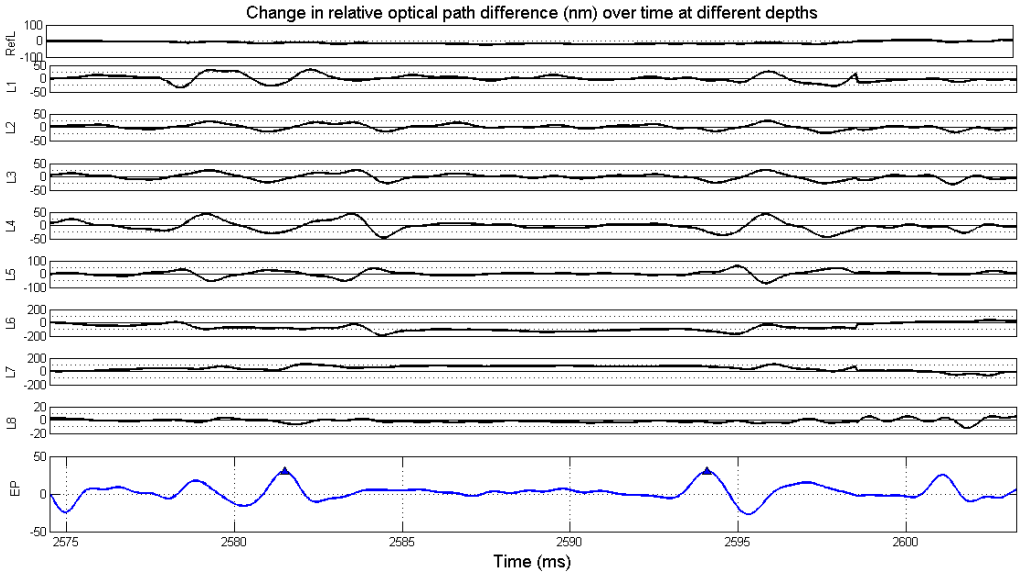

Fig. 4.18 Depth resolved activity (case 4)

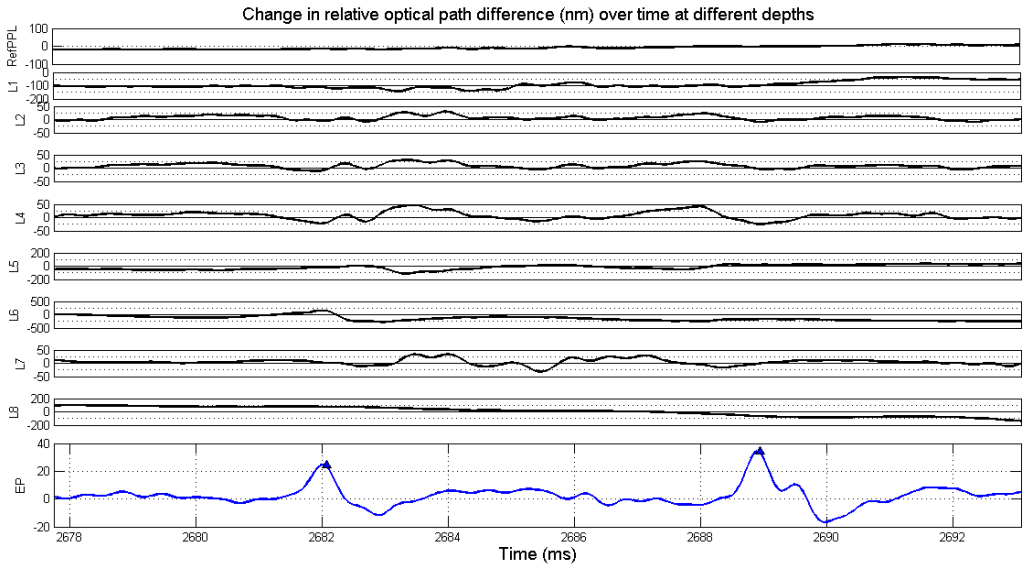

Fig. 4.19 Depth resolved activity (case 5)

9. Discussion

This study was focused on non-contact optical detection of the transient thickness changes in axons during activity. This is the first study, to the best of our knowledge, where functionally stimulated neural activity in *Limulus* nerve has been optically detected by phase-resolved OCT. This first step of the study has demonstrated that OCT can be a non-contact recording tool to study neurons.

Imaging and phase measurement results both from reference-arm configuration and common-path configuration OCT system have been demonstrated. Having both setups implemented in the same system allowed for comparing the detection sensitivity of two setups for future applications. While regular reference-arm configuration provides more

flexibility for structural imaging, common-path configuration provides improved phase stability and sensitivity. This improved phase stability allowed us to reproduce the results of optical detection of neural activity on more regular basis in comparison to the reference-path configuration. In order to ensure reliable optical measurements, recorded phase data was chosen for analysis only if the signal strength was above a threshold (described in previous section). Poor signal intensity produces random phase jumps and if the phase noise becomes higher than the activity associated phase changes, it becomes impossible to detect activity.

As mentioned earlier, none of the optical recordings shown here was averaged, i.e. these are single shot measurements with some low level filtering for removing 60Hz noise. The control experiment described earlier serves as a way to make sure that the changes in optical phase measurement truly reflects nerve activity. Following the first set of recording, KCl was added to the nerve solution to block the action potentials and the results in optical and electrical recordings confirmed the absence of activity.

There is one limitation of functional stimulation which is reduced flexibility in data analysis. Selective stimulation of the ommatidia has not been incorporated into our system yet. Due to bulk stimulation of the entire compound eye, almost all the ommatidia are stimulated and their axons carry action potentials. Since action potentials are spontaneously arriving to the optical measurement site from multiple sources (600-700 ommatidia in a single lateral compound eye [21]), it is difficult to correlate the optical and electrical recordings from so many axons unless very few axons (~10-15) are

chosen for electrical and optical recording. This can be ensured by fine dissection of the nerve sample and making the tip of suction electrode glass capillary tube very small (diameter of tip should be just enough to allow only the axons chosen). However, despite these drawbacks, there are several benefits of using functional stimulation. One easily observable advantage is that it allows for stimulation artifact free electrophysiology recording. But the most important advantage of functional stimulation is that it allows for studying the neurons in a setting more representative of real network environment. This makes it easier to move to the next step of the long term study where a small network of neurons can be monitored optically by using this OCT based electrode. The reason also behind choosing *Limulus* as an animal model is that *Limulus* lateral compound eye and its optic nerve is a very well-established model for studying behaviors of a small neural network such as lateral inhibition [22].

Currently, one drawback of this limited study is that the optical recording by OCT is limited to only one depth profile under analysis and this single depth profile does not contain all the axons that go into the suction electrode. Electrical recording detects activity in any and all the axons in the suction electrode. It is therefore, expected and very likely that there will be a large percentage of cases where there is electrical activity without any activity in optical measurements (i.e. false negatives). To overcome this drawback, we are currently working towards developing methods to scan multitude of spatial locations. This multipoint scanning of optical electrode will enable the detection of activity from larger number of axons and therefore improve the overall sensitivity of the method.

Chapter 5
Control Experiments

After successful optical detection of action potential induced rapid thickness change of nerve, the accuracy of the developed system was systematically verified. To evaluate the accuracy, two controlled experiments were carried out in a step by step manner. The first level of control experiment was to block the nerve impulse propagation by adding excess KCl to the Ringer solution. The second control experiment uses a simple cold block for switchable control of the deactivation and reactivation of action potential propagation. In three different stages of cold block, neural activity is monitored in both electrical and optical recordings. Details of these experiments are described in the following sections.

1. Experiment with Excess KCl

Addition of excess KCl in nerve solution blocks the propagation of action potentials due to imbalance in intracellular and extracellular ion concentration [18]. A schematic explaining the addition of KCl to the Ringer solution is provided in Figure 5.1. Figure 5.2 shows electrical recording and simultaneous optical recording (thickness change measurement) for two cases: before adding any excess KCl to the solution and after adding KCl to the solution. The plots in Figure 5.2a shows that action potentials were detected both in electrical and optical recording. The second part of this plot shows the recording after KCl was added to the solution. KCl was introduced to the solution

without altering any components of the whole experiment setup. The activity of nerve ceased within a second after KCl addition. Fig. 5.2b also shows the recording after KCl was added to the solution but for longer time scale. Both electrical and optical recording confirms the presence of no activity (no action potentials or thickness changes). The similarity in electrical and optical recordings from the deactivated nerve proves the validity of the optical measurements. The similarity in electrical and optical recordings from the deactivated nerve proves the validity of the optical measurements. Therefore, this control experiment is a strong indication that the results of previous section truly reflect the optical detection of thickness change.

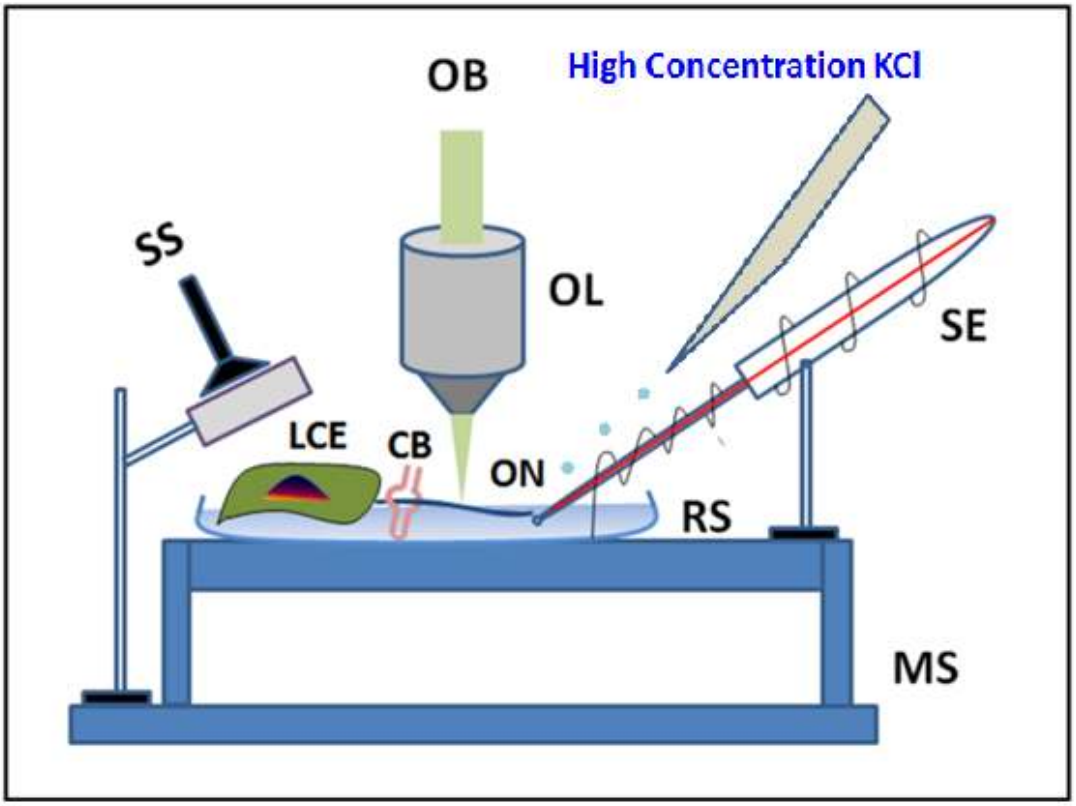

Fig. 5.1 Setup for potassium chloride (KCl) experiment

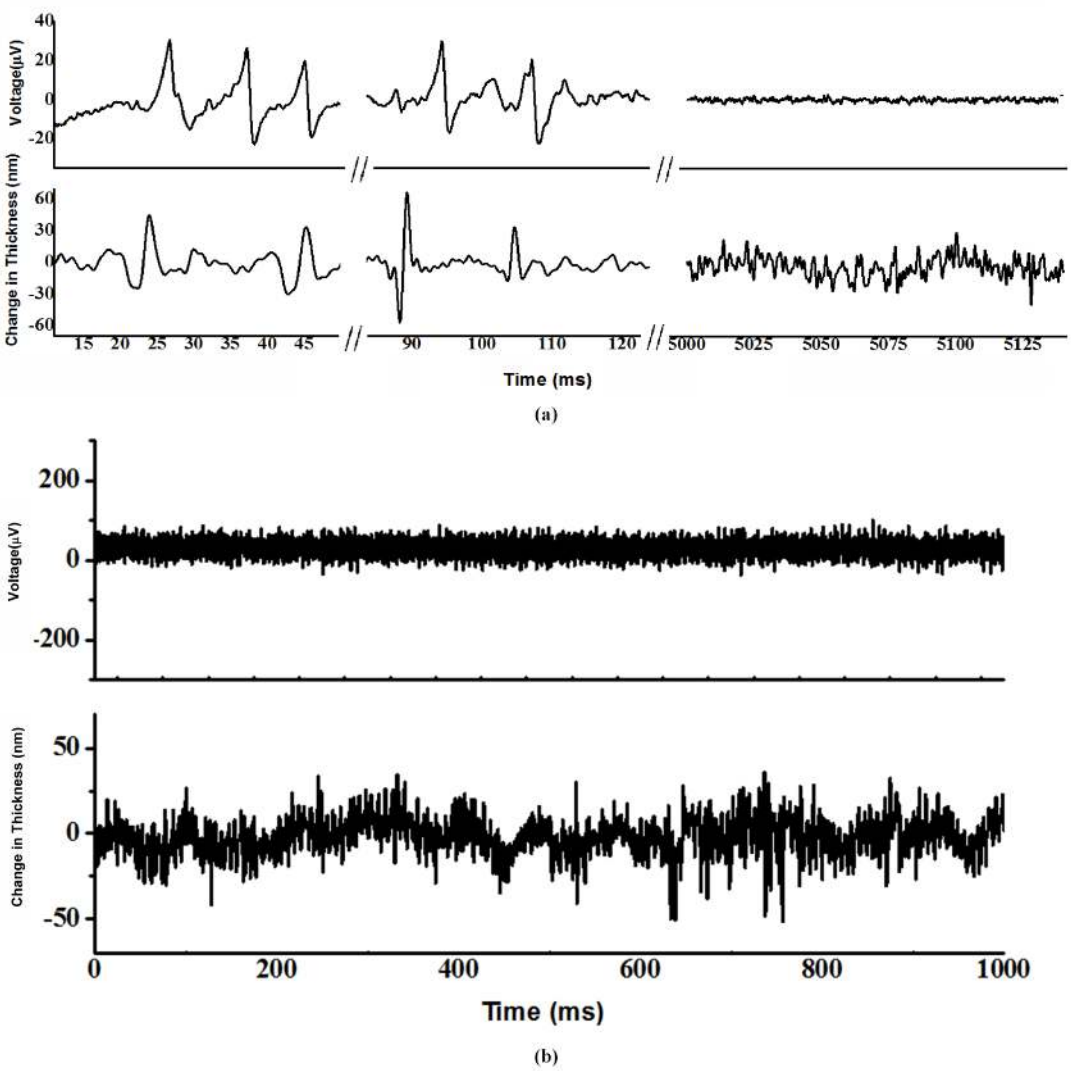

Fig. 5.2 Electrical and optical recordings of neural activity in *Limulus* optic nerve. Data recorded before adding KCl (a) and after adding KCl (b) are shown here for comparison.

2. Cold Block Experiment

A frozen nerve exhibits much higher electrical resistance than in normal condition [103, 104]. As a result, at low temperatures where nerve experiences freezing condition, the conduction of impulses decreases to almost zero and this have made cold block as a suitable agent for blocking action potential in a nerve. In a cold block, a small section of nerve is introduced inside the cold block and temperature is gradually decreased within that block by using some cooling medium, cold salt solution, for example [103]. The nerve starts to freeze at a negative temperature and under these conditions no action potential propagation or alternatively, no structural change of nerve is expected to be observed through optical recording. The advantage of using cold block is that the process of inactivating the nerve is rapidly reversible which means that with the increase of temperature, nerve recovers its active state and starts conducting action potentials again. In our experiment, another set of optical recording were carried out once the nerve has recovered from its blocked state and being able to propagate impulses.

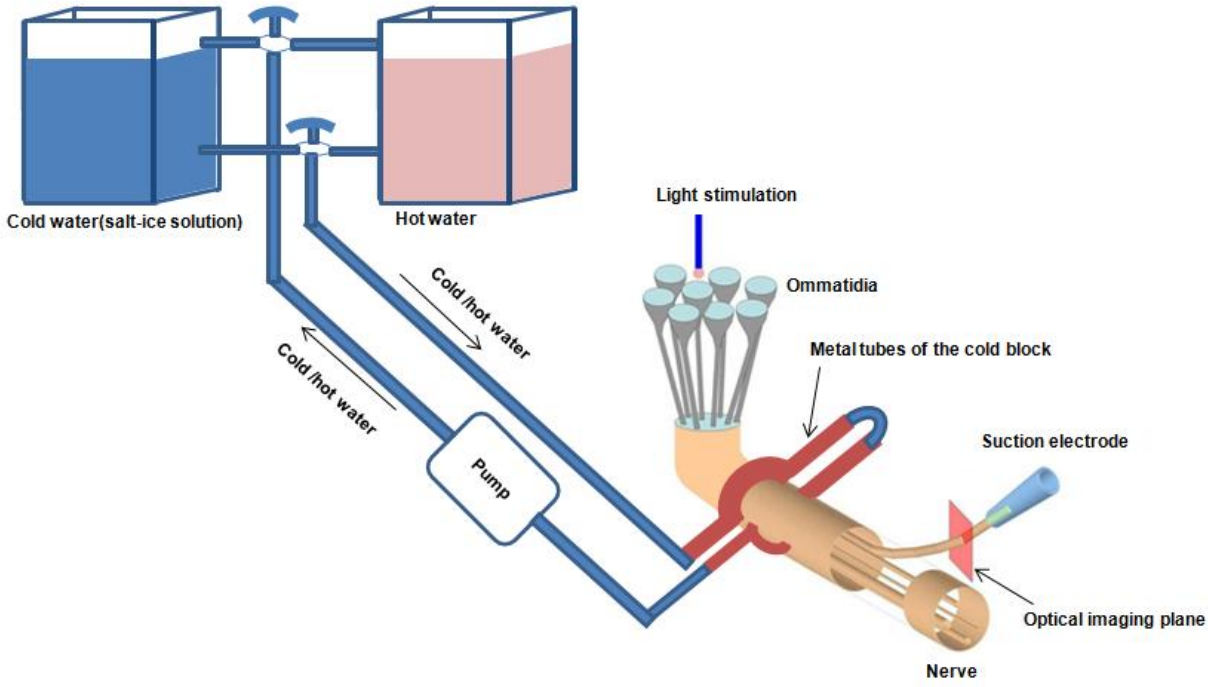

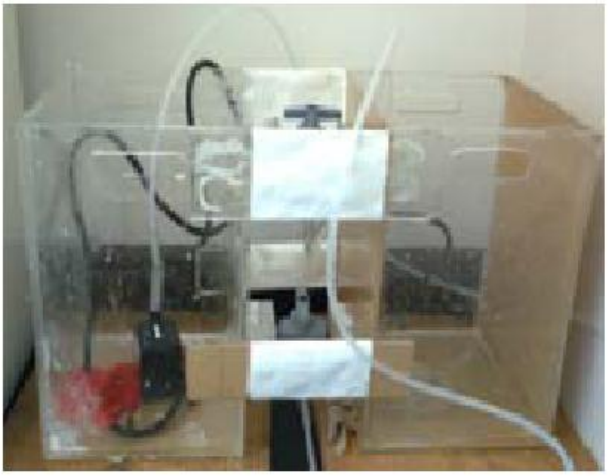

Fig. 5.3 (a) An illustration of the experimental setup of the cold block to activate/deactivate action potential propagation through the nerve while electrical recording is done at the end of the nerve (b) Implemented cold block. Two tanks to contain cold and hot solution(left) and two metallic tubes of the cold block(right) [108].

A metal tube based cold block was built to control the temperature around the nerve sample (Figure 5.3). Two water reservoirs were made from Plexiglas to contain hot and cold water. Plastic tubing was used to carry these liquid toward the cold block which is a simple block of two metal tubes placed on top and bottom of the nerve. When the cold water is passed through these tubes, the temperatures drop down gradually around the nerve and as it reaches close to 2^0C or lower, the nerve stops conducting action potentials. Once the hot water switch is turned on in place of cold water, the temperature starts to rise again and the nerve starts conducting as it reaches close to room temperature (22^0C). During experiment, simultaneous electrical and optical recording was done for all three sequential steps: before deactivation of nerve (regular state, no liquid flow), after deactivation (by running cold water) and after reactivation of nerve (by running hot water). Figure 5.4 shows representative recordings in three stages. Figure 5.4a shows electrical and optical recording during first stage (before deactivation). The electrical spikes are accompanied by simultaneous changes in nerve thickness (i.e. change in OPL). Figure 5.4b shows the recording when the nerve was deactivated by cold block operation in cold mode. Both recordings show absence of activity. Later, in third stage, the nerve was reactivated using hot mode of cold block operation and the recording shows the presence of action potentials and corresponding changes in thickness of nerve. These recording in three stages of cold block operation demonstrate the validity of optical recordings of activity. Figures 5.5 to 5.13 show more examples of simultaneous electrical and optical recording in different states of cold block operation.

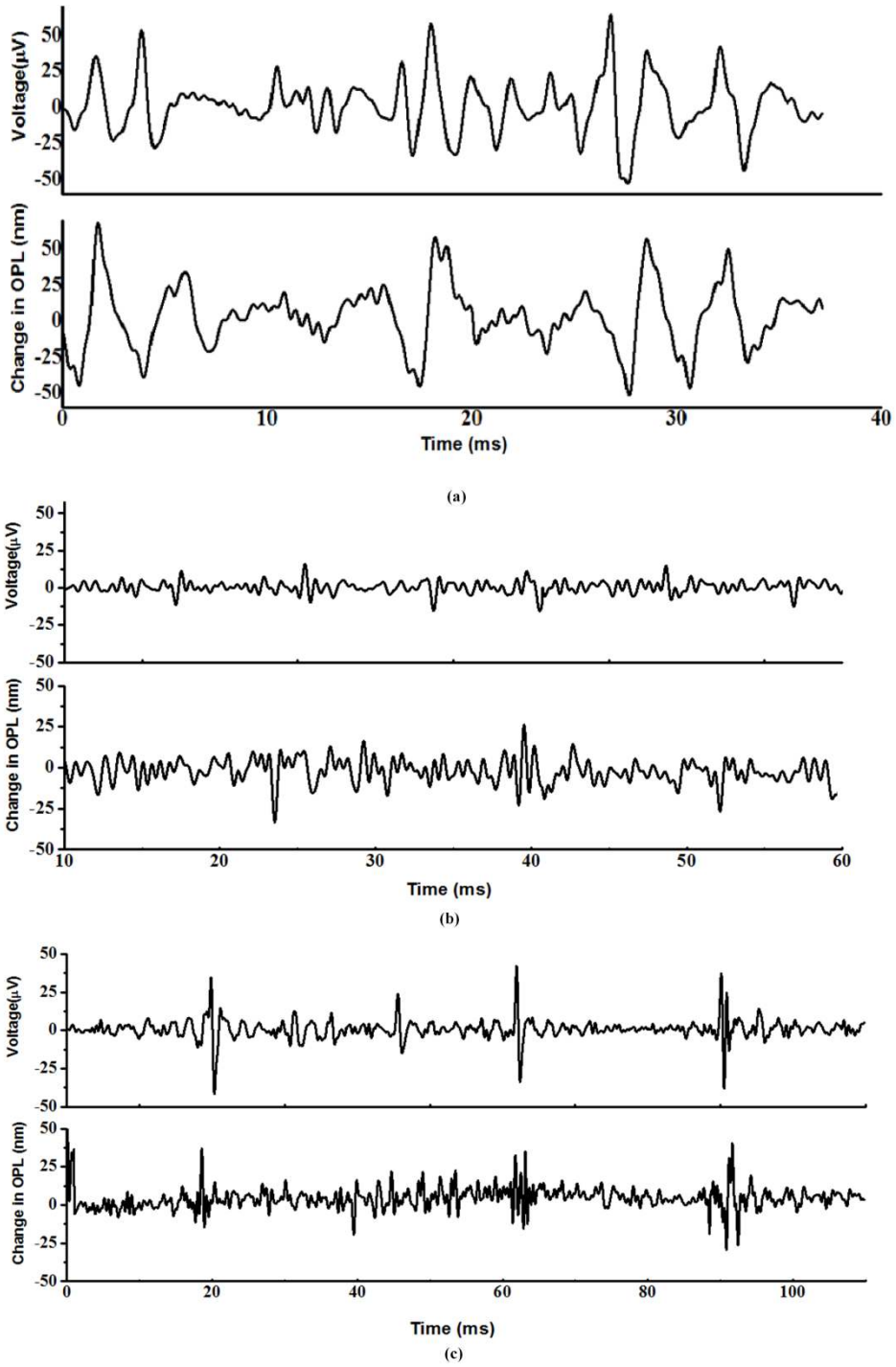

Fig. 5.4 Simultaneous electrical and OCT recordings from functionally stimulated optic nerve during three stages of cold block operation. (a) Before cold block operation, (b) after cold mode of cold block operation and (c) after hot mode of cold block operation.

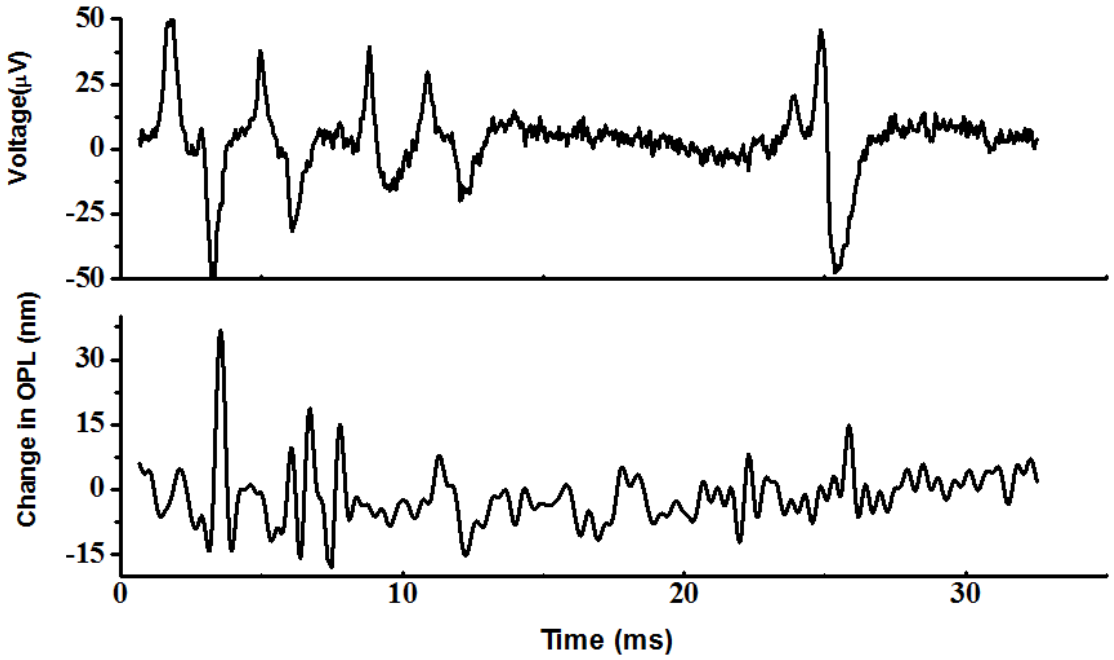

Fig. 5.5 Simultaneous electrical and OCT recordings from functionally stimulated optic nerve during activated state (before cold block operation, case 1)

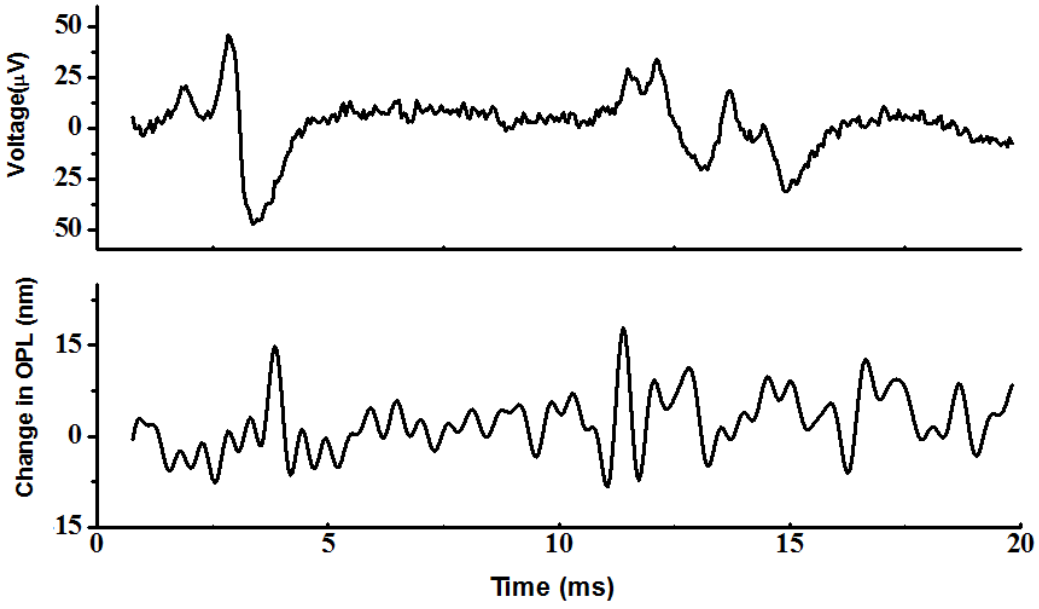

Fig. 5.6 Simultaneous electrical and OCT recordings from functionally stimulated optic nerve during activated state (before cold block operation, case 2)

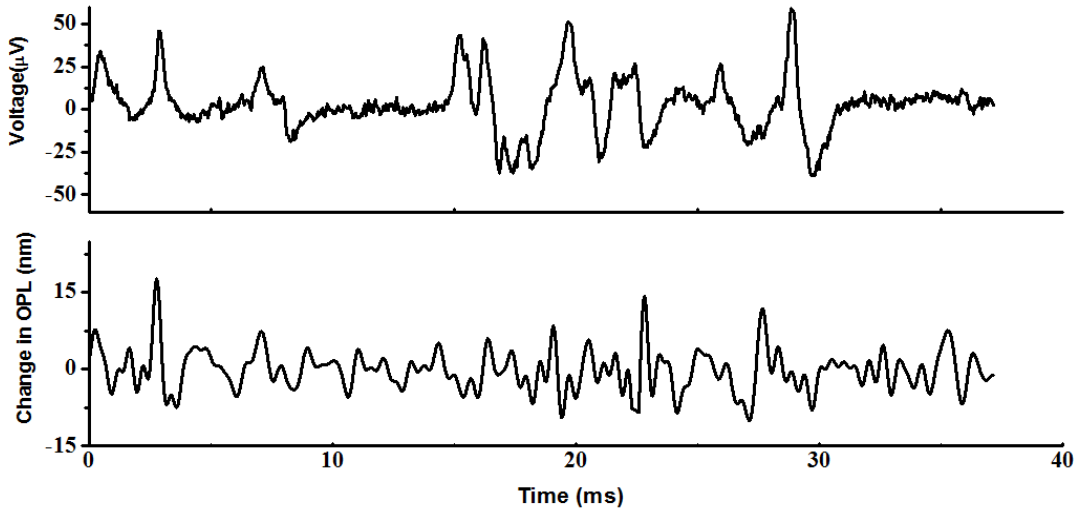

Fig. 5.7 Simultaneous electrical and OCT recordings from functionally stimulated optic nerve during activated state (before cold block operation, case 3)

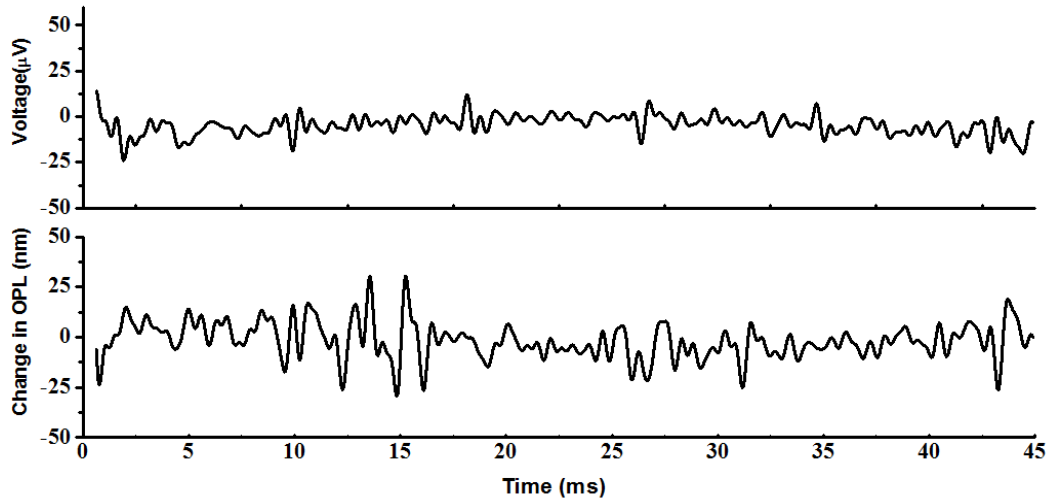

Fig. 5.8 Simultaneous electrical and OCT recordings from functionally stimulated optic nerve during deactivated state (after cold block operation, case 1)

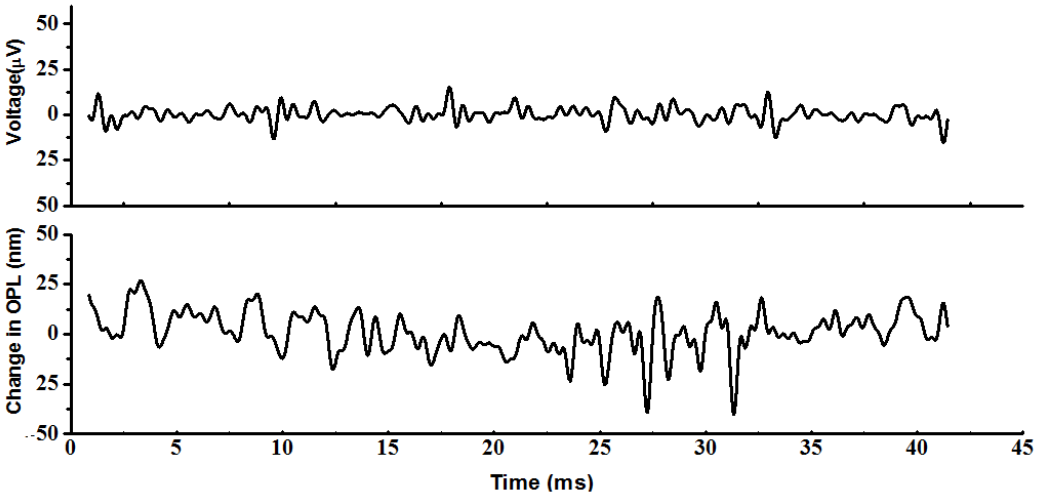

Fig. 5.9 Simultaneous electrical and OCT recordings from functionally stimulated optic nerve during deactivated state (after cold block operation, case 2)

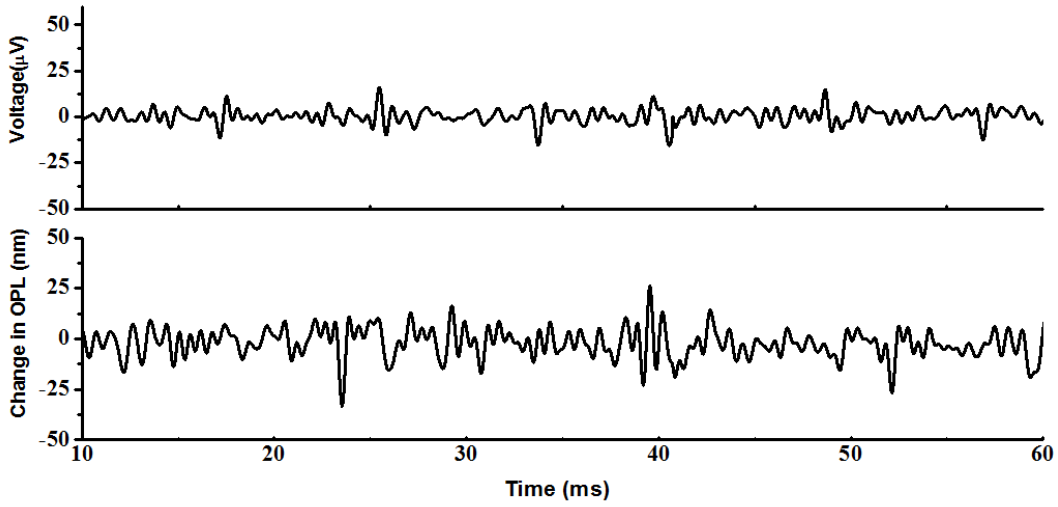

Fig. 5.10 Simultaneous electrical and OCT recordings from functionally stimulated optic nerve during deactivated state (after cold block operation, case 3)

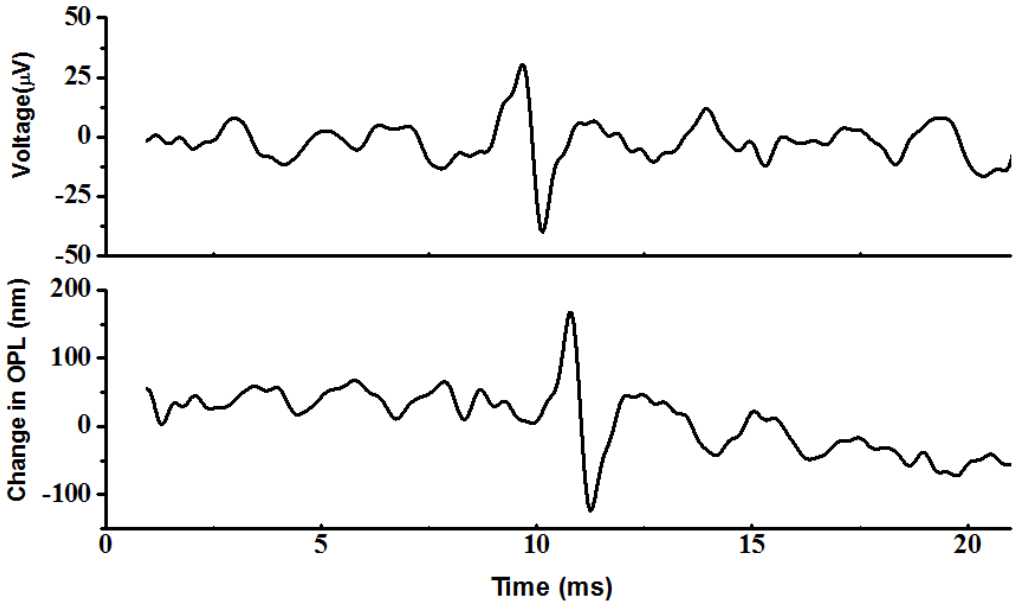

Fig. 5.11 Simultaneous electrical and OCT recordings from functionally stimulated optic nerve during reactivated state (after cold block operation, case 1)

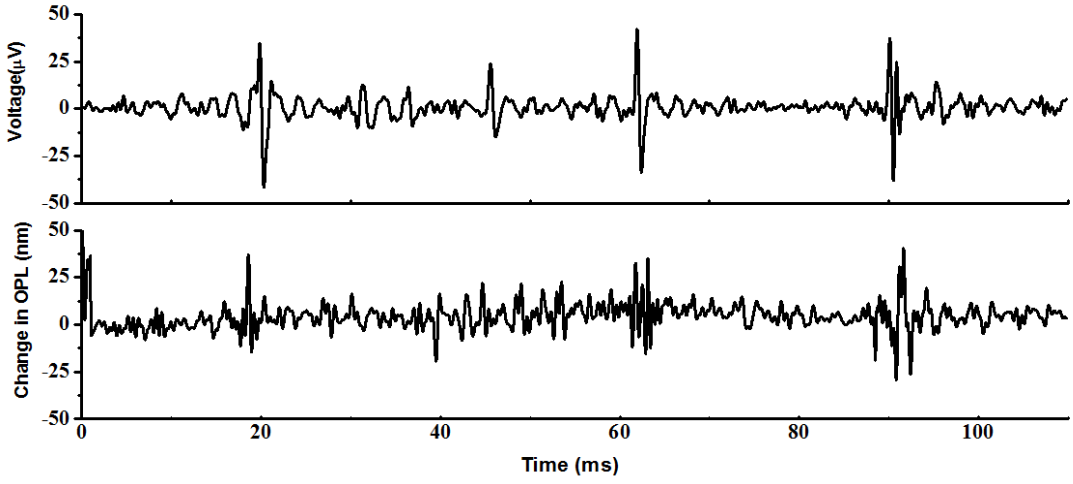

Fig. 5.12 Simultaneous electrical and OCT recordings from functionally stimulated optic nerve during reactivated state (after cold block operation, case 2)

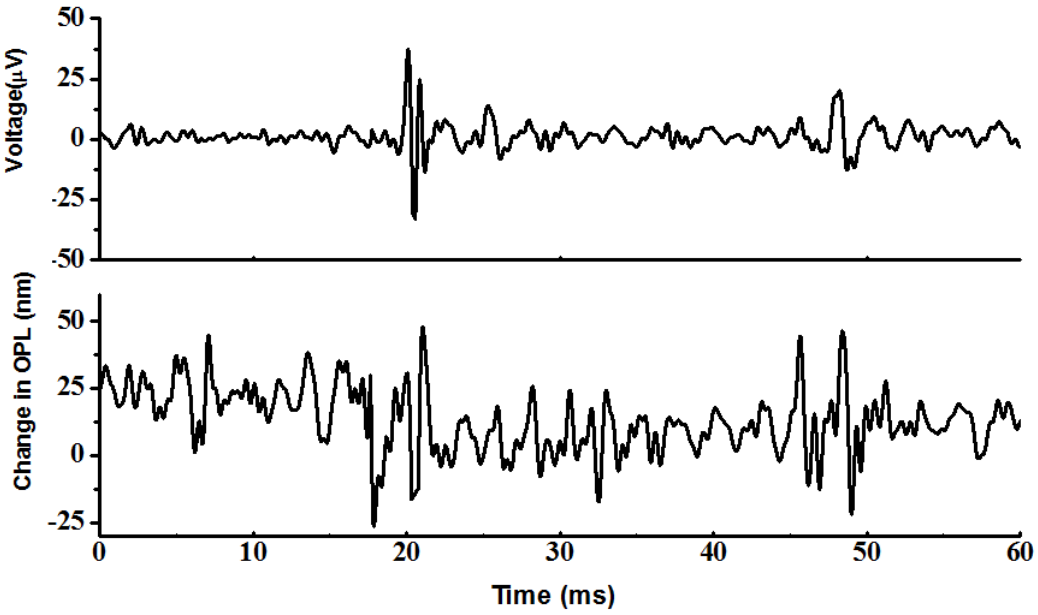

Fig. 5.13 Simultaneous electrical and OCT recordings from functionally stimulated optic nerve during reactivated state (after cold block operation, case 3)

3. Discussion

Recording of nerve activity in electrical and optical method are quite different in nature. In case of electrical recording, the suction electrode collects signal from all the axons inside its capillary glass tube and burst of single action potentials are observed. In case of optical recording, one depth profile (A-line) is chosen from a cross-section image of the nerve bundle. The chosen depth profile contains multiple axon bundles at different depths and the thickness change is measured for each bundle. A MATLAB program has been written for comparing the thickness changes of all these bundles with the timings of action potentials in electrical recording.

One limitation of optical recording is that the phase noise is highly dependent on the signal intensity or signal-to-noise ratio (SNR) of a measurement and change in signal strength directly affects the minimum observable thickness change. Previous studies by Yazdanfar *et al*. and Park *et al.* have independently demonstrated that phase noise or minimum detectable phase difference $(\sigma_{\Delta\varphi})$ and SNR are related by this expression, $\sigma_{\Delta\varphi} = (SNR)^{-1/2}$ [18, 106]. To minimize the fluctuation in backscattered intensity due to undesired vibration of the sample, the surrounding area of the sample was kept free from any airflow or movement of objects. The common-path configuration also reduced most of the common-mode environmental noises. Even after all those precautions, the data was reevaluated in post processing to ensure artifact free recording. In most of the successful optical detection in this study, we have observed that the thickness change of the axon bundle corresponding to a single action potential was usually in the range of 20-40nm. Therefore, a SNR of 15dB was used as a threshold signal intensity which corresponds to a minimum observable thickness change of ~11nm. Any measurement with an SNR lower than 15dB, although may be representing any thickness change, was rejected during evaluation.

Following the above routine, multiple sets of electrical and optical recording data have been analyzed and sensitivity is calculated from those data using this expression: sensitivity = true positives / (true positives + false negatives). True positive (TP) refers to the event where both electrical and optical system detected activity. False positive (FP) refers to the event where optical recording shows sign of activity but no activity found in electrical recording. False negative (FN) are the events where activity detected by

electrical method is absent in optical method (in previous section, second action potential in recording of before adding KCl is an example of FN). True negative (TN) is the case where there is no activity detected in both methods (in previous section, recordings after adding KCl is an example of TN). However, since the number of impulses in each trial is not same in case of functionally stimulated compound eye, calculation of true negatives was not applicable in this study. 44 events (action potentials) were analyzed for this calculation and 19 true positives, 25 false negatives and 7 false positives were found. This gives to a sensitivity of 43.18%. False positive cases may be the result of optical measurement from axons which were not in suction electrode. Since the number of axons scanned for phase measurement is lower compared to the axons in the suction electrode, it is quite likely that there will be a large percentage of cases of false negatives. More details about this sensitivity analysis are in discussion section.

Chapter 6

Detection of Neural Activity in Brains

1. Epileptic Activity in Mouse Brain Slice

Epileptic or seizure like activity is generally characterized by rapid periodic and unpredictable burst of electrical activity. Recent studies have shown that there are also changes in optical properties of brain tissues during the onset of seizure [111, 112]. The goal of this study was to find out the how optical changes are preceding the electrical activity. We have observed a time delay of 50-60 seconds between optical and electrical activity during this experiments.

Experimental Setup

Acute hippocampal slices (thickness 300 µm) were prepared from wild-type (P10-P20 old) mice (Black mouse (C57BL/6), The Jackson Laboratory, Bar Harbor, ME). Mice were anesthetized and decapitated according to UC Riverside IACUC approved protocols. The brain was rapidly removed and slices were cut using Leica 1200 vibrotome in low Ca ice-cold ACSF, followed by recovery in normal ACSF for 1 h at 32°C. Slice of choice was placed on a top of microelectrode array (perforated 10X6 MEA array, electrode diameter 10 µm, electrode to electrode distance 90 µm) so that

hippocampus region of the brain covered most of the array. Slice then was brought under OCT imaging system (OCT system: center wavelength 800 nm, axial resolution 1.66 µm, lateral resolution 3µm). ACSF solution was gravity flowed on top of the slice at 3-5 ml/min rate. Control measurement (ACSF) followed by application of 10mM KCl ACSF to induce seizure activity. Simultaneous volumetric OCT and electrical data were recorded during control conditions and during seizure activity. Then the acquired optical and electrical data were post-processed using MATLAB routines.

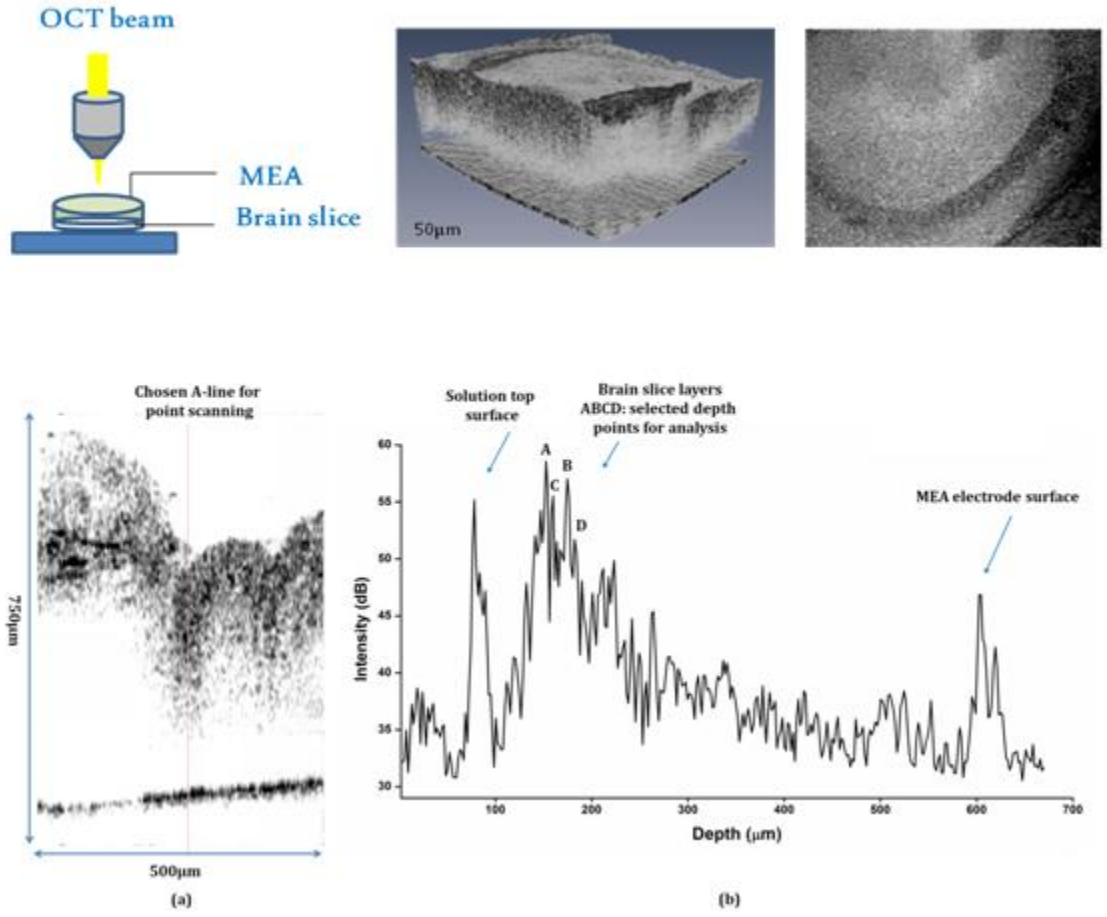

Fig. 6.1 (a) Experimental set up for brain slice-MEA-OCT experiment. (b) OCT volumetric and (c) *en face* image of 300µm thick brain slice, the dark structure representing the hippocampal region. (d) OCT cross-section of same brain slice. (e) OCT depth profile showing intensity at different depths of the chosen A-line in (d).

MEA recorded the electrical activity, amplified it and then saved it on to the computer. Simultaneously, OCT beam was focused on the brain slice to scan the hippocampus region (Dentate Gyrus and CA areas). A 3D OCT scanning was performed to generate a volumetric image of the scanned region. Then a cross-section was examined to choose an A-line for M-scanning. M-scanning is scanning same depth profile (A-line) over time and this yields phase measurements data. From analyzing the data, the change in intensity and change in phase difference (i.e. corresponding thickness change) were plotted and compared with MEA recorded electrical activity.

Detected Optical Changes in Brain Slice

Four depth points (A, B, C, D) were chosen from the OCT intensity depth profile in Figure 6.1(e) for data analysis. Phase differences between a pair of points over time were measured and the standard deviations were also calculated. These values, along with combined signal intensity of the two depth points and the electrical recording from microelectrode array (MEA) were plotted. Post experiment analysis revealed that signal intensity (SNR) decreases sharply almost about 30-40 seconds before the epileptic burst activity starts. Change in mean phase difference and standard deviation of phase also showed significant changes before and during activity. The results are shown below for four different pairs of depth points, AB, AC, AD and BC.

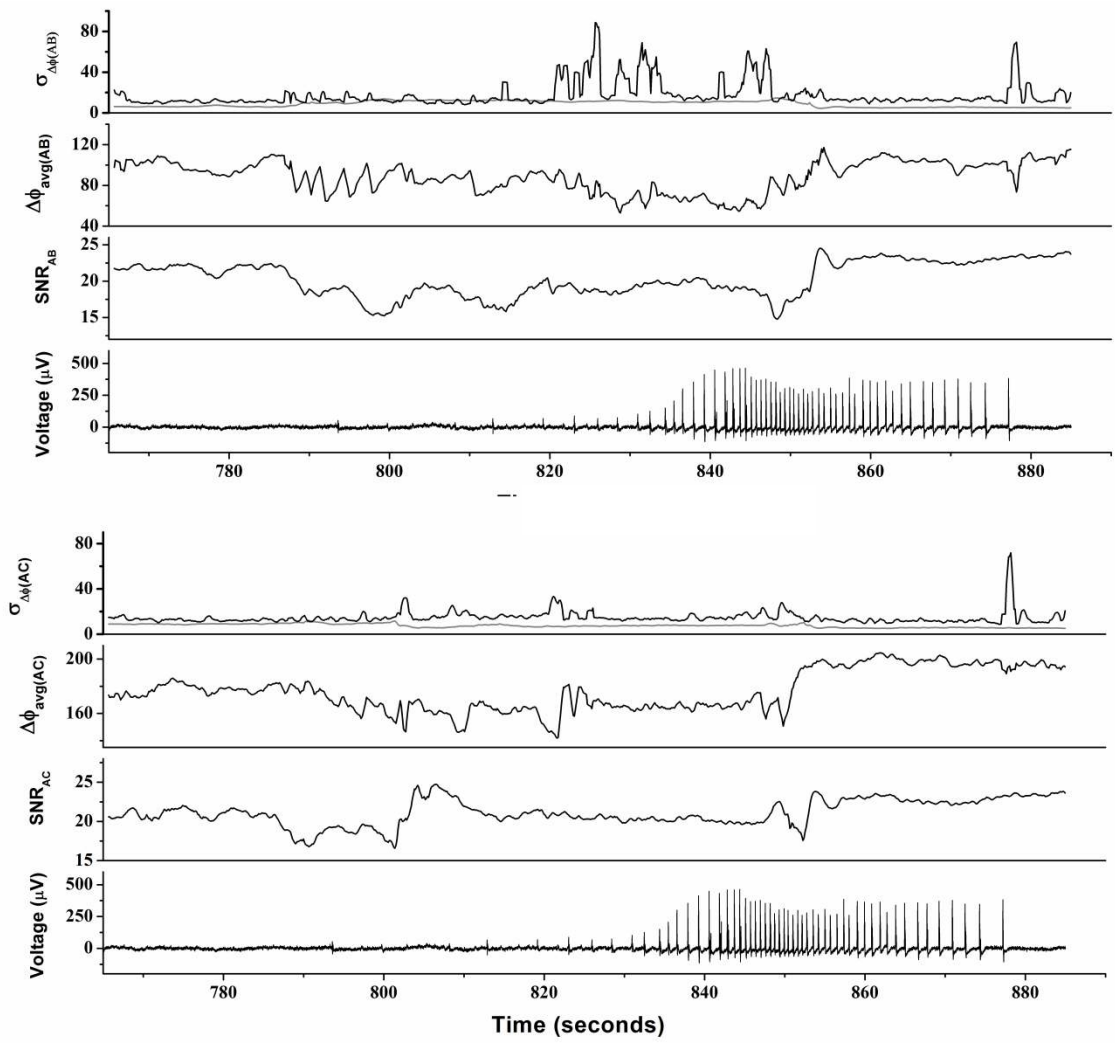

Fig. 6.2 Optical changes in brain slice before and during epileptic activity (a) for depth pair AB, (b) for depth pair AC.

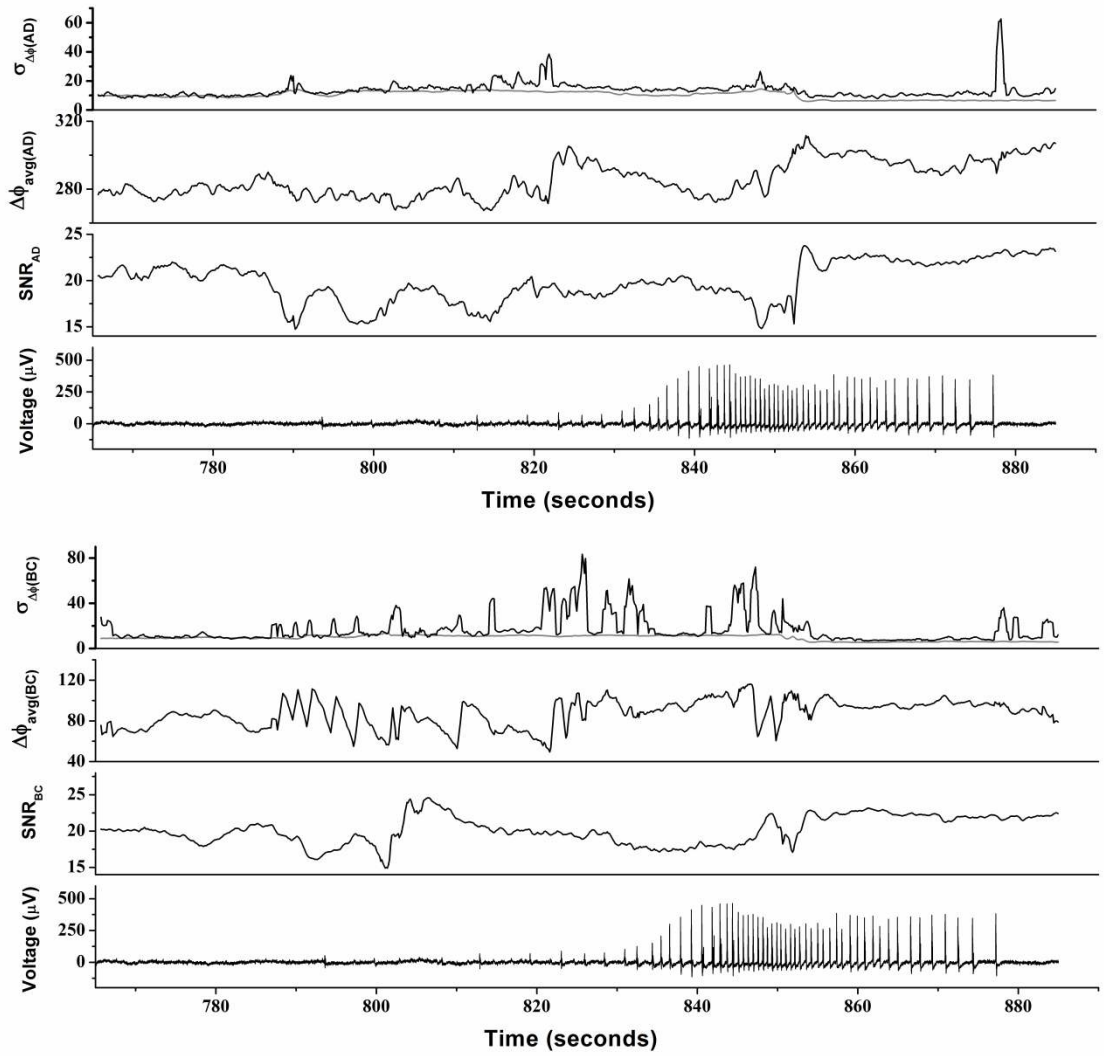

Fig. 6.3 Optical changes in brain slice before and during epileptic activity (a) for depth pair AD, (b) for depth pair BC.

2. Neural Activity in Fruit Fly Brain

Fruit fly brain is a very well known sample in neuroscience research. Earlier studies have shown the periodic change in fluorescence of the brain cells during activity. The goal of this study was to investigate the change of scattering in brain tissue during neural activity.

Experimental Set up

Fruit fly brain was dissected and placed on a Petri dish in a solution. OCT image was acquired and reconstructed volume of the brain was generated. A section of the volumetric OCT image of the brain stem is shown in Figure 6.4c. For first five minutes, one OCT volume was acquired at every minute. Thereafter, hormone was injected into the solution to induce neural activity. Volume was acquired at every minute for next 30 minutes. The OCT raw data were later processed to generate the volume and integrated *en face* image. From the integrated *en face* image, average intensity was calculated for all 35 volume data.

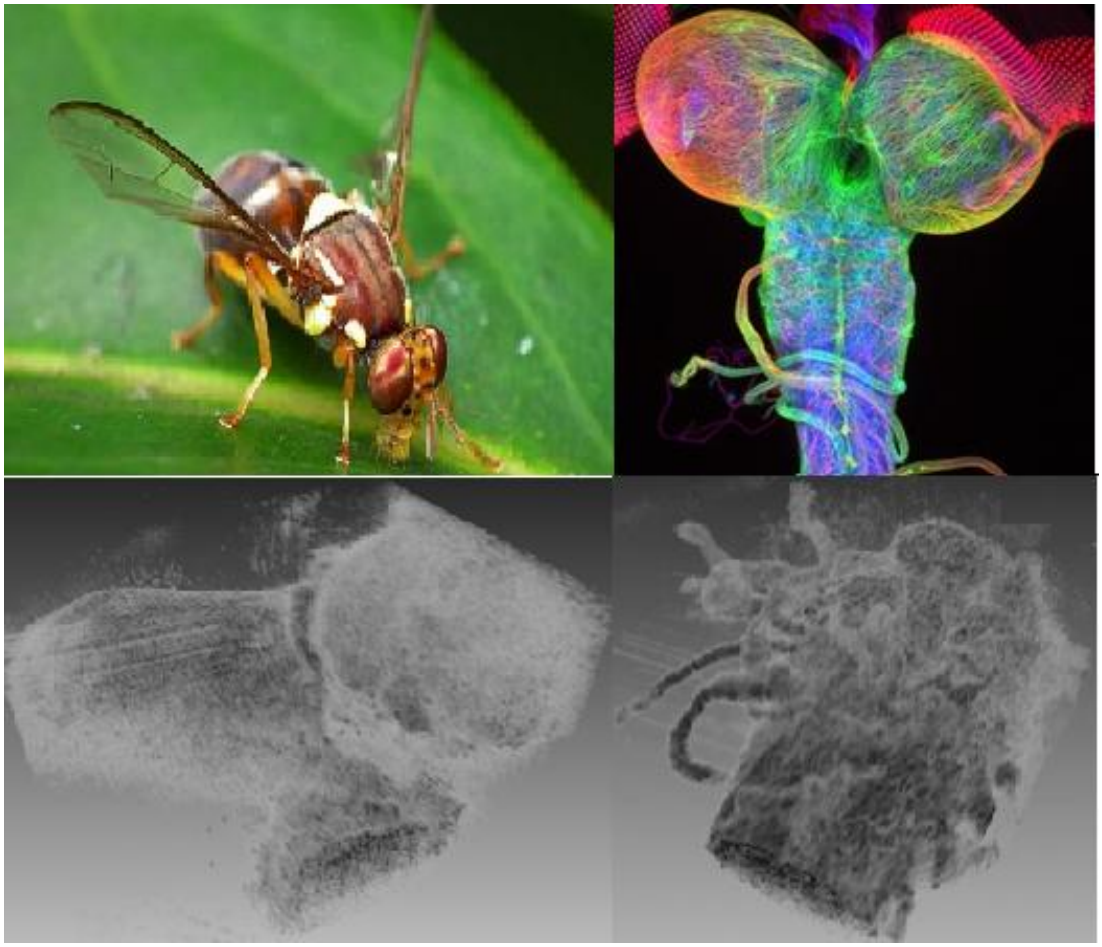

Fig. 6.4 Imaging fruit fly brain using OCT. (a) Snapshot of a fruit fly (b) Brain (top) and stem (bottom) of a fruit fly brain (c) OCT generated image of fruit fly brain lobe and stem. [109. 110]

3. Detected Optical Changes in Brain Tissues

OCT volumes were acquired at every minute for thirty five minutes before and after injecting hormone to the solution. The depth layers from each volume were added to get an integrated volume or an *en face* image and the average intensity from this integrated volume was calculated. The average intensity plot in Figure 6.5b shows that the intensity

started increasing 6-7 minutes after hormone injection and rapidly increases to a maximum within 12-13 minutes. The intensity gradually started to decreases after that and it was decreasing till the last data point acquired at 35th minute of data acquisition. This is a very significant finding because fruit fly brain is known to have a increase in neural activity within 6-10 minutes of hormone injection and after 10-15 minutes, it starts going back to normal level [113]. From OCT data, we have observed very similar timeline of activity and in addition, the optical changes have shown a good timing correlation with the change in fluorescence (fluorescence not shown here).

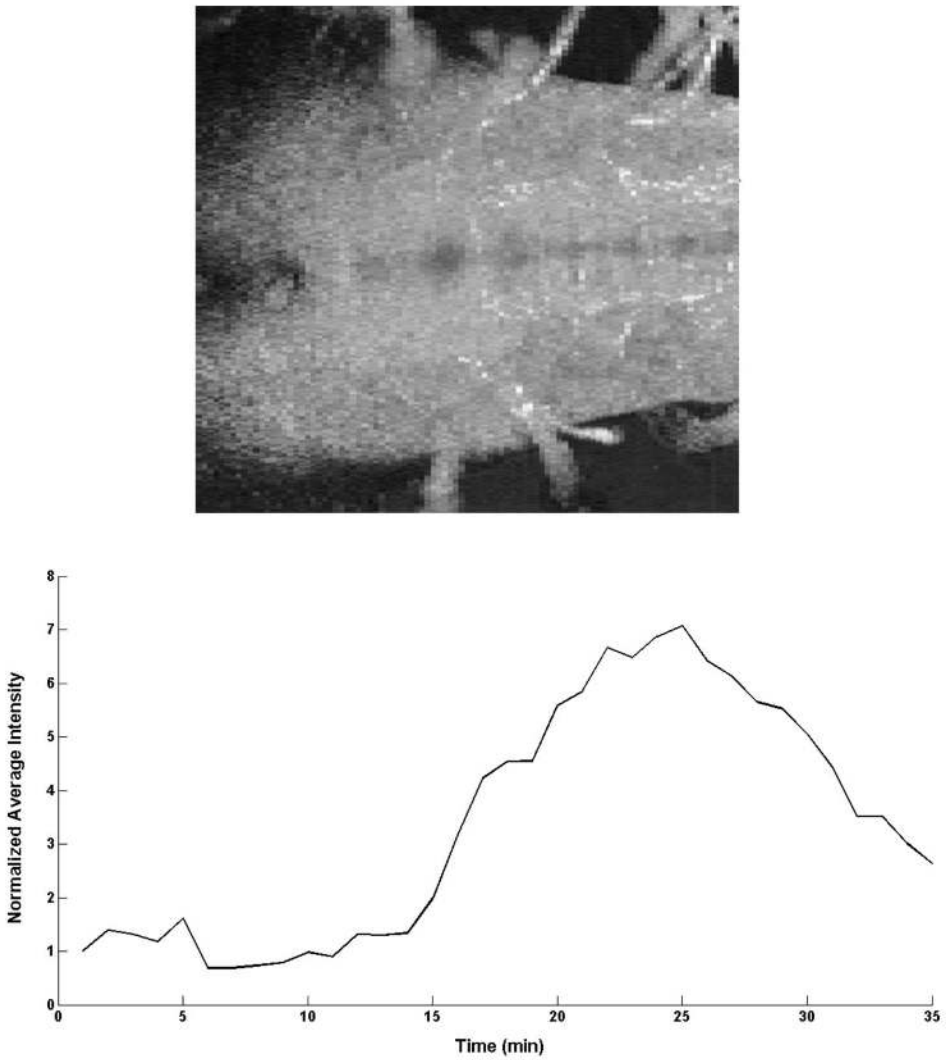

Fig. 6.5 Analysis of volumetric image of fruit fly brain stem. (a) an integrated volume (*en face*) by adding the depth layers from a volumetric image. (b) Graph showing the average intensity calculated from (a) for every minutes of recording.

Conclusion

Optical detection of neural activity is a well suited technique for applications where no physical contact between electrode and nerve is desired. In this study, phase-resolved OCT has been demonstrated to be capable of measuring the nerve thickness changes associated with action potential propagation. The optical detection of activity is also verified through deactivation of action potential propagation (using KCl). Because of the undesired fluctuations in phase measurement due to environmental factors, the rate of success is still not as good as the gold standard electrical recording method. However, these results have shown that OCT can detect thickness changes associated with action potential for small sized *Limulus* axons and to the best of our knowledge, for the first time this study has demonstrated single shot optical detection of functionally stimulated neural activity. Current and future efforts are focused towards the improvement of phase sensitivity of the system to increase the overall accuracy in detection.

References and Bibliography

1. Matthews GG. **"**Neurobiology, Molecules, Cells and Systems", 2001; Second Edition,
2. Nicholls JG, Martin AR, Wallace BG. "From Neuron to Brain: A Cellular and Molecular Approach to the Function of the Nervous System". 1992; Third Edition.
3. Shepherd GM. "Neurobiology". 1994; Third Edition.
4. Brock LG, Coombs JS, Eccles JC. "The Recording Of Potentials From Motoneurones With An Intracellular Electrode". Journal of Physiology-London. 1952;117(4):431-60.
5. Fatt P, Katz B. "Membrane Potentials At The Motor End-Plate". Journal Of Physiology-London. 1950;111(3-4):P46-P7.
6. Fatt P, Katz B. "Some Observations On Biological Noise". Nature. 1950;166(4223):597-8.
7. Graham J, Gerard Rw. "Membrane Potentials And Excitation Of Impaled Single Muscle Fibers. Journal Of Cellular And Comparative Physiology". 1946;28(1):99-117.
8. Ling G, Gerard Rw. "The Normal Membrane Potential Of Frog Sartorius Fibers. Journal Of Cellular And Comparative Physiology". 1949;34(3):383-96.
9. Nastuk WL, Hodgkin AL. The Electrical Activity Of Single Muscle Fibers. Journal Of Cellular And Comparative Physiology. 1950;35(1):39-73.
10. Weidmann S. Electrical Characteristics Of Sepia Axons. Journal Of Physiology-London. 1951;114(3):372-81.
11. Hamill Op, Marty A, Neher E, Sakmann B, Sigworth Fj. "Improved Patch-Clamp Techniques For High-Resolution Current Recording From Cells And Cell-Free Membrane Patches". Pflugers Archiv-European Journal Of Physiology. 1981;391(2):85-100.
12. Pine J. "Recording Action-Potentials From Cultured Neurons With Extracellular Micro-Circuit Electrodes". Journal Of Neuroscience Methods. 1980;2(1):19-31.
13. Meister M, Pine J And Baylor Da, "Multi-Neuronal Signals From The Retina - Acquisition And Analysis," J Neurosci Meth 1994;51:95-106.
14. Warren Dj, Fernandez E And Normann Ra, "High-Resolution Two-Dimensional Spatial Mapping Of Cat Striate Cortex Using A 100-Microelectrode Array," Neuroscience 2001;105:19-31.

15. Vetter Rj, Williams Jc, Hetke Jf, Nunamaker Ea And Kipke Dr, "Chronic Neural Recording Using Siliconsubstrate Microelectrode Arrays Implanted In Cerebral Cortex," Ieee Trans Biomed Eng 2004;51:896-904.
16. Hosoya T, Baccus Sa And Meister M, "Dynamic Predictive Coding By The Retina," Nature 2005;436:71-77.
17. Park Bh, Pierce Mc, Cense B, De Boer Jf. “Real-Time Multi-Functional Optical Coherence Tomography”. Optics Express. 2003;11(7):782-93.
18. Park Bh, Pierce Mc, Cense B, Yun Sh, Mujat M, Tearney Gj, Et Al. Real-Time Fiber-Based Multi-Functional Spectral-Domain Optical Coherence Tomography At 1.3 Mu M. Optics Express. 2005;13(11):3931-44.
19. Hubel Dh, Wiesel Tn. Receptive Fields Of Single Neurones In The Cats Striate Cortex. Journal Of Physiology-London. 1959;148(3):574-91.
20. Hubel Dh, Wiesel Tn. Receptive Fields, Binocular Interaction And Functional Architecture In Cats Visual Cortex. Journal Of Physiology-London. 1962;160(1):106-&.
21. Roth Bj, Wikswo Jp. The Magnetic-Field Of A Single Axon - A Comparison Of Theory And Experiment. Biophysical Journal. 1985;48(1):93-109.
22. Wikswo Jp. “A Low-Noise Low Input Impedance Amplifier For Magnetic Measurements Of Nerve Action Currents Ieee Transactions On Biomedical Engineering”, Vol. Bme-30, No. 4, April 1983
23. Trontelj Z, Zorec R, Jazbinsek V, Erne Sn. “Magnetic Detection Of A Single Action-Potential In Chara-Corallina Internodal Cells. Biophysical Journal”. 1994;66(5):1694-6.
24. Shtrankfeld Ig And Frank Gm, "Luminescence Of Giant Nerve Fibres On Excitation," Biofizika 1964;9:321-6.
25. Levene Mj, Dombeck Da, Kasischke Ka, Molloy Rp And Webb Ww, "In Vivo Multiphoton Microscopy Of Deep Brain Tissue," J. Neurophysiol. 2004;91:1908-12.
26. Jung Jc, Mehta Ad, Aksay E, Stepnoski R And Schnitzer Mj, "In Vivo Mammalian Brain Imaging Using Oneand Two-Photon Fluorescence Microendoscopy," J. Neurophysiol. 2004;92:3121-33.
27. Kasischke Ka, Vishwasrao Hd, Fisher Pj, Zipfel Wr And Webb Ww, "Neural Activity Triggers Neuronal Oxidative Metabolism Followed By Astrocytic Glycolysis," Science 2004;305:99-103.
28. Tasaki I, Watanabe A, Sandlin R And Carnay L, "Changes In Fluorescence, Turbidity, And Birefringence Associated With Nerve Excitation,"Proc. Natl. Acad. Sci. U.S.1968;61:883-8.

29. Grinvald A, Manker A, Segal M. Visualization Of The Spread Of Electrical-Activity In Rat Hippocampal Slices By Voltage-Sensitive Optical Probes. Journal Of Physiology-London. 1982;333(Dec):269-91.
30. Grinvald A, Lieke Ee, Frostig Rd, Hildesheim R. "Cortical Point-Spread Function And Long-Range Lateral Interactions Revealed By Real-Time Optical Imaging Of Macaque Monkey Primary Visual-Cortex". Journal Of Neuroscience. 1994;14(5):2545-68.
31. Yuste R, Tank Dw, Kleinfeld D. "Functional Study Of The Rat Cortical Microcircuitry With Voltage-Sensitive Rye Imaging Of Neocortical Slices". Cerebral Cortex. 1997;7(6):546-58.
32. Ashcroft et al. "Twenty Questions: The state of ion channel research in 2004", *Nature Reviews Drug Discovery* **3**, 239-278 (March 2004).
33. Yasuda, R., Nimchinsky, E. A., Scheuss, V.,Pologruto, T. A., Oertner, T. G., Sabatini, B.L., Et Al. (2004). "Imaging Calcium Concentration Dynamics In Small Neuronal Compartments". Sci. Stke 2004, L5.
34. Denk W, Yuste R, Svoboda K, Tank DW. "Imaging calcium dynamics in dendritic spines. Current Opinion in Neurobiology". 1996;6(3):372-8.
35. Yuste R, Denk W. "Dendritic Spines As Basic Functional Units Of Neuronal Integration". Nature. 1995;375(6533):682-4
36. Yuste R, Majewska A, Cash Ss, Denk W. Mechanisms Of Calcium Influx Into Hippocampal Spines: Heterogeneity Among Spines, Coincidence Detection By Nmda Receptors, And Optical Quantal Analysis. Journal Of Neuroscience. 1999;19(6):1976-87.
37. Smetters D, Majewska A, Yuste R. Detecting Action Potentials In Neuronal Populations With Calcium Imaging. Methods. 1999;18(2):215-21.
38. Tank Dw, Sugimori M, Connor Ja, Llinas Rr. Spatially Resolved Calcium Dynamics Of Mammalian Purkinje-Cells In Cerebellar Slice. Science. 1988;242(4879):773-7.
39. Delaney Kr, Zucker Rs, Tank Dw. Calcium In Motor-Nerve Terminals Associated With Posttetanic Potentiation. Journal Of Neuroscience. 1989;9(10):3558-67
40. Tsien Ry. A Non-Disruptive Technique For Loading Calcium Buffers And Indicators Into Cells. Nature. 1981;290(5806):527-8
41. Miyawaki A, Nagai T, Mizuno H. Engineering Fluorescent Proteins. Microscopy Techniques2005. P. 1-15
42. Mank M, Griesbeck O. Genetically Encoded Calcium Indicators. Chemical Reviews. 2008;108(5):1550-64.
43. Hasan, M.T., Friedrich, R.W., Euler, T., Larkum, M.E., Giese, G., Both, M., Duebel, J.,

Waters, J., Bujard, H., Griesbeck, O., Et Al. (2004). Functional Fluorescent Ca2+ Indicator Proteins In Transgenic Mice Under Tet Control. Plos Biol 2, E163.
44. Hires SA, Tian L, Looger LL. Reporting neural activity with genetically encoded calcium indicators. Brain Cell Biology. 2008;36(1-4):69-86.
45. Cohen LB, Salzberg BM, Davila HV, Ross WN, Landowne D, Waggoner AS, et al. Changes In Axon Fluorescence During Activity - Molecular Probes Of Membrane-Potential. Journal of Membrane Biology. 1974;19(1-2):1-36.
46. Ross WN, Salzberg BM, Cohen LB, Grinvald A, Davila HV, Waggoner AS, et al. "Changes In Absorption, Fluorescence, Dichroism, And Birefringence In Stained Giant-Axons - Optical Measurement Of Membrane-Potential". Journal of Membrane Biology. 1977;33(1-2):141-83
47. Cohen L, Hopp HP, Wu JY, Xiao C, London J, Zecevic D. "Optical Measurement Of Action-Potential Activity In Invertebrate Ganglia. Annual Review Of Physiology". 1989;51:527-41.
48. Grinvald A, Cohen Lb, Lesher S, Boyle Mb. "Simultaneous Optical Monitoring Of Activity Of Many Neurons In Invertebrate Ganglia Using A 124-Element Photo-Diode Array". Journal Of Neurophysiology. 1981;45(5):829-40.
49. Zecevic D, London Ja, Cohen Lb. "Simultaneous Monitoring Of Activity Of Many Neurons In The Buccal Ganglia Of Navanax During Feeding - A Demonstration". Journal of General Physiology. 1985;86(6):A19-A
50. Dombeck DA, Blanchard-Desce M, Webb WW. "Optical recording of action potentials with second-harmonic generation microscopy. Journal of Neuroscience. 2004;24(4):999-10
51. Denk W, Svoboda K. Photon upmanship: why multiphoton imaging is more than a gimmick. Neuron, 1997; 18:351–357.
52. Denk W, Strickler JH, Webb WW (1990) Two-photon laser scanning fluorescence microscopy. Science 248:73–76.
53. Campagnola PJ, Wei MD, Lewis A, Loew LM (1999) High-resolution nonlinear optical imaging of live cells by second harmonic generation. Biophys J 77:3341–3349.
54. Ben-Oren I, Peleg G, Lewis A, Minke B, Loew L (1996) Infrared nonlinear optical measurements of membrane potential in photoreceptor cells. Biophys J 71:1616–1620.
55. Kim SA, Byun KM, Lee J, Kim JH, Kim DGA, Baac H, et al. "Optical measurement of neural activity using surface plasmon resonance". Optics Letters. 2008;33(9):914-6.
56. Hill DK, Keynes RD. "Opacity Changes In Stimulated Nerve". Journal of Physiology-London. 1949;108(3):278-81.

57. Hill DK, "The effect of stimulation on the opacity of a crustacean nerve trunk and its relation to fibre diameter," J. Physiol. (London) 1950;111:283-303.
58. Cohen LB and Keynes RD, "Evidence for structural changes during action potential in nerves from walking legs of Maia squinado," J. Physiol. (London) 1968;194:85-86.
59. Cohen LB and Keynes RD, "Changes in light scattering associated with the action potential in crab nerves," J. Physiol. (London) 1971;212:259-75.
60. Cohen LB, Keynes RD and Landowne D, "Changes in light scattering that accompany the action potential in squid giant axons: potential-dependent components," J. Physiol. (London) 1972;224:701-25.
61. Stepnoski RA, Laporta A, Raccuiabehling F, Blonder GE, Slusher RE, Kleinfeld D. "Noninvasive Detection Of Changes In Membrane-Potential In Cultured Neurons By Light-Scattering". Proceedings of the National Academy of Sciences of the United States of America. 1991;88(21):9382-6.
62. Sandlin R, Lerman L, Barry W and Tasaki I, "Application of Laser Interferometry to Physiological Studies of Excitable Tissues," Nature 1968;217:575-&.
63. Hill BC, Schubert ED, Nokes MA and Michelson RP, "Laser interferometer measurement of changes in crayfish axon diameter concurrent with action potential," Science 1977;196:426-8.
64. Akkin T, Dave DP, Milner TE and Rylander HG, "Detection of neural activity using phase-sensitive optical low-coherence reflectometry," Optics Express 2004;12:2377-2386.
65. Fang-Yen C, Chu MC, Seung HS, Dasari RR and Feld MS, "Noncontact measurement of nerve displacement during action potential with a dual-beam low-coherence interferometer," Opt. Lett. 2004;29:2028-30.
66. Hill DK, "The Volume Change Resulting from Stimulation of a Giant Nerve Fibre," Journal of Physiology-London 1950;111:304-327.
67. Bryant SH and Tobias JM, "Optical and Mechanical Concomitants of Activity in Carcinus Nerve .1. Effect of Sodium Azide on the Optical Response .2. Shortening of the Nerve with Activity," Journal of Cellular and Comparative Physiology 1955;46:71-95.
68. Hill BC, Schubert ED, Nokes MA and Michelson RP, "Laser interferometer measurement of changes in crayfish axon diameter concurrent with action potential," Science 1977;196:426-8.
69. Iwasa K, Tasaki I and Gibbons RC, "Swelling of Nerve-Fibers Associated with Action-Potentials," Science 1980;210:338-339.

70. Tasaki I, Kusano K and Byrne PM, "Rapid mechanical and thermal changes in the garfish olfactory nerve associated with a propagated impulse," Biophys. J. 1989;55:1033-40.
71. Tasaki I and Byrne PM, "Volume expansion of nonmyelinated nerve fibers during impulse conduction,"Biophys. J. 1990;57:633-5.
72. Nassif N, Cense B, Park BH, Pierce MC, Yun SH, Bouma BE, Tearney GJ, Chen TC and de Boer JF, "In vivo high-resolution video-rate spectral-domain optical coherence tomography of the human retina and optic nerve," Optics Express 2004;12:367-376.
73. Nassif N, Cense B, Park BH, Yun SH, Chen TC, Bouma BE, Tearney GJ and de Boer JF, "In vivo human retinal imaging by ultrahigh-speed spectral domain optical coherence tomography," Optics Letters 2004;29:480-482.
74. Joo C, Akkin T, Cense B, Park BH and de Boer JF, "Spectral-domain optical coherence phase microscopy for quantitative phase-contrast imaging," Optics Letters 2005;30:2131-2133.
75. Huang D, Swanson EA, Lin CP, Schuman JS, Stinson WG, Chang W, Hee MR, Flotte T, Gregory K, Puliafito CA and Fujimoto JG, "Optical coherence tomography," Science 1991;254:1178-81.
76. Swanson E, Izatt J, Hee M, Huang D, Lin C, Schuman J, Puliafito C and Fujimoto J 1993 Opt. Lett. **18** 1864–6.
77. Schmitt J M, Kn¨uttel A, Yadlowsky M and Eckhaus M, “Optical coherence tomography of a dense tissue: statistics of attenuation and backscattering”, 1994; Phys. Med. Biol. **39** 1705–20
78. Hee M R, Izatt J A, Swanson E A, Huang D, Schuman J S, Lin C P, Puliafito C A and Fujimoto J G 1995a Arch. Ophthalmol. **113** 325–32
79. Ducros M, Marsack J, III H R, Thomsen S and Milner T 2001 J. Opt. Soc. Am. A **18** 2945–56
80. Bowd C, Zangwill L, Blumenthal E, Vasile C, Boehm A G, Gokhale P, Mohammadi K, Amini P, Sankary T and Weinreb R 2002 J. Opt. Soc. Am. A **19** 197–206
81. Boppart S A, Brezinski M E, Pitris C and Fujimoto J G 1998b. Neurosurgery **43** 834–41
82. Boppart S A 2003 Psychophysiology **40** 529–41
83. Feldchtein F I, Reitze D, Sergeev A, Gelikonov V, Gelikonov G, Kuranov R, Gladkova N, Iksanov R, Ourutina M and Warren J 1998 Opt. Express **3** 239–50
84. Otis L L, Colston B W Jr, Everett M J and Nathel H 2000 Dentomaxillofac. Radiol. **29** 85–9

85. B.H. Park, C.E. Saxer, S.M. Srinivas, J.S. Nelson, J.F. de Boer, “In vivo burn depth determination by high-speed fiber-based polarization-sensitive optical coherence tomography,” Journal of Biomedical Optics 6(4): 474-9 (2001).
86. Boppart S A, Tearney G J, Bouma B E, Southern J F, Brezinski M E and Fujimoto J 1997 Proc. Natl Acad. Sci. USA **94** 4256–61
87. Dunkers J P, Cicerone M T andWashburn N R 2003 Opt. Express **11** 3074–9
88. Boppart S A, Brezinski M E, Tearney G J, Bouma B E and Fujimoto J G 1996 J. Neurosci. Meth. **70** 65–72
89. Mason C, Markusen J F, Town M A, Dunnill P andWang R K 2004a Phys. Med. Biol. **49** 1097–116
90. Mason C, Markusen J F, Town M A, He Y, Dunnill P and Wang R K 2004b Biosensors Bioelectron. **20** 414–23
91. Wang R K 2004 Meas. Sci. Technol. **15** 725–33
92. Fukana T and Yamaguchi I 1996 Opt. Lett. **21** 1942–4
93. Chinn S R and Swanson E A 1996 Opt. Lett. **21** 899–901
94. Dunkers J P, Parnas R S, Zimba C G, Peterson R C, Flynn K M, Fujimoto J G and Bouma B E 1999 Composites A **30** 139–45
95. Dunkers J P, Phelan F R, Zimba C G, FLynn K M, Saunders D P, Peterson R C and Parnas R S 2001 Polym. Compos. **22** 803–14
96. Mujat M, Park BH, Cense B, Chen TC, de Boer JF. Autocalibration of spectral-domain optical coherence tomography spectrometers for in vivo quantitative retinal nerve fiber layer birefringence determination. Journal of Biomedical Optics. 2007;12(4).
97. Drexler W, Fujimoto JG. [Editors]. “Optical Coherence Tomography – Technology and Applications”, 2008. First Edition, Springer.
98. Wang LH, Wu H. “Biomedical Optics, Principles and Imaging”, 2007. First Edition, Johns Wiley & Sons, Inc.
99. Shuster CN, Barlow RB, Brockman HJ. “The American Horseshoe Crab”, 2003. First Edition, Harvard University Press.
100. Hartline HK, Ratliff F. (Editor). “Studies on Excitation and Inhibition in the Retina”, 1974; First Edition; The Rockefeller University Press.
101. Sekiguchi K. “Biology of Horseshoe Crabs”, 1988; First Edition, Science House Co. Ltd., Tokyo.
102. Park BH, Cense B, Pierce MC and de Boer JF, "A novel technique for speckle reduction with multifunctional optical coherence tomography," SPIE Photonics West 2006;Biomedical Optics:6085-02.
103. Boyd TE, Ets HN. Studies on cold block in nerve I. Block with and without freezing. American Journal of Physiology. 1934;107(1):76-84.

104. Boyd TE, Gerard RW. The effect of prolonged activity on the irritability of medullated nerve. American Journal of Physiology. 1930;92(3):656-64.
105. Hartline HK. Intensity and duration in the excitation of single photoreceptor units. Journal of Cellular and Comparative Physiology. 1934;5(2):229-47.
106. S. Yazdanfar, C.H. Yang, M.V. Sarunic, and J.A. Izatt, "Frequency estimation precision in Doppler optical coherence tomography using the Cramer-Rao lower bound," Opt. Express **13**, 410 (2004).
107. http://www.docstoc.com/docs/122964542/Horseshoe-crab-Limulus-%EF%BF%BD- dorsal-view
108. Md. Rezuanul Haque, Md. Shahidul Islam, Christian M. Oh, B. Hyle Park, "Development of a cold block for switchable activation/deactivation of action potential propagation", UC System wide Bioengineering Symposium, UCSB (2011)
109. http://pinterest.com/susanbon/the-oddly-strange-have-to-know-more-list/
110. http://www.cam.ac.uk/sites/www.cam.ac.uk/files/styles/content-580x288/public/news/research/news/111102-queensland-fruit-fly-bactrocera-tryoni-bareego.jpg?itok=tB1prXoj
111. J. R. Weber et al., in Conference on Biomedical Optics, OSA Technical Digest, 2010, paper BSuD110p.

112. K. F. Rajneesh et al., J. Neurosurg. 113(2), A422–A423 (2010).

113. Young-Joon Kim, Dusˇan Zˇ itnˇ an, et al. A Command Chemical Triggers an Innate Behavior by Sequential Activation of Multiple Peptidergic Ensembles, Current Biology 16, 1395–1407